Ab initio study of thermoelectric phenomena via the exact solution of the Boltzmann equation

Fiorentini, Mattia

Awarding institution:
King's College London

Ab initio study of thermoelectric phenomena via the exact solution of the Boltzmann equation

Mattia Fiorentini

Department of Physics
King's College London

This dissertation is submitted for the degree of
Doctor of Philosophy

April 2017

Abstract

A detailed understanding of electrical transport and energy dissipation phenomena is crucial for the discovery and engineering of new, high-performance materials for application ranging from nano-electronics to thermoelectric energy conversion. The experimental investigation of charge and heat conduction in controlled conditions is often challenging and expensive, and therefore accurate and efficient theoretical and simulation approaches are pivotal to foster new advancements.

In my PhD work I have developed an ab initio computational approach to predict electronic transport properties of bulk materials. This work goes beyond the state-of-the-art in the field by merging an accurate, first-principles description of the fundamental interaction between electrons and lattice vibrations, and the exact solution of the Boltzmann transport equation . This computationally challenging task is accomplished by the development of a novel, fully parallel computational infrastructure based on state-of-the-art high-performance computing techniques.

This approach allows the calculation of a range of electronic transport coefficients (electrical conductivity, mobility, electronic thermal conductivity, Seebeck coefficient and Lorenz number), also accounting for the effects of non-equilibrium phonon populations due to thermal gradients. In addition, the analysis tools developed in this work provide accurate ways to examine the microscopic details of the relevant scattering mechanisms and decay channels that determine each specific transport coefficient. These developments are of fundamental importance to assess and validate a number of approximations and phenomenological models that are popular within the electronic transport and thermoelectric communities. In addition, this work provides accurate tools to test design rules to enhance the thermoelectric performance and guide the experimental synthesis and characterization of more efficient compounds.

In this work, I have applied this computational framework to the investigation of many aspects of thermoelectricity in diverse classes of materials, such as metals and doped semiconductors, in a wide range of temperature and, where suitable, doping concentration.

In elemental metals, predictions for resistivity and Lorenz number have been compared against experiments and previous first-principles results, confirming the effectiveness of approximate approaches to Boltzmann transport for these systems. In n-doped silicon, I have focused on a wide range of electric and thermoelectric quantities. In addition to a detailed characterization of resistivity and mobility, this work provides a unique insight on the Lorenz number, a quantity that is not directly accessible with experiments and plays an important role in thermoelectric engineering. Moreover, the analysis of the Seebeck coefficient provides a better understanding of the coupled electron and phonon dynamics in this material, also suggesting strategies towards higher thermoelectric efficiency. Finally, I have analysed the transport properties of boron-doped diamond. Here I have used phenomenological models to simulate the complex doping mechanism in place in this system. I have focused on the prediction of the best transport properties achievable in Boron-doped diamond, in order to provide a useful reference for the experiments that typically display a large uncertainty (due to the difficult assessment of impurity content in synthetic samples). The characterization of the different phonon scattering channels (also in comparison with the case of silicon) offers an insight into the origin of the extraordinary hole mobilities of this system.

Table of contents

List of figures **ix**

List of tables **xi**

Nomenclature **xiii**

1 Introduction **1**
1.1 Motivation 1
1.2 Summary 5

2 *Ab initio* techniques for electronic transport **7**
2.1 Microscopic origin of electronic transport 7
2.2 Electronic ground-state properties from Density Functional Theory 8
2.2.1 The Exchange-Correlation energy in the Local Density Approximation 11
2.2.2 Physical quantities in DFT 12
2.3 Density Functional Perturbation Theory for lattice vibrations 13
2.4 Electron-phonon coupling from first principles 16
2.5 Wannier interpolation for electronic and vibrational properties, and electron-phonon coupling 18

3 Semi-classical transport theory **23**
3.1 Current density 23
3.2 The Onsager relations and linear response 26
3.3 Boltzmann equation 28
3.3.1 Derivation 28
3.3.2 Linearisation 31
3.3.3 Linearised BE 35
3.4 Electron scattering mechanisms 36

3.4.1 Phonon scattering . . . 37
3.4.2 Ionized impurities . . . 38
3.4.3 Neutral impurities . . . 39
3.5 Phonon drag . . . 40
3.5.1 Decoupling phonons from electrons . . . 40
3.5.2 The *phonon drag* driving force . . . 41
3.6 Comparison with approximated methods . . . 42
3.6.1 Relaxation time approximation . . . 42
3.6.2 Variational formula for transport coefficients . . . 46

4 HPC methods for the exact LBE solution 49
4.1 `eBET`: exact Boltzmann Electronic Transport . . . 49
4.2 Multi-mesh interpolation for electronic transport . . . 50
4.3 The MPI cartesian topology . . . 52
4.4 Preconditioned Conjugate Gradients solver . . . 55
4.4.1 Preconditioning . . . 56
4.4.2 Comparison with Steepest Descent . . . 57
4.4.3 Implementation and convergence . . . 59

5 Elemental metals: framework validation 61
5.1 Electric resistivity . . . 62
5.2 Thermal transport by electrons . . . 64
5.3 Wiedmann-Franz law from first-principles . . . 64
5.4 Conclusion . . . 66

6 Silicon: first-principles thermoelectricity with non-equilibrium phonon effects 69
6.1 System simulation from first principles . . . 70
6.2 Transport coefficient . . . 71
6.2.1 Mobility and resistivity . . . 71
6.2.2 Seebeck coefficient . . . 74
6.2.3 Lorenz number . . . 78
6.2.4 Sensitivity of the kinetic coefficient on the scattering mechanisms . 82
6.2.5 Kelvin relation for the electronic system with phonon drag . . . 84
6.3 Approximate approaches to BE . . . 85

7 Diamond: electronic transport for next-generation electronics 87
7.1 Boron ionization in Diamond 88
7.2 Mobility and resistivity at room temperature 90
7.3 Temperature dependence of Mobility 93

8 Conclusion 99
8.1 Future outlook 101

Appendix A Deriving the BE from the BBGKY hierarchy 105

Appendix B Deformation potential models in Silicon 109

Appendix C Numerical parameters and convergence 113
C.1 Metals 113
C.1.1 Aluminium 113
C.1.2 Copper 113
C.2 Silicon 114
C.2.1 Convergence of transport quantities 114
C.2.2 Performance and accuracy of the BE solver 116
C.3 Diamond 117

References 119

List of figures

1.1 Basic operational modes of a thermoelectric device 2
1.2 ZT doping dependence at $T = 300$K in $Si_{80}Ge_{20}$ 4

4.1 Flowchart of the eBET software developed for the calculation presented in this work 51
4.2 Diagramatic representation of a distributed matrix - vector product 53
4.3 Graphical comparison of convergence between CG and SD 59

5.1 Al (left panel) and Cu (right panel) electrical resistivity as obtained in this work 62
5.2 Cu electrical resistivity in earlier literature 63
5.3 Al thermal resistivity (left panel) and Cu thermal conductivity (right panel) of electrons as obtained in this work 64
5.4 Al and Cu electrons' thermal transport coefficient from the literature 65
5.5 Al (left panel) and Cu (right panel) L as obtained in this work 66

6.1 Si electron mobility at room temperature 71
6.2 Si electron mobility as temperature function 72
6.3 Si electrical resistivity and thermal conductivity of the electrons 73
6.4 Contribution to electrical resistivity per scattering channel at room temperature 75
6.5 Total Seebeck coefficient in function of doping concentration at room temperature 76
6.6 Accumulation plot of phonon drag contribution to the Seebeck coefficient in silicon 77
6.7 Accumulation plot of the lattice thermal conductivity as a function of the phonon frequency in silicon 78
6.8 Total Seebeck coefficient as function of temperature in Si 79
6.9 Lorenz number as function of donor concentration 79

6.10 Lorenz number as function of the Seebeck coefficient 81
6.11 Accumulation plot of L and S in the energy spectrum 83
6.12 Intrinsic mobility in the RTA approximation and using the varrational formula 85

7.1 Total acceptor concentration versus ionised acceptor concentration at room temperature 89
7.2 Diamond electric resistivity at room temperature as function of Boron concentration 91
7.3 Hole drift mobility at room temperature as function of Boron concentration 92
7.4 Hole drift mobility as function of temperature 94
7.5 Contribution to Diamond resistivity by each scattering channel in a temperature range 95
7.6 Comparison between $\mu_h(T)$ obtained from the exact BE solution and RTA in Diamond 96

8.1 Diamond diffusive S as function of temperature 101

B.1 Si drift mobility using deformation potential fitted with first-principles parameters 111

C.1 Convergence of electron mobility 115
C.2 CG convergence through iterations 116
C.3 Spatial decay of relevant operators in the MLWF basis 117

List of tables

B.1 Intra valley phonon modes parameters from first-principles. 110
B.2 Inter-valley phonon modes parameters from first principles. 110

Nomenclature

Roman Symbols

Al	Aluminium
Cu	Copper
e	Electric charge quantum
k_B	Boltzmann's constant
L	Lorenz number
m	Mass
n	Spatial density
S	Seebeck coefficient
T	Temperature
V	External potential
ZT	Dimensionless thermoelectric figure of merit

Greek Symbols

β	Reciprocal of the thermal energy, $\beta \equiv {}^{1}/_{k_B T}$
σ_e	Electric conductivity
λ	Phonon branch
μ_e	Electron mobility
μ_h	Hole mobility

ε Energy

ω Angular frequency

ψ Kohn-Sham orbital

ρ_e Electric resistivity

Superscripts

0 Ground state property

Subscripts

e Electron

h holes

m Band index

ph Phonon

Other Symbols

$\mathscr{C}$ Collision matrix

$\mathscr{D}$ Dynamical matrix of the inter-atomic force constants.

$\mathscr{H}$ Hamiltonian operator

$\hbar$ Planck's constant reduced

$\mathbb{N}$ Natural numbers

$\mathbb{R}$ Real numbers

Acronyms / Abbreviations

BE Boltzmann transport equation

BT Boltzmann transport theory

BW Bloch wave function

BZ First Brillouin zone

CG Conjugate Gradient algorithm

CM Collision matrix

CRTA Constant RTA

DFT Density functional theory

$e-e$ Electron - electron interaction

EPC Electron-phonon coupling

EPCM Electron-phonon coupling matrix

$e-ph$ Electron - phonon

ERTA Energy RTA

GS Ground state

HEG Homogeneous electron gas

LBE Linear Boltzmann equation

LDA Local density approximation

LOVA Lowest Order Variational Approach to BE

MLWF Maximally localized Wannier function

MRTA Momentum RTA

PC Primitve Cell

RTA Relaxation-time approximation

SCF Self-consistent field

SD Steepest descent algorithm

TE Thermoelectric

ToF Time-of-flight

WF Wannier function

Chapter 1

Introduction

1.1 Motivation

Addressing the issues of energy production, dissipation and recovery is of paramount importance to sustain development and prosperity of modern society[1, 2]. For instance, in today's electronic industry energy conservation has become the most prominent aspect in the design of next-generation devices[3] and has lead to renewed efforts to bring novel power-efficient materials into mainstream applications[4, 5]. On the other hand, an intense worldwide scientific effort is currently focused onto the search for green technologies to convert, for example, waste heat produced by industrial factories, car engines and everyday electronics into usable energy; in these regards, a particularly active and exciting field of research is thermoelectric (TE) energy conversion[6]. Here, the fabrication of efficient power generators (and refrigerators) relies on experimental and theoretical innovations and the discovery of new classes of materials to boost long-known phenomena such as the TE effects.

Thermoelectricity has indeed a quite long history. The first thermoelectric phenomenon was observed in 1821 by Thomas Johann Seebeck and is thus called the Seebeck effect: a voltage difference was measured in a metal junction as a result of a temperature difference between the junction's extremities. Closing the circuit, a current density arises that is proportional to the temperature gradient: the proportionality factor is called Seebeck coefficient. The other complementary TE phenomenon is the Peltier effect; in 1834, in a system similar to the one used by Seebeck, Jean Charles Athanase Peltier observed the occurrence of a temperature gradient as a result of an electric current. What is peculiar of the Peltier heat is that, in contrast with the Joule effect, the direction of the heat flux between the junction's extremities depends on the direction of the electric current.

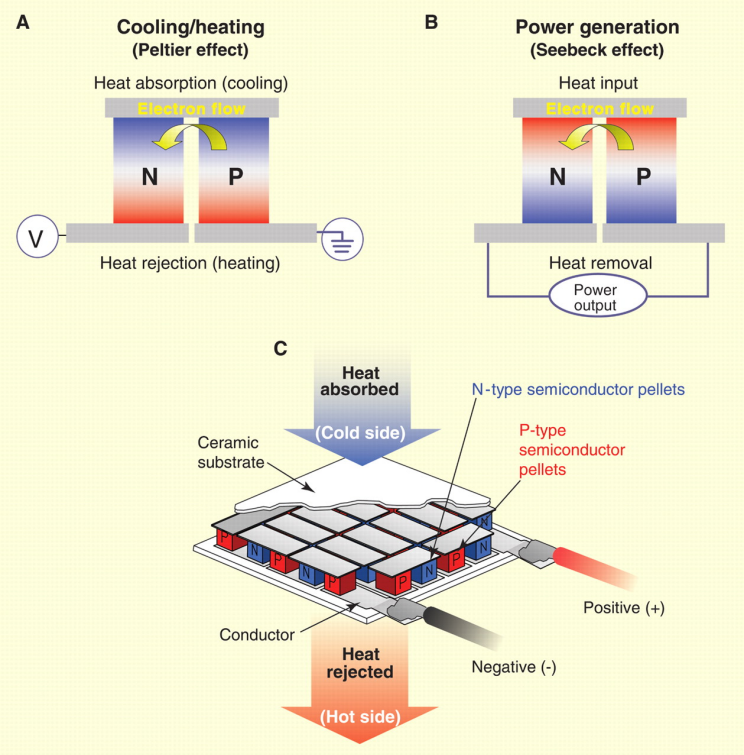

Fig. 1.1 Essential structure of a TE device: the core element is composed of a couple of n- and p- type TE materials, and is capable of providing all the fundamental operational modes e.g. heating, cooling and electric generation. Figure from Ref. 7.

These effects are at the basis of TE devices (see Fig 1.1) that allow (a) heat extraction and (b) energy harvesting. Such devices have been employed in a number of applications from the early 1950s[7–10]: electric generation in extreme environments[1], waste heat recovery in the automotive industry[11], solid-state cooling in electronics, temperature control for complex high-tech systems, *et cetera*. The interest in these devices stems from their compactness, reliability and environmental friendliness[2, 12]: TEs are solid state systems that do not require moving parts, combustion or gas/liquid phases to operate as opposed to e.g. refrigerators, heat pumps or turbines.

The performance of TE materials is measured in terms of the dimensionless figure of merit, ZT. The main impairment to a large-scale use in both commonplace and high-tech applications is the poor efficiency compared to traditional devices e.g. mechanical thermal engines or heat pumps. As an example, commercially available TE refrigerators have $ZT \approx 1$ and their efficiency is around 10%, compared to the 60% figure of two-phase- fluids air

[1] Beginning with the NASA Apollo missions every deep space operation has been powered with the aid of TE devices[10].

conditioners[7], corresponding to a $ZT \approx 4$ [13]. The consensus is that at least a $ZT \gtrapprox 2$ in necessary for a wider commercial exploitation, while for specific large-scale, high-power applications significantly higher ZT are sought[14]. However, finding good TE materials with high ZT is a challenging task. Alloying elements is a traditional search path for new materials: among the most successful systems for common applications are SiGe[15] (1956) and, PbTe and Bi_2Te_3[16] (1910), with $ZT \approx 1$ at the operational temperature[17].

ZT is solely defined in term of the electronic and thermal transport details of the material[18],

$$ZT = \frac{\sigma_e S^2 T}{k_e + k_l}. \tag{1.1}$$

As shown in the numerator of Eq. 1.1 a large Seebeck coefficient, S, and electrical conductivity, σ_e – being $\sigma_e S^2$ the *power factor*–, lead to an enhancement of ZT. On the contrary, the figure of merit is suppressed by large electronic and lattice thermal conductivities, k_e and k_l, that add up in the denominator of Eq. 1.1. In the 1990s, the rise of nanotechnology introduced new paradigms in TE material engineering. The idea of nanostructured bulk systems[19] and low-dimensional conductors[20] led to the concept of *phonon glass/electron crystal* systems [21]: better ZT could be achieved through the design of nanostructured materials[6] that allow electrons to move freely while heavily disrupting lattice heat diffusion[14]. Traditionally, $\sigma_e S^2$ had been increased by finding optimal doping concentrations[10]. More recently, new ideas about the optimal features of the band-structure of good TEs have been suggested, e.g. having larger gaps and effective masses to enhance electronic transport[13, 22], that combined with nanostructuring to reduce heat transport, have lead to a very encouraging increase in the values of ZT, with latest generation of bulk materials having ZT above 1.5 around $700-800$K[23].

Further advances in thermoelectric energy conversion require a breakthrough in our ability to fully control transport and energy dissipation in complex materials. This entails a detailed understanding of (i) the vibrational properties of the crystal and their link to heat diffusion, (ii) the electronic band structure and its effects on electronic transport, and (iii) the scattering mechanisms that affect charge and heat conduction. For this, *ab initio* material modeling provides an accurate way to describe such fundamental aspects[24]. Once these ingredients are known, the Boltzmann transport formalism offers a convenient and effective path to calculate transport coefficients. In the past few years this approach has been extremely successful to study lattice thermal conductivity of materials [25, 26].

On a more general footing, the *ab initio* study of electronic transport poses further intricacies compared to heat diffusion[24] both from modeling and computational perspectives.

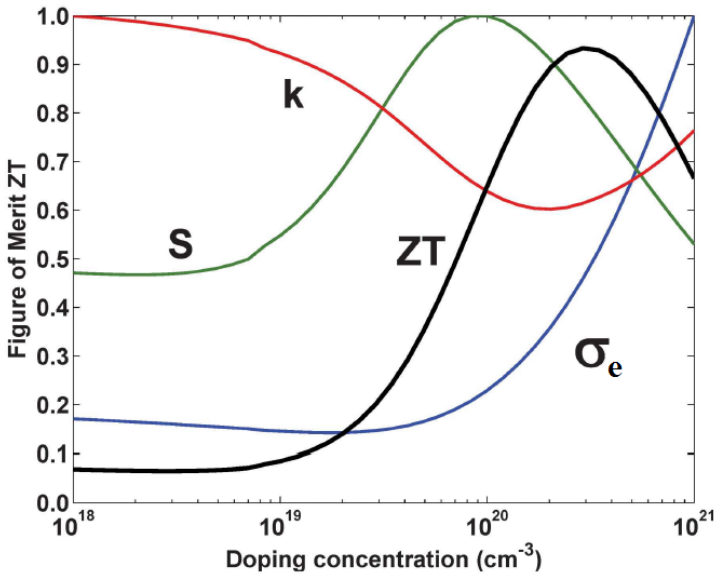

Fig. 1.2 ZT doping dependence at $T = 300$ K in $Si_{80}Ge_{20}$. σ_e is the electrical conductivity, S the Seebeck coefficient and k the total thermal conductivity. Figure from Ref. 6

In particular, it is important to stress that the accurate description of electronic transport in doped semiconductors requires addressing notable challenges. For instance, in order to capture the complex temperature and doping dependence of transport coefficients (see Fig. 1.2), it is necessary to have an accurate description of the carrier density, and of the nature and the concentration of impurities, that effectively scatter charge carriers. In addition, the interplay between heat and electrical currents is often important and give rise to *phonon drag* effects [2] that can significantly affect transport coefficients.

The state-of-the-art in first-principles electronic transport within the Boltzmann transport Theory (BT) can be described by discussing the case of silicon. Even for this relatively simple system of huge technological importance, a fully *ab initio* calculation including the exact solution of the Boltzmann equation for a range of doping concentrations is still missing. Indeed, Zhou et al. [27] have recently achieved a quite complete *ab initio* study of doped silicon, but resorting to an approximate solution of the BE. On the other hand, Li [28] recently solved the Boltzmann transport equation (BE) for silicon but without accounting for carrier-impurity interactions, and thus focusing only on the intrinsic regime.

The development of efficient BE solvers interfaced with *ab initio* electronic structure codes is crucial to boost the predictive power in the field of electronic transport. This is an important step that will also allow the assessment of simpler approaches that can be used for

[2] Phonon drag acts as an additional driving force, similarly to electric fields and temperature gradients: this effect will be discussed in n-doped Silicon in Chap. 6.

systems that present an higher degree of complexity and for which the full solution of the BE is computationally prohibitive.

1.2 Summary

In this work, a novel computational approach is implemented for the investigation of electronic transport properties from first principles; the computational framework has been successfully applied on Copper, Aluminium, n-doped Silicon and Boron-doped Diamond. This work goes beyond the state-of-the-art in electronic transport calculations by merging an accurate simulation of the fundamental interaction between electrons and lattice vibrations, with the exact solution of the Boltzmann transport equation in linear response. Notably, the formalism developed also allows the study of out-of-equilibrium phonons effects on transport coefficients. Electron and phonons ground state properties are obtained using Density Functional Theory (DFT) and Density Functional Perturbation Theory (DFPT). The scattering of charge carriers from phonons and impurities is carefully considered; in particular, the electron-phonon coupling is accurately calculated from first principles. The efficiency and accuracy of Wannier interpolation is exploited for the ultra-dense sampling of the reciprocal space required in the solution of the BE. The combination of an accurate first-principles description of the system with the exact solution of the transport theory is a computationally intensive task; for this reason, a software infrastructure has been developed from scratch by using sophisticated high performance computing techniques.

The list of achievements that has just been mentioned, highlights few innovative points compared to popular codes that are widely used within the electronic transport community. As a first example, it is possible to cite BoltzTraP [29], released in 2006. This software package exploits the semi-classical Boltzmann theory to calculate the kinetic transport coefficients of Eq. 3.32, where the key quantity is the function $\tau_m \boldsymbol{k}$, often regarded as *relaxation time*. This well-known software implementation disregards the microscopic description of charge carrier scattering events altogether, resorting to the *constant relaxation time approximation* (see Sec. 3.6.1), in which case the Boltzmann equation is not solved, and a constant, effective relaxation time, τ, has to be provided as inputs by other means. More recently, another software package for the calculation of electronic transport coefficients has been released, BoltzWann [30]. Interestingly, this code exploits maximally localized Wannier functions (see Sec. 2.5) to obtain band structure on dense $\boldsymbol{k}$-point grid, but similarly to BoltzTraP, is not capable of solving the Boltzmann equation, thus failing to link the band and $\boldsymbol{k}$ dependence of the relaxation time, τ to the microscopic scattering events.

The first application of this computational infrastructure regards simple metals: these systems represent an excellent test-case for this novel framework. For both Aluminium and Copper, a wide literature of experimental and theoretical studies is available. In particular, this work is compared to precedent studies where the effect of the electron-phonon coupling was considered within DFT: in this case, it is possible to compare our exact BE solution with a common variational approach to BT.

The second application is a complete study of the electronic transport and TE coefficients of n-doped Silicon, also accounting for non-equilibrium phonon effects. Two are the main outcomes of this study. The first is a detailed understanding of the role of the different scattering mechanisms on the various transport coefficients. This analysis is particularly useful in the case of the Seebeck coefficient as it highlights the possibility to exploit the phonon drag effect to increase ZT. The second outcome is the assessment of simplified scattering models (e.g. deformation potential models) and approximate transport approaches that are popular within the transport community, such as different kinds of Relaxation Time Approximation (RTA) and an empirical model to estimate the Lorenz number.

Finally, Boron-doped Diamond is studied for next-generation electronic devices. Compared to the case of Silicon, here the effect of impurities both on the charge carrier density and on carriers' scattering is less understood and requires the use of phenomenological models that have been carefully tested. The study of this system in a range of boron concentrations provides a theoretical reference for the highest hole mobilities that can be achieved in ideal conditions (non compensation). In addition, the study of the mobility as a function of temperature offers an insight on the role of acoustic and optical phonon modes on electrical transport in diamond, explaining the change in the temperature dependence of hole mobility.

The structure of this thesis is as follows. Chap. 2 describes the first-principles techniques used to computed the fundamental physical quantities necessary for transport, namely the electronic bands, $\varepsilon_m(\boldsymbol{k})$, phonon energies, $\hbar\omega_\lambda(\boldsymbol{q})$, and the electron-phonon coupling (EPC) function. Chap. 3 reviews the theoretical principles used to calculate the transport coefficients. After introducing electrical and heat current densities in Sec. 3.1, the definition of transport coefficients in the Onsager formalism is provided in Sec. 3.2. Then, the Boltzmann transport theory is discussed in depth in Sec. 3.3 and the relevant electronic scattering mechanisms are reviewed in Sec. 3.4, with a particular emphasis on the phonon drag effect (Sec. 3.5). In Chap. 4, the computational aspects of solving the linearized BE are discussed, with details about the HPC techniques used to actually make these calculations possible. In Chaps. 5, 6, 7 the results on simple metals, Silicon and Diamond are presented and discussed. The conclusions and future outlook for this approach are given in Chap. 8.

Chapter 2

Ab initio techniques for electronic transport

2.1 Microscopic origin of electronic transport

To describe transport phenomena, this work adopts the semi-classical Boltzmann theory, that has the Boltzmann transport Equation (BE) as a cornerstone. The BE was developed by L. E. Boltzmann in 1872 to calculate transport properties of a dilute gas of weakly interacting, classical particles. Hence, it is not obvious that the use of this equation is legitimate to calculate electronic transport properties of metals and semiconductors; electronic densities in condensed matter are very high, Coulomb interaction is long-range, and the appropriate microscopic description should be the quantum-mechanical one.

However, the theoretical developments by Landau in the late 1950s [31] revealed that the carriers in condensed matter, especially in metals and doped semiconductors, are not the strongly-interacting and dense electrons but excitations which behave like a dilute gas of weakly interacting quasi-particles, the *Fermi liquid*; for these systems the BE can be justified[32–34] and, as a matter of fact, is commonly employed [35]. The resulting transport picture is the following: weak external fields do not alter the ground state electronic structure of the system but induce a semi-classical dynamics that perturbs the Fermi-Dirac equilibrium statistics of the carriers[36].

The physical scenarios in which the Boltzmann transport theory is a suitable framework for describing electronic transport are the ones in which charge carriers can be described as wave-packets. This means that the spatial and temporal variation of the perturbing external fields has to be small compared to the wavelength and energy of the packets, the effective two-body interaction experienced by charge carrier has to be short-ranged, compared to

the average carrier-carrier separation. BT fails whenever the wave nature of the electrons manifests itself and has to be included in the description of the scattering. For instance, when the dimensions of the system are smaller than the phase relaxation length of carriers (the average distance that an electron travels before information about its initial phase is lost), the quantum-mechanical wave-function of the carriers has a well-defined phase throughout the system. In this so-called coherent transport regime quantum interference effects such as Aharonov-Bohm oscillations may observed in transport. Another example in which BT fails is the extreme case in which the size of the system is smaller than the electron mean free path: in this ballistic regime carriers can cross the device without scattering, and a quantised conductance is observed in measurements.

In this chapter, it is discussed how these excitations and their interactions that are relevant to transport are modelled. In principle, these many-electron system properties should be computed using a proper quasi-particle band scheme, GW being currently the most popular approximation. Given the difficulties of this approach, the DFT framework is adopted. Indeed, practical experience[37] shows that at least for s- and p- bonded compounds, DFT (already at the level of the Local Density Approximation (LDA)) often gives a remarkably reliable model for quasi-particle properties. In addition to DFT, DFPT is very effective in modeling the vibrational properties of the system and, most importantly, the interaction between the lattice and charge carriers, which is a quantity of main interest in first-principles electronic transport.

2.2 Electronic ground-state properties from Density Functional Theory

The Ground State (GS) electronic properties are the first main ingredient needed to explicitly compose the BE. Since this work is focused on the prediction of transport from first-principles, it is important to devise a computational framework that is accurate while keeping the workload manageable.

Density Functional Theory paves a path to the calculation of the total GS energy of a many-electron system by reducing the problem of computing the electronic wave-functions, $\Psi(\boldsymbol{r}_1,\ldots,\boldsymbol{r}_N)$, of N interacting electrons, that depend on $3N$ variables, to calculating the electronic density, $n(\boldsymbol{r})$, which depends on 3 variables. Hohenberg and Kohn [38] showed that the GS energy of an interacting electron gas in an external potential, V, is a functional of

n,

$$E[n] = F[n] + \int n(\boldsymbol{r})V(\boldsymbol{r})\mathrm{d}_3 r, \tag{2.1}$$

through an *universal functional*, $F[n(\boldsymbol{r})]$ [1]. This theorem has the major implication that the GS electronic density, n^0, is the one that minimises $E[n]$ and it is unique for every choice of V [2]. Following this observation, all the GS properties of the system are in fact functionals of n^0, including the wave-functions $\Psi^0[n^0]$. Implementing the Hohenberg and Kohn [38] theorem is non-trivial for several reasons [39]: some of the intricacies regard the facts that an explicit form of the universal functional $F[n(\boldsymbol{r})]$ is not known, the formal representation of all the other observables as functionals of the ground state density is not straightforward, and also the choice of physically meaningful densities is a matter of debate.

Kohn and Sham [40] reformulated the problem of minimizing Eq. 2.1: they proposed a set self-consistent equations to practically implement DFT. The pivotal intuition was that the energy functional of the interacting system can be mapped to a system of non-interacting particles. The starting point is to observe that for the non interacting electron gas, $F[n]$ is equal to the kinetic energy, $T[n]$: in this case, the total kinetic energy is just the sum of the kinetic energy of the single-particle orbitals, ϕ,

$$T_s[n] = -\frac{\hbar^2}{2m_e}\sum_i^N \int \phi_i^*(\boldsymbol{r})\nabla^2\phi_i(\boldsymbol{r})\mathrm{d}_3 r, \tag{2.2}$$

where the functional dependence on n is implicitly inherited from ϕ.The total energy of the interacting system can then be linked to T_s by the formal definition of the *exchange-correlation energy* term, $E_{xc}[n]$ that makes up for the neglected quantum-mechanical features both in T_s and in the Hartree energy term,

$$F[n] = T[n] + U[n] \equiv T_s[n] + \frac{e^2}{2}\int \frac{n(\boldsymbol{r})n(\boldsymbol{r}')}{|\boldsymbol{r}-\boldsymbol{r}'|}\mathrm{d}_3 r\mathrm{d}_3 r' + E_{xc}[n], \tag{2.3}$$

where Hartree energy terms has been explicitly written down as the classical electrostatic potential energy.

The path to map an interacting electron system to a non-interacting one can be sketched from the observation that the electronic density of a non-interacting system can mimic the behavior of a physical system with two-body Coulomb interactions upon the application of a

[1] *Universal* means that F depends only on $e-e$ interaction and not on V.

[2] This statement has to be handled with care in the case of degenerate GS.

suitable one-body potential [3],

$$V_{SCF}(\boldsymbol{r}) = V(\boldsymbol{r}) + e^2 \int \frac{n(\boldsymbol{r}')}{|\boldsymbol{r}-\boldsymbol{r}'|} \mathrm{d}_3 r' + v_{xc}(\boldsymbol{r}). \tag{2.4}$$

The field defined on the left-hand side of Eq. 2.4 is referred to as *self-consistent field* (SCF) potential and involves the definition of the exchange-correlation potential, that is the functional derivative of the exchange correlation energy,

$$v_{xc}(\boldsymbol{r}) = \frac{\delta E_{xc}}{\delta n(\boldsymbol{r})}. \tag{2.5}$$

At this point, the issue of knowing the kinetic energy functional, $T[n]$ has become irrelevant. In fact, the total energy of the many-electron system can calculated from the one-body self-consistent field potential, $V_{SCF}(\boldsymbol{r})$: because of the Hohenberg and Kohn [38] theorem, n^0 of the interacting system is the same GS electronic density, n_s^0 of the one-body auxiliary system that is defined by $V_{SCF}(\boldsymbol{r})$. The calculation of n_s^0 is carried out after solving the much simpler one-body Schrödinger equation,

$$\left\{ -\frac{\hbar^2}{2m_e}\nabla^2 + V_{SCF}[n](\boldsymbol{r}) \right\} \psi_m(\boldsymbol{r}) = \varepsilon_m \psi_m(\boldsymbol{r}) \tag{2.6}$$

to obtain the auxiliary one-body wave-functions $\psi_n(\boldsymbol{r})$, named the *Kohn-Sham orbitals*. Is worth noting that, as the notation suggests, $V_{SCF}[n](\boldsymbol{r})$ depends implicitly on ψ through n. In fact, for a non magnetic system with N electrons, n has the familiar form in terms of $\psi_n(\boldsymbol{r})$,

$$n(\boldsymbol{r}) = 2 \sum_{m=1}^{N/2} |\psi_m(\boldsymbol{r})|^2 . \tag{2.7}$$

The many-electron problem has now been reduced to finding a suitable approximation of E_{xc}. The exchange-correlation term owes its name because embodies the aspects of the many-body, fermionic, quantum system that have been explicitly neglected while adding up the other terms in Eq. 2.3: $E_{xc}[n]$ is made of the *exchange term*, E_x and the *correlation term*, E_c. These two terms conceptually stem from the Hartree-Fock theory where Ψ is approximated with a Slater determinant of one-body orbitals ϕ. E_x takes into account the

[3] Varying the total energy $E[n]$ (Eq. 2.1, 2.3) in the auxiliary KS orbitals, the Rayleigh-Ritz principle is recovered, which is the same of the Schrödinger equation for the interacting system, except for the dependence of U on n [37]. This observation means that the GS energy that can be calculated from Eq. 2.6 is the same of the interacting system, if the universal functional $E_{xc}[n]$ was known.

decrease of total energy due to the Pauli exclusion principle. E_c represents the additional energy correction due to the approximation made when writing a multi-variate probability distribution Ψ as a product of the uni-variate $\{\phi\}$ as if the electrons were independently distributed. Despite the impossibility of finding an exact analytical expression for E_c in terms of either n or Ψ, Eq. 2.3 provides an explicit form of the terms of $E[n]$ that, at least in weakly correlated systems, are responsible for the largest energy contributions [39].

2.2.1 The Exchange-Correlation energy in the Local Density Approximation

The advantage of the Kohn and Sham [40] formulation is that an analytically approximated form for $E_{xc}[n]$, appearing in Eq. 2.3, can be explicitly built from the simple model of the homogeneous electron gas (HEG): the set of approximations leading to this landmark result is known as the *Local Density Approximation* (LDA) and is tied to the pioneering works of Thomas [41] and Fermi [42].

As mentioned earlier, $E_{xc}[n]$ is made of the sum of two functionals, $E_{xc}[n] = E_x[n] + E_c[n]$, where the correlation term receives contributions from,

$$E_c[n] = (T[n] - T_s[n]) + (U[n] - U_H[n]) - E_x[n]. \tag{2.8}$$

In LDA, the guiding assumption is that the spatial variations of $n(\boldsymbol{r})$ are small so that the system can be treated locally[4] as an homogenous electron gas.

Kohn and Sham [40] proposed the functional form of $E_{xc}^{LDA}[n]$,

$$E_{xc}^{LDA}[n] = \int n(\boldsymbol{r})\varepsilon_{xc}(n)\mathrm{d}_3 r, \tag{2.9}$$

$$v_{xc}^{LDA}(n) = \left(\varepsilon_{xc}(n) + n\frac{\mathrm{d}\varepsilon_{xc}(n)}{\mathrm{d}n}\right), \tag{2.10}$$

where $\varepsilon_{xc}(n)$ is the exchange-correlation energy density and is a function (not functional) of $n(\boldsymbol{r})$. $E_{xc}^{LDA}[n]$ can be still decomposed in the sum of an exchange term and correlation term. For the HEG E_x can be easily written in term of the exchange energy density,

$$\varepsilon_x^{LDA}(n) = \varepsilon_x^{hom}(n) = -\frac{3e^2}{4}\left(\frac{3}{\pi}\right)^{1/3} n^{4/3}, \tag{2.11}$$

[4]The notion of locality applies in regard to the spatial densities of the different energy functionals.

so that,

$$E_x^{LDA}[n] = -\frac{3e^2}{4}\left(\frac{3}{\pi}\right)^{1/3}\int n(\boldsymbol{r})^{4/3}\mathrm{d}_3 r. \tag{2.12}$$

The next step is to obtain E_c. Continuing along the analogy with the HEG, the contribution due to the kinetic energy functional becomes the one of Thomas [41] and Fermi [42]. In fact, calculating T_s in terms of the Kohn-Sham orbitals ψ as in Eq.2.2 leads to more accurate results [39] [5]. The calculation of the remaining part of E_c is a quite sophisticated matter and can be carried out in several approaches [39, 43], e.g. quantum monte carlo, on which also depends the accuracy of the LDA description. An established version of the LDA is the one of Perdew and Zunger [44] and is the one adopted in this work.

2.2.2 Physical quantities in DFT

The effectiveness of LDA can be questioned considering that the eigenvalues of the auxiliary one-body Schrödinger equation Eq. 2.6 do not refer to the observable many-electron system and V_{SCF} is a fictitious, static mean-field potential. However, LDA has proven particularly successful for band structure calculations in a number of solid state systems despite significant discrepancies from the HEG: this is due to the *systematic* error cancellation between ε_x and ε_c [39, 43], particularly the fact that the *exchange-correlation hole* obeys the correct sum rule [37].

Nevertheless, V_{SCF} can be seen as an approximation of the irreducible self-energy Σ of the Dyson equation. The Dyson equation [45] provides an exact path for the calculation of the one-electron propagators in a polarized medium[6]. This equation can be recast in an form that makes a comparison between the physical many-electron system and the auxiliary one evident[47],

$$\left[-\frac{\hbar^2\nabla^2}{2m_e}+V(\boldsymbol{r})\right]\varphi_m(\boldsymbol{r})+\int\Sigma(\boldsymbol{r},\boldsymbol{r}';E_n)\varphi_m(\boldsymbol{r}')\mathrm{d}_3 r' = E_n\varphi_m(\boldsymbol{k}). \tag{2.13}$$

where V denotes an external one-body potential. The eigenvalue E_n appearing in Eq. 2.13 is the true quasi-particle energy and $\varphi_m(\boldsymbol{k})$ is the wave-function of the electronic quasi-particle. Σ is often regarded as the *mass operator* and takes into account the energy contribution arising from the polarization of the electronic medium because of the presence of an additional electron. In contrast with V_{SCF}, Σ is a non-local, energy dependent, complex potential.

[5] One of the most well-known shortcomings of the Thomas-Fermi theory is its inability to explain the shell structure of atoms.

[6] A comparison between DFT and Green's functions many-body theories has been presented by [46].

For *weakly correlated* systems the first two features of Σ are not predominant and V_{SCF} provides a good approximation: firstly, the eigenvalues ε_n in Eq. 2.6 can be considered as a reasonable approximation to the electronic quasi-particles energy E_n, at least for band-structure calculations[7]. Secondly, V_{SCF} can be used to calculate the vibrational properties of the crystal and the perturbation of the electronic system due to lattice thermal vibrations, as summarized in the following sections.

To conclude, the solution of the Dyson equation via the design of meaningful approximations and practical implementations is a much more challenging task compared to DFT[8].

2.3 Density Functional Perturbation Theory for lattice vibrations

As mentioned at the beginning of this chapter, the vibrational properties of the crystal cannot be neglected in any first-principles approach to transport. The reason for this is that the interactions between charge carriers and lattice vibrations are ubiquitous and often the principal resistivity source in a multitude of systems, such as metals and lightly-doped semiconductors. Below, the first-principles lattice treatment adopted in this work is briefly reviewed.

The theoretical description of the dynamics of crystal lattice in solid state physics is based on the decoupling of the electronic and lattice degrees of freedom of Born and Oppenheimer [50], named the *adiabatic approximation*[9]. This approximation can be summarized in two steps[51]. Firstly, the wave-function of the total system is decomposed in a product of the electrons' and nuclei's according to the original Born and Oppenheimer [50] ansatz,

$$\Psi_{tot} = \Psi_e(\{\boldsymbol{r}_i\};\{\boldsymbol{R}_I\})\Psi_N(\{\boldsymbol{R}_I\}). \tag{2.14}$$

where Ψ_e is the GS electron wave-function and depends on electrons' coordinates $\{\boldsymbol{r}\}$, and parametrically on the ions' coordinates $\{\boldsymbol{R}_I\}$, while Ψ_N is the nucleus wave-function and depends on nuclei's coordinates $\{\boldsymbol{R}_I\}$. Secondly, the total Hamiltonian is expanded in the

[7] DFT commonly gives really poor estimation of insulators' band gap so that if both valence and conduction bands have to be used, the most trivial solution is to apply a *scissor operator* to shift the energy gap based on correct values.

[8] One of the most popular many-body approaches goes under the name of GW, proposed by Hedin [48] and named after the diagrammatic approximation of the screened Coulomb interaction. An implementation was proposed by van Schilfgaarde et al. [49]

[9] The physical intuition here is that the ions are slow and heavy so that they do not feel the short time-scale variations of the electron-nucleus interaction, and conversely electrons are not excited by the nuclei's motion.

small parameter m_e/m_I [52], with m_e and m_I being the electron's and ion's mass respectively, so that the effect of the nuclei's kinetic operator on electrons are neglected. Physically, this means that electrons follows the configuration of the nuclei adiabatically, always being in the GS. The result of these two assumptions is that the ions' dynamics is given by the following Schrödinger equation,

$$\left[-\sum_I \frac{\hbar^2}{2m_I}\nabla^2_{\boldsymbol{R}_I} + E_{BO}(\boldsymbol{R})\right]\Psi_N(\boldsymbol{R}) = \mathscr{E}_\lambda \Psi_N(\boldsymbol{R}). \tag{2.15}$$

$E_{BO}(\boldsymbol{R})$ is the *Born-Oppenheimer energy surface* and is given by the ground state energy of the interacting electrons moving in field of the nuclei with *fixed* configuration $\{\boldsymbol{R}_I\}$ [10]. $E_{BO}(\boldsymbol{R})$ is the expectation value of the adiabatic Hamiltonian,

$$\mathscr{H}_{BO} = -\frac{\hbar^2}{2m}\sum_i \nabla^2_{\boldsymbol{r}_i} + \frac{e^2}{2}\sum_{i\neq i'}\frac{1}{|\boldsymbol{r}_i - \boldsymbol{r}_{i'}|} - \sum_{iI}\frac{Z_I e^2}{|\boldsymbol{r}_i - \boldsymbol{R}_I|} + E_{\text{nuclei}}(\{\boldsymbol{R}_I\}), \tag{2.16}$$

where $E_{\text{nuclei}}(\{\boldsymbol{R}_I\})$ is the potential energy arising from the electrostatic interaction between nuclei of charge $Z_I e$.

Given Eq. 2.15, the forces acting on ion I become,

$$\boldsymbol{F}_I = -\frac{\partial E_{BO}(\boldsymbol{R})}{\partial \boldsymbol{R}_I}, \tag{2.17}$$

and are vanishing at ions' equilibrium positions. In the harmonic approximation, ions' motion consists of small oscillations around equilibrium positions, so that we can expand ionic coordinates as $\boldsymbol{R}_I = \boldsymbol{R}_I^{latt} + \boldsymbol{\nu}_I + \boldsymbol{d}_I$, where $\boldsymbol{R}_I^{latt}$ are the lattice cell coordinates of the cell of ion I, $\boldsymbol{\nu}_I$ is the equilibrium position of ion within the cell and $\boldsymbol{d}_I$ is the ion displacement around the equilibrium position. The second derivatives of the BO energy surface in $\boldsymbol{d}_I$ define the *inter-atomic force constants* matrix,

$$\mathscr{D}(\boldsymbol{R}_I, \boldsymbol{R}_J) \equiv \frac{\partial^2 E_{BO}(\boldsymbol{R})}{\partial \boldsymbol{d}_I \partial \boldsymbol{d}_J}. \tag{2.18}$$

Because of the lattice translational symmetry, $\mathscr{D}(\boldsymbol{R}_I - \boldsymbol{R}_J) = \mathscr{D}_{IJ}(\boldsymbol{R})$, with $\boldsymbol{R} = \boldsymbol{R}_I - \boldsymbol{R}_J$, and conveniently leads to the definition of the *dynamical matrix*,

$$\mathscr{D}_{IJ}(\boldsymbol{q}) = \sum_{\boldsymbol{R}} e^{-i\boldsymbol{q}\cdot\boldsymbol{R}}\frac{\mathscr{D}_{IJ}(\boldsymbol{R})}{\sqrt{m_I m_J}}. \tag{2.19}$$

[10] Another explicative name is the *clamped-ion* energy of the system.

that is the Fourier transform of the inter-atomic force constants. The eigenvalues, $\omega_\lambda^2(\boldsymbol{q})$ and eigenvectors, $\boldsymbol{e}^\lambda_{\boldsymbol{\nu}_I}(\boldsymbol{q})$ of $\mathscr{D}_{IJ}(\boldsymbol{q})$ define the normal modes of vibration of the crystal,

$$\mathscr{D}_{IJ}(\boldsymbol{q})\boldsymbol{e}^\lambda_{\boldsymbol{\nu}_J}(\boldsymbol{q}) = \omega^2_\lambda(\boldsymbol{q})\boldsymbol{e}^\lambda_{\boldsymbol{\nu}_J}(\boldsymbol{q}). \tag{2.20}$$

λ is the branch index in the reciprocal space: it is a cumulative index accounting for cartesian direction, α, of the displacement and ionic label within a cell, $\boldsymbol{\nu}_I$. Hence the collective vibrational modes of ions are labeled in the reciprocal space by $\lambda\boldsymbol{q}$, and in the adiabatic approximation form a gas of harmonic oscillators called *phonons*, that play a major role in both electronic and thermal transport of the solid state.

From the Hellmann [53] Feynman [54] theorem, the derivative of the expectation value E_{BO} in the ions' displacement is the expectation value of the $\mathscr{H}_{BO}$ derivative w.r.t. its parametric dependence on $\{\boldsymbol{R}_I\}$,

$$\boldsymbol{F}_I = -\frac{\partial E_{BO}(\boldsymbol{R})}{\partial \boldsymbol{R}_I} = -\left\langle \Psi(\boldsymbol{R}) \left| \frac{\partial \mathscr{H}_{BO}(\boldsymbol{R})}{\partial \boldsymbol{R}_I} \right| \Psi(\boldsymbol{R}) \right\rangle = -\int n_{\boldsymbol{R}}(\boldsymbol{r}) \frac{\partial V_{\boldsymbol{R}}(\boldsymbol{r})}{\partial \boldsymbol{R}_I} \mathrm{d}_3 r - \frac{\partial E_{\text{nuclei}}(\boldsymbol{R})}{\partial \boldsymbol{R}_I}, \tag{2.21}$$

where $V_{\boldsymbol{R}}(\boldsymbol{r}) = -\sum_{iI} \frac{Z_I e^2}{|\boldsymbol{r}_i - \boldsymbol{R}_I|}$ is the bare electron-nucleus Coulomb interaction and $n_{\boldsymbol{R}}$ is the electronic density in the ionic ocndiguration $\boldsymbol{R} = \{\boldsymbol{R}_I\}$. The second derivatives of E_{BO}, that define $\mathscr{D}(\boldsymbol{R}_I, \boldsymbol{R}_J)$ in Eq. 2.18 read,

$$\frac{\partial^2 E_{BO}(\boldsymbol{R})}{\partial \boldsymbol{R}_I \partial \boldsymbol{R}_{I'}} = \int \frac{\partial n_{\boldsymbol{R}}(\boldsymbol{r})}{\partial \boldsymbol{R}_{I'}} \frac{\partial V_{\boldsymbol{R}}(\boldsymbol{r})}{\partial \boldsymbol{R}_I} \mathrm{d}_3 r + \int n_{\boldsymbol{R}}(\boldsymbol{r}) \frac{\partial^2 V_{\boldsymbol{R}}(\boldsymbol{r})}{\partial \boldsymbol{R}_I \partial \boldsymbol{R}_{I'}} \mathrm{d}_3 r + \frac{\partial^2 E_{\text{nuclei}}(\boldsymbol{R})}{\partial \boldsymbol{R}_I \partial \boldsymbol{R}_{I'}}. \tag{2.22}$$

Eq. 2.22 states that the dynamical matrix elements require the calculation of the *linear response* of the electronic charge density to a distortion of the nuclear geometry[11].

Density Functional Perturbation Theory (DFPT) lays out an efficient theoretical framework to calculate the derivatives of $E_{BO}(\boldsymbol{R})$ [43] using a perturbative expansion in the ions displacements of V_{SCF}. Baroni et al. [56], Gonze [57] devised a self-consistent set of equations to calculate $\partial n_{\boldsymbol{R}}(\boldsymbol{r})/\partial \boldsymbol{R}_I$ [12]. Firstly, the derivative of $n_{\boldsymbol{R}}(\boldsymbol{r})$ can be linearized in the

[11] Another technique to calculate phonon frequency and, as discussed later, the electron-phonon coupling is the one of *frozen phonon*, as described by Lam and Cohen [55]. A comparison between DFPT and frozen phonon calculation is available in Ref. 43

[12] The numerical implementation of DFPT used in this work is the one of Giannozzi et al. [58], that follows the work of Baroni et al. [56]. The actual set of equations solved in the implementation of Ref. 58, is obtained from a further decomposition of the equations presented below, to account for numerical aspects that are discussed in Ref. 43.

finite-difference ion displacement [13], $\Delta \boldsymbol{R}_I$ (cft. Eq. 2.7),

$$\Delta n = 4 \quad \mathrm{Re} \sum_{i=1}^{N/2} \psi_i^* \Delta \psi_i. \tag{2.23}$$

where the imaginary part of the sum in Eq. 2.23 vanishes [43]. The perturbed Kohn-Sham orbital, $\Delta\psi$ can be calculated by standard first-order perturbation theory [59],

$$(\mathscr{H}_{SCF} - \varepsilon_i)\,|\Delta\psi_i\rangle = -\,(\Delta V_{SCF} - \Delta\varepsilon_i)\,|\psi_i\rangle\,. \tag{2.24}$$

The self-consistent Hamiltonian $\mathscr{H}_{SCF}$ comes from Eq. 2.6, leads to the definition of the perturbation of the self-consistent field potential as,

$$\Delta V_{SCF}(\boldsymbol{r}) = \Delta V(\boldsymbol{r}) + e^2 \int \frac{\Delta n(\boldsymbol{r}')}{|\boldsymbol{r} - \boldsymbol{r}'|} \mathrm{d}_3 r' + \frac{\mathrm{d}v_{xc}(n)}{\mathrm{d}n} \Delta n(\boldsymbol{r}), \tag{2.25}$$

togerther with the first order correction to the Kohn-Sham eigenvalue, $\Delta\varepsilon_i = \langle\psi_n|\Delta V_{SCF}|\psi_i\rangle$.

It is important to remark that Eq. 2.25 allows the calculation of the perturbation of V_{SCF} due to ions' displacement. Even though the self-consistent field refers to the auxiliary non-interacting system[14], ΔV_{SCF} represent the additional potential term felt by electron because of lattice vibrations, which is named *electron-phonon coupling* (EPC) [51].

2.4 Electron-phonon coupling from first principles

The last important element here discussed, is the first-principles description of the interaction between phonons and electrons.

The adiabatic approximation (cft. Sec. 2.3) is useful to get the crystal properties such as phonon dispersions, but has the major drawback of not allowing the motion of the nuclei to be the source of electronic excitations. This picture is rather a crude and has quite dramatic consequences on electronic transport: for example, it would exclude any resistive effect in the electric conduction in metals. The absence of electronic transition in the adiabatic approximation is the consequence of disregarding the effect of the nuclei's kinetic operators on the electronic wave-function, $-\hbar^2/2m_I \nabla^2_{\boldsymbol{R}}$. In fact, inspecting the off-diagonal matrix elements of the total Hamiltonian, $\mathscr{H}_{\mathrm{tot}} = \sum_I -\hbar^2/2m_I \nabla^2_{\boldsymbol{R}_I} + \mathscr{H}_{BO}$ (cft. Eq. 2.16) it is possible

[13] The finite difference operator in the set of parameters $\{\lambda_j\}$ of function f is defined as $\Delta^\lambda f = \sum_j \partial f_\lambda / \partial\lambda_j \Delta\lambda_j$ [43]

[14] See Par. 2.2.2 for a brief discussion of the physical meaning of V_{SCF}.

to see that the only non-vanishing terms are [51],

$$\left\langle \Psi'_N \left| \left\langle \Psi'_e \left| \frac{\hbar^2 \nabla^2_{\boldsymbol{R}}}{2m_I} \right| \Psi_e \right\rangle \right| \Psi_N \right\rangle, \tag{2.26}$$

$$\left\langle \Psi'_N \left| \frac{\hbar \nabla_{\boldsymbol{R}}}{\sqrt{2m_I}} \right| \Psi_N \right\rangle \left\langle \Psi'_e \left| \frac{\hbar \nabla_{\boldsymbol{R}}}{\sqrt{2m_I}} \right| \Psi_e \right\rangle, \tag{2.27}$$

which are, in fact, the *non-adiabatic* ones.

The first of these two expressions, Expr. 2.26 is usually neglected being of second order in the ion's displacement. The first factor in Expr. 2.27 is the vibrational mode of Ψ_N. The second factor is interpreted in perturbation theory [59] as the first order correction to the electronic GS arising from the ions' displacement. This term can thus be reformulated as an explicit additional interaction that adds to the electronic Hamiltonian [51],

$$\mathscr{H}_{\mathrm{e-ph}} = \sum_{iI} \left\langle \Psi'_N \left| \boldsymbol{d}(\boldsymbol{R}_I) \right| \Psi_N \right\rangle \left\langle \Psi'_e \left| \frac{\partial V_{\boldsymbol{R}}(\boldsymbol{r}_i)}{\partial \boldsymbol{R}_I} \right| \Psi_e \right\rangle, \tag{2.28}$$

where $\boldsymbol{d}(\boldsymbol{R}_I)$ is the displacement operator of ion I.

The simplest form of Eq. 2.28 comes from second quantization [60], which is used to model the electron-phonon interaction; the first factor is the matrix element of a normal mode of vibration $\boldsymbol{q}\lambda$ between harmonic crystal states, and reads [51],

$$\left\langle \Psi'_N \left| \boldsymbol{d}(\boldsymbol{R}_I) \right| \Psi_N \right\rangle = \sum_{\boldsymbol{q}\lambda} \sqrt{\frac{\hbar}{2\rho\,\omega^{\lambda}_{\mathrm{ph}}(\boldsymbol{q})}} \boldsymbol{e}^{\lambda} e^{i\boldsymbol{q}\cdot\boldsymbol{R}_I} \left\langle \Psi'_N \left| a_{\lambda\boldsymbol{q}} + a^{\dagger}_{\lambda-\boldsymbol{q}} \right| \Psi_N \right\rangle, \tag{2.29}$$

were ρ is the crystal mass density and $\boldsymbol{e}^{\lambda}$ is the polarization vector of the phonon branch λ. To clarify the notation, Ψ_N represents a state of the lattice populated by phonon modes $\{\lambda\boldsymbol{q}\}$ with number $n_{\lambda}(\boldsymbol{q})$. When the lattice is in equilibrium at temperature T, $n^0_{\lambda}(\boldsymbol{q})$ is the Bose-Einstein distribution. The annihilation (creation) operator, a ($a^{\dagger}$) in the matrix element in Eq. 2.29 gives the number of vibration quanta after the removal (addition) of a phonon in the vibrational mode $\lambda\boldsymbol{q}$ ($\lambda - \boldsymbol{q}$),

$$\left\langle \Psi'_N \left| a_{\lambda\boldsymbol{q}} + a^{\dagger}_{\lambda-\boldsymbol{q}} \right| \Psi_N \right\rangle = n_{\lambda}(\boldsymbol{q}) + [n_{\lambda}(-\boldsymbol{q}) + 1]. \tag{2.30}$$

The second factor in Eq. 2.28 is the perturbation of the electronic potential due to a lattice vibration. In this second quantization picture, the many-body state of the system is populated by electrons occupying Bloch states or Bloch Wave functions (BW), so that the one-particle

perturbation operator can be written as [60],

$$\left\langle \Psi'_e \left| \frac{\partial V_{\boldsymbol{R}}(\boldsymbol{r})}{\partial \boldsymbol{R}_I} \right| \Psi_e \right\rangle = \sum_{m\boldsymbol{k}m'\boldsymbol{k}'} \int e^{i(\boldsymbol{k}'-\boldsymbol{k})\cdot\boldsymbol{r}} \boldsymbol{u}^*_{m'\boldsymbol{k}'}(\boldsymbol{r}) \frac{\partial V_{\boldsymbol{R}}(\boldsymbol{r})}{\partial \boldsymbol{R}_I} \boldsymbol{u}_{m\boldsymbol{k}}(\boldsymbol{r}) \mathrm{d}_3 r \left\langle \Psi'_e \left| c^\dagger_{m'\boldsymbol{k}'} c_{m\boldsymbol{k}} \right| \Psi_e \right\rangle. \tag{2.31}$$

In the equation above, $\boldsymbol{u}_{m\boldsymbol{k}}(\boldsymbol{r})e^{-i\boldsymbol{k}\cdot\boldsymbol{r}}$ represents a BW, Ψ_e is a many-electron state populated with Bloch electrons $\{m\boldsymbol{k}\}$, $\boldsymbol{G}$ is a reciprocal lattice vector and c ($c^\dagger$) is the annihilation (creation) operator of a Bloch electron. Conservation of the crystal momentum implies $\boldsymbol{k}-\boldsymbol{k}'+\boldsymbol{q}=\boldsymbol{G}$.

The three equations just presented lead to the definition of the second-quantization electron-phonon Hamiltonian of Eq. 2.28 as,

$$\mathscr{H}_{e-ph} = \sum_{\boldsymbol{q}\lambda} \sum_{\boldsymbol{G}\boldsymbol{k}mm'} g^\lambda_{mm'}(\boldsymbol{G},\boldsymbol{k};\boldsymbol{q}) c^\dagger_{m'\boldsymbol{k}+\boldsymbol{q}+\boldsymbol{G}} c_{m\boldsymbol{k}} \left(a_{\lambda\boldsymbol{q}} + a^\dagger_{\lambda-\boldsymbol{q}} \right), \tag{2.32}$$

where the EPC function is defined as[15],

$$\begin{aligned} g^\lambda_{mm'}(\boldsymbol{G},\boldsymbol{k};\boldsymbol{q}) &= \sqrt{\frac{\hbar}{2\rho\omega^\lambda_{\mathrm{ph}}(\boldsymbol{q})}} \boldsymbol{e}^\lambda \int \psi^*_{m'\boldsymbol{k}+\boldsymbol{q}+\boldsymbol{G}}(\boldsymbol{r}) \frac{\partial V_{\boldsymbol{R}_I}(\boldsymbol{r}_i)}{\partial \boldsymbol{R}_I} \psi_{m\boldsymbol{k}}(\boldsymbol{r}) \mathrm{d}_3 r \\ &= \sqrt{\frac{\hbar}{2\rho\omega^\lambda_{\mathrm{ph}}(\boldsymbol{q})}} \left\langle \boldsymbol{u}_{m'\boldsymbol{k}+\boldsymbol{q}+\boldsymbol{G}} \left| \partial V^\lambda_{mm'}(\boldsymbol{k},\boldsymbol{k}+\boldsymbol{q}+\boldsymbol{G}) \right| \boldsymbol{u}_{m\boldsymbol{k}} \right\rangle. \end{aligned} \tag{2.33}$$

Within the DFT framework, it is possible to calculate the matrix element of the EPC in Eq. 2.33 by assuming that the Kohn-Sham orbitals, ψ of Eq. 2.6, are good approximation of BW and by considering that the derivative in the ion's displacement of V_{SCF}, as defined within DFPT in Eq. 2.25 is a good approximation of the disturbance induced in the physical electronic potential.

2.5 Wannier interpolation for electronic and vibrational properties, and electron-phonon coupling

In this first-principles approach to transport, the most time-consuming operation is the calculation of electrons' transition probability due to EPC. This calculation is well known to be computationally demanding. For this reason semi-empirical EPC models have been

[15]For further details regarding this derivation of the EPC function from the second-quantization of the phonon-perturbation operator, the reader should refer to Ref. 60.

developed in terms of EPC constants[61] that can be fitted from ab-initio calculations[16] on coarse k-point meshes [62] . Calculating EPCM elements on a basis of Wannier functions (WFs) is a computationally efficient way include first-principles EPC in electronic transport. More generally, interpolating WF and BW enables a remarkable speedup in the calculation of band structure, phonon dispersion and electron-phonon coupling on dense k-point grids.

WF are a legitimate basis set of complete, orthonormal functions and were introduced to provide a sound justification to tight-binding approaches [36]. First-principles WF can be calculated applying a unitary transformation to BW. Here the definition of WF in presented as direct space transformation of BW for a finite crystal[17],

$$|\boldsymbol{\nu}\boldsymbol{R}^{latt}\rangle = \sum_{m\boldsymbol{k}} |m\boldsymbol{k}\rangle \langle m\boldsymbol{k}|\boldsymbol{\nu}\boldsymbol{R}^{latt}\rangle = \frac{V}{(2\pi)^3}\sum_{m\boldsymbol{k}} e^{-i\boldsymbol{k}\cdot\boldsymbol{R}^{latt}} U_{\boldsymbol{\nu}m,\boldsymbol{k}}\,|m\boldsymbol{k}\rangle\,, \tag{2.34}$$

where $\boldsymbol{R}^{latt}$ is a direct lattice vector and $\boldsymbol{\nu}$ labels the WF within a cell. The arbitrariness in the choice of U comes from the definition of $|m\boldsymbol{k}\rangle$. BWs are the common eigenstate of the one-body effective crystal Hamiltonian, which in the DFT picture is $\hat{\mathscr{H}}_{SCF}$, defined on the left-hand side of Eq. 2.6, and the lattice translation operator, $\hat{T}_{\boldsymbol{R}^{latt}}$, and take the form,

$$\langle \boldsymbol{r}|m\boldsymbol{k}\rangle = e^{i\phi_m(\boldsymbol{k})} u_{m\boldsymbol{k}}(\boldsymbol{r}) e^{i\boldsymbol{k}\cdot\boldsymbol{r}}, \tag{2.35}$$

where $u_{m\boldsymbol{k}}(\boldsymbol{r})$ has the periodicity of the direct lattice. The factor $e^{i\phi_m(\boldsymbol{k})}$ in Eq. 2.35 represents the phase arbitrariness of the Schrödinger equation and is responsible for the freedom of choice of U. The inverse transformation of Eq. 2.34 reads,

$$|m\boldsymbol{k}\rangle = \frac{1}{N}\sum_{\boldsymbol{\nu}\boldsymbol{R}}^{latt} e^{i\boldsymbol{k}\cdot\boldsymbol{R}^{latt}} U^{\dagger}_{m\boldsymbol{\nu},\boldsymbol{k}}\,|\boldsymbol{\nu}\boldsymbol{R}^{latt}\rangle, \tag{2.36}$$

where N is the number of unit cells in the finite crystal.

A particularly convenient choice of transformation to construct WF from BW can be obtained by trying to maximize the localisation of WF, leading tp the Maximally Localized WF set (MLWF)[63]. The task is to set a localisation measure [64] and then to minimize it to obtain an explicit form of U. This is can be done by defining a spread functional, Ω,

$$\Omega \equiv \sum_{\boldsymbol{\nu}} \langle \boldsymbol{\nu}\boldsymbol{0}|\, r^2\, |\boldsymbol{\nu}\boldsymbol{0}\rangle - (\langle \boldsymbol{\nu}\boldsymbol{0}|\, \boldsymbol{r}\, |\boldsymbol{\nu}\boldsymbol{0}\rangle)^2\,. \tag{2.37}$$

[16] cft. App. B to see how deformation potential model can be fitted form first-principles calculation in the case of silicon.

[17] A finite crystal is made by a finite number of repetitions of the unit cell and is the system that is indeed considered in numerical calculations.

A software implementation that allows the calculation of MLWF basis set from a Plane Wave (PW) basis is `wannier90` [65]. The lattice version of the electronic MLWF is simply the Fourier transform of a vibrational eigenmode, defined in Eq. 2.20 referred to a single ionic displacement,

$$\langle \boldsymbol{\nu R} | \boldsymbol{q}\lambda \rangle = \sum_{\boldsymbol{\nu' R'}^{latt}} e^{i\boldsymbol{q}\cdot\boldsymbol{R}_I'^{latt}} \boldsymbol{e}^{\lambda}_{\boldsymbol{\nu'}}(\boldsymbol{q}) \delta(\boldsymbol{\nu'} - \boldsymbol{\nu}) \delta(\boldsymbol{R'} - \boldsymbol{R}). \tag{2.38}$$

MLWFs provide a very accurate and convenient tight-binding basis set for electronic structure calculations. This occurs thanks to their localization [63]: MLWFs decay rapidly in a super-cell of the direct crystal lattice as function of $\boldsymbol{R}^{latt}$. To exploit this aspect from a computational point of view, it is possible to devise an interpolation scheme from BW to WF and then back to BW to reduce the computational cost of first-principles transport calculations; as a matter of fact, Wannier interpolation is the key element to achieve precise electronic transport predictions with a fully first-principles EPC. Giustino et al. [66] provided a specific case of such a procedure for the calculation of ε, $\hbar\omega_{\mathrm{ph}}$ and most importantly g. Once the Wannier representation of the desired operators has been computed, it is possible to get back to their Bloch representation on an arbitrary $m\boldsymbol{k}$ point. $\mathscr{H}_{SCF}$ is diagonal on the Bloch/Kohn-Sham basis set, so that

$$\varepsilon_{m\boldsymbol{k}} = \sum_{\boldsymbol{\nu\nu' R}^{latt}} e^{i\boldsymbol{k}\cdot\boldsymbol{R}^{latt}} U_{m\boldsymbol{\nu'k}} \left\langle \boldsymbol{\nu' 0} \right| \mathscr{H}_{SCF} \left| \boldsymbol{\nu R}^{latt} \right\rangle U^{\dagger}_{\boldsymbol{\nu}m\boldsymbol{k}}, \tag{2.39}$$

and the same is true for phonon frequencies,

$$\omega^2_{\lambda\boldsymbol{q}} = \frac{1}{N} \sum_{\boldsymbol{\nu\nu' R}^{latt}} e^{i\boldsymbol{q}\cdot\boldsymbol{R}^{latt}} \boldsymbol{e}^{\lambda}_{\boldsymbol{\nu}}(\boldsymbol{q})^{\dagger} \left\langle \boldsymbol{\nu 0} \right| \mathscr{D} \left| \boldsymbol{\nu' R}^{latt} \right\rangle \boldsymbol{e}^{\lambda}_{\boldsymbol{\nu'}}(\boldsymbol{q}). \tag{2.40}$$

The core aspect of the Wannier interpolation is the calculation of the matrices $U_{\boldsymbol{\nu}m,\boldsymbol{k}}$ and $\boldsymbol{e}^{\lambda}_{\boldsymbol{\nu}}(\boldsymbol{q})$, which are the ones that diagonalise the Wannier representation of the operators $\mathscr{H}_{SCF}$ and $\mathscr{D}$ in the reciprocal space. The Wannier interpolation scheme can be interestingly applied to the EPC, enabling the use of first-principles electron phonon interaction in an exact BT framework. The EPC interpolation requires only the calculation pf U and $\boldsymbol{e}$, once the Wannier representation of $\partial_{\boldsymbol{\nu R}^{latt}} V$ has been obtained. To explicitly write down the interpolation formula, the definition of the perturbation of the self-consistent field potential due to a phonon has to be written in its contributions from each ion displacement [66],

$$\partial_{\lambda\boldsymbol{q}} V_{SCF}(\boldsymbol{r}) = \mathrm{Re}\left[\sum_{\boldsymbol{\nu R}^{latt}} e^{i\boldsymbol{q}\cdot\boldsymbol{R}^{latt}} \boldsymbol{e}^{\lambda}_{\boldsymbol{\nu}}(\boldsymbol{q}) \left(\frac{m_0}{m_{\boldsymbol{\nu}}} \right)^{\frac{1}{2}} \partial_{\boldsymbol{\nu R}^{latt}} V_{SCF}(\boldsymbol{r}) \right], \tag{2.41}$$

where the term on the right-hand side can be naturally called *phonon perturbation in the Wannier representation* [66]. The combination of Eq. 2.41, 2.36 leads to the explicit formula of the Wannier interpolation of the EPC matrix element and consequently of the EPC coupling function, Eq. 2.33 [66],

$$\left\langle m'\boldsymbol{k}+\boldsymbol{q}\left|\partial_{\lambda\boldsymbol{q}}V_{SCF}\right|m\boldsymbol{k}\right\rangle = \frac{1}{N^2}\sum_{\boldsymbol{\nu}\boldsymbol{\nu}'\boldsymbol{\nu}''\boldsymbol{R}^{latt}\boldsymbol{R}''^{latt}} e^{i\left(\boldsymbol{k}\cdot\boldsymbol{R}^{latt}+\boldsymbol{q}\cdot\boldsymbol{R}''^{latt}\right)} \times U^{\dagger}_{m'\boldsymbol{\nu}',\boldsymbol{k}+\boldsymbol{q}}\left\langle \boldsymbol{\nu}'\boldsymbol{0}\left|\partial_{\boldsymbol{\nu}''\boldsymbol{R}''^{latt}}V_{SCF}\right|\boldsymbol{\nu}\boldsymbol{R}^{latt}\right\rangle U_{\boldsymbol{\nu}m,\boldsymbol{k}}\left(\boldsymbol{e}^{\lambda}_{\boldsymbol{\nu}''}(\boldsymbol{q})\frac{m_0}{m_{\boldsymbol{\nu}''}}\right)^{-1}. \quad (2.42)$$

Eq. 2.39, 2.40 and 2.42 define the *Wannier interpolation* scheme. Noffsinger et al. [67] implemented such scheme by the use of MLWF, and has been used to obtain the results presented in this work, specifically to calculate the three key quantities $\varepsilon_m(\boldsymbol{k})$, $\hbar\omega_\lambda(\boldsymbol{q})$ and $g^{\lambda}_{mm'}(\boldsymbol{k};\boldsymbol{q})$ necessary to solve the BE with first-principles EPC on very dense $\boldsymbol{k}$-space meshes.

It is worth to notice that one of the benefits of Wannier representation is that matrix elements depend on the distance between cells by construction. The concept of maximal localization can be clarified in these terms: the matrix elements of the quantities of interest on the MLWF basis exhibit the most rapid decay at the increase of the distance $\|\boldsymbol{0}-\boldsymbol{R}_{latt}\|$ compared to other possible choices of WF basis. In particular, the matrix elements show an exponential decay outside the Wigner-Seitz cell[18]. Also, it turns out that electronic structure calculation on the MLWF basis requires smaller reciprocal-space meshes to converge compared to calculations on PW basis (see App. C). For these reasons, it is evident that the Wannier representation is very efficient in terms of computational resources.

[18] Plots of the spatial dependence of MLWF in the relevant case of Boron-doped Diamond are shown in [66] in App. C.3

Chapter 3

Semi-classical transport theory

In this chapter, the main ingredients of BT in linear response are discussed. The definition of current density is given as an ensemble average in Sec. 3.1. Then, the linear response transport coefficients linking the external perturbing fields, namely homogeneous electric fields and temperature gradients, to the charge and heat current densities are defined according to the Onsager theory in Sec. 3.2. In this framework, transport coefficients are calculated as an average over the electronic distribution function in the reciprocal space, and this latter function is calculated by solving the BE, as shown in Sec. 3.3. In the case of weak external perturbation, the assumption of a linear response of the system is valid and the BE can be linearized, as discussed in Sec. 3.3.2. The scattering events that affect transport are defined by the electronic transition probabilities, which represent the core part of the BE, and are discussed in Sec. 3.4. In presence of a thermal gradient, not only electrons but also phonons are driven out of equilibrium: the Seebeck effect is particularly sensitive to the presence of out-of-equilibrium phonons: they give rise to *phonon drag* that is discussed in detail in Sec. 3.5. Finally, some simplified approaches that avoid the solution of the BE are mentioned in Sec. 3.6.1 to provide a mean of comparison with methods that are popular in the electronic transport literature.

3.1 Current density

In a continuum, what links an observable with its current is the continuity equation, which can be written for every conserved quantity. The conservation law for a generic quantity O in absence of sources reads,

$$\frac{\mathrm{d}}{\mathrm{dt}} \int_{\Omega} d_3 x n_O(\boldsymbol{x}) = \int_S dS n_O(\boldsymbol{x}) \boldsymbol{v}(\boldsymbol{x}) \cdot \hat{\boldsymbol{s}}(\boldsymbol{x}), \tag{3.1}$$

where $\boldsymbol{x}$ is the position, n_O is the spatial density of quantity O, $\boldsymbol{v}$ is the velocity field of the medium in which O is embedded, Ω is the volume of space considered, S is the volume's boundary surface and $\hat{\boldsymbol{s}}$ is the unit vector that points to the outward normal direction to the surface. The important quantity here is the one defined in the right-hand side integral of Eq. 3.1, named *current density*,

$$\boldsymbol{J}_O(\boldsymbol{x}) \equiv n_O(\boldsymbol{x})\boldsymbol{v}(\boldsymbol{x}). \tag{3.2}$$

To increase the level of accuracy in this description, let us think of the medium as a thermodynamically large ensemble of particles. The dynamics of a particle system is described as formulated by W. R. Hamilton (1833). Every macroscopic field defined earlier is in fact an average over the microscopic particle dynamics. For example, the macroscopic particle density $n(\boldsymbol{x},t)$ could be calculated from the positions of the particles $\{\boldsymbol{q}_i(\boldsymbol{x},t)\}$ averaged over a macroscopically small space-time interval around a certain space-time point $(\boldsymbol{x},t)$.

The bridge between mechanics and thermodynamics has been established with the ensemble approach by J. W. Gibbs (1902): if the system is at equilibrium, the ensemble approach allows to calculate all the observables as averages over the particle distribution in the states' space. A classical example of the application of this paradigm shift is the calculation of the average kinetic energy of a perfect gas by means of the Boltzmann distribution (1868). The soundness of this proceeding relies on the ergodic assumption and the Poincaré theorem but, in the classical realm, its validity mostly remains supported by unambiguous evidence[68].

In the ensemble framework, the central quantity of an N-particle system is the *N-body distribution function* or density function. In Hamiltonian mechanics, the N-body distribution function depends on the $6N$ canonical coordinates, $\{\boldsymbol{q}_i, \boldsymbol{p}_i\}$ that uniquely define the physical state of the N-particle system at time t. The N-body distribution function is the only quantity needed for the calculation of all observables, defined as ensemble averages, and thus defines the system's macrostate. This function proves challenging to calculate because of its obvious degree of complexity. Nevertheless, the quantities that are relevant in semi-classical transport do not depend explicitly on the correlation between 2 to N bodies and can be regarded as single-particle observables. Additionally, if it is assumed that the system is at the steady state, the microscopic dynamics will not affect the temporal dependence of the macroscopic scale, that will be stationary.

In fact, electronic transport deals with the low-lying, weakly-interacting charge carriers' excitations in a thin layer around the Fermi surface. The electronic quasi-particles behave similarly to a diluted gas of classical, neutral particles, as briefly discussed in Sec. 2.1: to

explicitly calculate any observable, only the steady-state, 1-body distribution function, is needed. This function is often called just the *distribution function*, f, and can be defined as,

$$N \equiv \int_{\Lambda} d\alpha f(\alpha), \tag{3.3}$$

where Λ is the set of all available 1-particle states, α refers to one of such states and N is the number of particles in the system.

It is now possible to give the definition of current density for the observable O as an ensemble average,

$$\boldsymbol{J}_O \equiv \int_{\Lambda} d\alpha f(\alpha) n_O(\alpha) \boldsymbol{v}(\alpha), \tag{3.4}$$

where, n_O is the observable O density per state. In this work, the focus is posed on charge and heat transport by electrons. The two associated currents densities can be calculated by referring to the density per states. Let's label an electronic state using the band index and crystal momentum, $\alpha \to m\boldsymbol{k}$. The number of electronic states for each $m\boldsymbol{k}$ point is given from the Born-Von Karman periodic boundary condition as equal to [36] $2/(2\pi)^3$ [1]. The amount of electric charge in each state is simply,

$$n_{em}(\boldsymbol{k}) = -\frac{e}{4\pi^3}, \tag{3.5}$$

where μ is the chemical potential. The microscopic change in heat is defined by the first law of thermodynamics, $\delta Q = \mathrm{d}U - \mu \mathrm{d}N$. It follows that the heat dissipation per electronic state reads [36],

$$n_{Qm}(\boldsymbol{k}) = \frac{1}{4\pi^3}(\varepsilon_m(\boldsymbol{k}) - \mu). \tag{3.6}$$

Inserting the definitions of charge density and heat density per $m\boldsymbol{k}$-state Eq. 3.5, 3.6, in the general definition of ensemble current density Eq. 3.4, the formula of the corresponding currents in term of the electronic distribution function, $f_m(\boldsymbol{k})$ reads,

$$\boldsymbol{J}_e = -\frac{e}{4\pi^3} \sum_m \int_{BZ} f_m(\boldsymbol{k}) \boldsymbol{v}_m(\boldsymbol{k}) \mathrm{d}_3 k, \tag{3.7a}$$

$$\boldsymbol{J}_Q = \frac{1}{4\pi^3} \sum_m \int_{BZ} [\varepsilon_m(\boldsymbol{k}) - \mu] f_m(\boldsymbol{k}) \boldsymbol{v}_m(\boldsymbol{k}) \mathrm{d}_3 k. \tag{3.7b}$$

In this work, the steady-state distribution function, $f_m(\boldsymbol{k})$ is calculated by solving exactly the BE in linear response, as will be explained with all the necessary details in Sec. 3.3.

[1] Here it is assumed that transport does not depend on spin, meaning that neither transition probabilities nor observable quantities distinguish between spin up or down.

3.2 The Onsager relations and linear response

In an isolated system at equilibrium, macroscopic observables are time-independent and current densities are absent. If the system is then coupled to external fields this is often no more the case. It is reasonable to suppose that after a short transient period of time, the applied fields will eventually drive the system to a steady state. In this case, meaningful observables such as rates of change and densities are time independent but currents are non-zero: this is the most common setting of *irreversible thermodynamics*, which is the theoretical framework that leads to the definition of the transport coefficients.

Since currents are absent at equilibrium, it is reasonable to postulate that they have linear dependence on the external perturbations in the weak coupling regime. The Kelvin (1854) and Onsager relations (1931) are one of the theoretical milestones of non equilibrium thermodynamics[69] because they draw a link between the various, distinct phenomena that define thermoelectricity in solid state physics [70, 36]. The linear response assumption has obvious advantages: it is straightforward to point out the system's intrinsic transport properties, since all the information are collected in the *kinetic coefficients*, L_{ij}, that relate flows to external fields,

$$\boldsymbol{J}_i = L_{ij}\boldsymbol{X}_j. \tag{3.8}$$

L_{ij} is a tensor in the spatial (implicit) indexes. Its L_{ij} component is the kinetic coefficient that relates the i-th current density, $\boldsymbol{J}_i$, to the j-th external perturbation, $\boldsymbol{X}_j$, that is known as *driving force*. To correctly identify the kinetic coefficient we have to define firstly a transport setting e.g. to fix driving forces, $\boldsymbol{X}_j$, and fluxes, $\boldsymbol{J}_i$. These two sets of quantities are conjugate in the sense that the instantaneous entropy production is unchanged for any possible legitimate choice of forces and fluxes [71],

$$\dot{S} = \sum_i \boldsymbol{X}_i \cdot \boldsymbol{J}_i. \tag{3.9}$$

which is derived from the continuity equation of entropy $\dot{S} = \frac{\partial S}{\partial t} + \nabla \cdot \boldsymbol{J}_S = \Sigma_i \boldsymbol{X}_i \cdot \boldsymbol{J}_i$. The consistency of this formulation can be tested by deducting the fluxes that maximize the entropy production for given forces (the *maximum entropy production principle*), or vice versa, with the constraint that the Onsager relations in Eq. 3.8 are valid. One of the many possible choice in presence of a temperature gradient, a concentration gradient leading to a chemical potential gradient, $\nabla\mu$, and an electric field is [60],

$$\dot{S} = \frac{1}{T}\left\{\left(\boldsymbol{E} - \frac{\nabla\mu}{e}\right)\cdot\boldsymbol{J}_e - \left(\frac{\nabla T}{T}\right)\cdot\boldsymbol{J}_\varepsilon\right\}, \tag{3.10}$$

in which case the driving forces are the electrochemical potential, $\mathscr{E} = -\nabla_{\boldsymbol{r}}(\phi + \mu/e)$ (with ϕ being the electric potential) and minus the temperature gradient over the temperature, $-\nabla_{\boldsymbol{r}}T/T$. Neglecting spatial variations of μ, we can write down the following linear-response equations,

$$\boldsymbol{J}_e = L_{11}\boldsymbol{E} + L_{12}\left(-\frac{\nabla_{\boldsymbol{r}}T}{T}\right), \tag{3.11a}$$

$$\boldsymbol{J}_\varepsilon = L_{21}\boldsymbol{E} + L_{22}\left(-\frac{\nabla_{\boldsymbol{r}}T}{T}\right). \tag{3.11b}$$

In this work, the kinetic coefficients are calculated exactly from the solution of the Linearised BE (LBE)[2]. From the four kinetic coefficients of Eq. 3.11, it is possible to calculate all the other quantities that together define the thermoelectric properties of a system. These quantities have clear empirical definitions in term of observables (voltage and temperature differences) so that their calculations once the current densities are obtained is unambiguous. In the case of purely electric transport we have *electric conductivity*, σ_e, *electric resistivity*, ρ_e, and *electron mobility*, μ_e (hole mobility, μ_h),

$$\sigma_e = L_{11}, \tag{3.12}$$

$$\rho_e = \frac{1}{\sigma_e}, \tag{3.13}$$

$$\mu_e = \frac{\sigma_e}{en}. \tag{3.14}$$

Thermal transport of the electronic system is given by the heat flow at open circuit, that defines the *thermal conductivity* of the electrons k_e,

$$k_e = L_{22} - L_{21}\frac{L_{12}}{L_{11}}. \tag{3.15}$$

The off-diagonal kinetic coefficients define the reversible conversion between heat and charge fluxes in linear response and lead to the definition of Seebeck coefficient, S and Peltier coefficient, Π,

$$S = \frac{L_{12}}{L_{11}}, \tag{3.16}$$

$$\Pi = \frac{L_{21}}{L_{11}}. \tag{3.17}$$

[2]The expression of the kinetic coefficient in therm of the solution of the LBE will be given in Sec. 3.3.2.

Π and S are the transport coefficients that characterize the *thermoelectric* response of the system. These two effects are linked through the second Thomson relation[3] [36],

$$\Pi = TS. \tag{3.18}$$

Theoretically, this is the direct result of the identity $L_{21} = TL_{12}$, and will be a subject for discussion in Silicon, in Sec. 6.2.5, in the presence of a non-equilibrium phonon population.

As a last quantity, it is possible to mention the *Lorenz number L*, that establishes a relation between electric and thermal conductivities of the electrons,

$$L = \frac{k_e}{\sigma_e T} = \frac{L_{22}}{L_{11}T} - L_{21}\frac{L_{12}}{(L_{11})^2 T} = \frac{L_{22}}{\sigma_e T} - S^2. \tag{3.19}$$

L was first highlighted in the Wiedmann-Franz law that prescribes a constant value of $L = (\pi k_B/\sqrt{3}e)^2 = 2.44 \times 10^{-8}$ WΩK^{-2} in physical systems that exhibit a free-electron-like behavior, such as elemental metals.

3.3 Boltzmann equation

The BE was conceived to calculate the distribution function of distinguishable, weakly interacting particles. Before applying BE to electronic transport, it is important to stress two fundamental observations linking the electronic ensemble to a classical diluted gas. Firstly, wave packets can be regarded as distinguishable particles if the average spacing between two neighbours is larger than the de Broglie wavelength e.g. $\hbar/\sqrt{2m_c K_B T}n^{-1/3} \gg 1$, so that the quantum aspects becomes negligible on a macroscopic scale. Secondly, particles are diluted if their spatial density, n is small compared to the typical interaction range, R e.g. $nR^3 \ll 1$ [35]. For the reasons discussed in Sec. 2.1, the emerging quasi-particle picture of elemental metals and semiconductors studied in this work complies with these assumptions, leading to a transport picture that is accurately described by BT.

3.3.1 Derivation

The BE can be derived at least in two ways that give an insight on as many features[72] of this transport framework. The first derivation gives a physically sound reason of the fact that only the one-body distribution function affects the kinetic of a system of diluted particles,

[3] Also known as Kelvin relation after the name of its first discoverer.

and is presented in App. A. The other provides an intuitive explanation of the structure of the BE based on physical principles and is presented below.

Conservation of the number of particles

Below, the normalization condition for the distribution function on a Bravais lattice is given (cft. Eq. 3.3),

$$N \equiv \int_{\Lambda} \mathrm{d}\alpha f(\alpha) = \sum_{m} \int_{V_{BZ}} \mathrm{d}_3 k \frac{V}{8\pi^3} f_m(\boldsymbol{k}), \tag{3.20}$$

being Λ the 1-body state space, α the particle state label, N the number of particles in the Wigner-Seitz cell and V, the volume of the same cell, and V_{BZ} is the Brillouin zone volume.

Consider now the number of bodies in a small volume of Λ around $(\boldsymbol{q},\boldsymbol{p})$ at time t, $\mathrm{d}N(\boldsymbol{q},\boldsymbol{p};t) = f(\boldsymbol{q},\boldsymbol{p};t)\mathrm{d}_3 q\mathrm{d}_3 p$. At time $t+\delta t$, this small bunch of particles will evolve to $\mathrm{d}N'(\boldsymbol{q}',\boldsymbol{p}';t+\delta t) = f(\boldsymbol{q}',\boldsymbol{p}';t+\delta t)\mathrm{d}_3 q\mathrm{d}_3 p$. Within the semi-classical dynamics induced by the external perturbations and because of the Liouville theorem [36], the particles $\mathrm{d}N'$ at time $t+\delta t$ are exactly the ones of $\mathrm{d}N$ at time t. This fact can be formalized with the following equation,

$$f(\boldsymbol{q}+\boldsymbol{v}\delta t, \boldsymbol{p}+\boldsymbol{F}\delta t; t+\delta t)\mathrm{d}_3 q\mathrm{d}_3 p = f(\boldsymbol{q},\boldsymbol{p};t)\mathrm{d}_3 q\mathrm{d}_3 p, \tag{3.21}$$

that is correct if the diffusion of particles in the Λ space is driven by the semi-classical dynamics only.

The BE describes the evolution of the 1-body distribution function under the *combined effect* of the semi-classical dynamics induced by external, macroscopic perturbation, and scattering of particles due to interactions with other bodies, also dubbed *collisions*. The effect of collisions is summarised by an electronic transition probability. In App. A, the case of 2-body collisions is mentioned, but since the electronic quasi-particles responsible for transport can be assumed as non-interacting, the focus here is on one-body collisions $\boldsymbol{q},\boldsymbol{p} \to \boldsymbol{q}',\boldsymbol{p}'$. In a crystal, for example, there are phonons, impurities, excitons, plasmons *et cetera* that will affect electrons' dynamics. In practical implementations of BT, scatterers' kinetics is often regarded as decoupled from carriers'[4]. This approximation is valid whenever it is sound to assume that scatterers relax to their prescribed distribution function on a much shorter time-scale than carriers.

On a general footing, all the aforementioned scattering phenomena add a term to the right-hand side of Eq. 3.21, that composes the scattering kernel of the BE; it accounts for the number of particles that join the group $\mathrm{d}N$, δN_+, due to a collision, minus the ones

[4]Despite this, scatterers distribution function is not necessary the equilibrium one as it will be discussed in Sec. 3.5. This has interesting effects on transport, as shown in Chap. 6.

that fail to get there, δN_{-}[36], for the same cause. As a whole, this number is defined as $\delta N \equiv \left(\frac{\delta f}{\delta t}\right)_{coll} \mathrm{d}_3 q \mathrm{d}_3 p \delta t$. With a small re-arrangement, equation Eq .3.21 becomes,

$$f(\boldsymbol{q}+\boldsymbol{v}\delta t, \boldsymbol{p}+\boldsymbol{F}\delta t; t+\delta t) - f(\boldsymbol{q},\boldsymbol{p};t) = \left(\frac{\delta f}{\delta t}\right)_{coll} \delta t. \tag{3.22}$$

For the applications that pertain this work, let's consider an homogeneous system made by the repetition of a single unitary cell: a perfect crystal. As already mentioned in Sec. 3.1, the electronic states are labeled by their band and wave-vector $m\boldsymbol{k}$ and have a density of states in the wave-vector space, without taking spin into account, that is $1/(2\pi)^3$. If the finite time-step is taken to zero, the left-hand side of Eq. 3.22 becomes proportional to the total time-derivative of the distribution function, which is,

$$\frac{\mathrm{d}f}{\mathrm{d}t} = \frac{\partial f}{\partial t} + \boldsymbol{v}\cdot\nabla_{\boldsymbol{q}}(f) + \boldsymbol{F}\cdot\nabla_{\boldsymbol{p}}(f) = \frac{\partial f}{\partial t} + (\mathscr{L} f), \tag{3.23}$$

where $\mathscr{L}$ is the Liouville operator, $\mathscr{L} \equiv \Sigma_{i=1}^{N}[\frac{\partial \mathscr{H}}{\partial p_i}\frac{\partial}{\partial q_i} - \frac{\partial \mathscr{H}}{\partial q_i}\frac{\partial}{\partial p_i}]$, with the Hamiltonian defined in Eq. A.2. The collision term is,

$$\left(\frac{\delta f}{\delta t}\right)_{coll} = \frac{V}{(8\pi^3)}\sum_m \int_{BZ} \mathrm{d}_3 k' f_m(\boldsymbol{k}') P_{m'\boldsymbol{k}'\to m\boldsymbol{k}} - \frac{V}{(8\pi^3)}\sum_m \int_{BZ} \mathrm{d}_3 k' f_m(\boldsymbol{k}) P_{m\boldsymbol{k}\to m'\boldsymbol{k}'}, \tag{3.24}$$

being $P_{m\boldsymbol{k}\to m'\boldsymbol{k}'}$ the transition probability. The first term on the right-hand side is δN_{+}, while the other is δN_{-}. As a remark, this form of the collision term is correct even for half-integer spin particles with non-spin-flipping collisions.

In all the condensed matter applications, the transition probability has a quantum-mechanical nature: to this level of approximation, it is needed just to the first order in the interaction potential, meaning that it can be calculated through the Fermi golden rule. In particular, for a fermionic system the Pauli exclusion principle plays a fundamental role, so that the first order transition probability becomes,

$$P_{m\boldsymbol{k}\to m'\boldsymbol{k}'} = \frac{2\pi}{\hbar}\left|\langle m'\boldsymbol{k}'|\, U\,|m\boldsymbol{k}\rangle\right|^2 \delta(E-E')\left[1-f_{m'}(\boldsymbol{k}')\right]. \tag{3.25}$$

Now that all the fundamental concepts have been laid down, if Eq. 3.23 is combined with Eq. 3.24, the Boltzmann transport equation can be finally written,

$$\frac{\partial f}{\partial t} + (\mathscr{L} f) = -\left(\frac{\delta f}{\delta t}\right)_{coll}. \tag{3.26}$$

The physical interpretation is clear. On the left-hand side there is the change in the distribution function due to the semi-classical dynamics imposed by the external perturbations that has to be balanced, on the right-hand side by the variation due to collisions, which depends on the distribution function itself.

3.3.2 Linearisation

Let's consider an homogeneous systems under the action of a uniform weak, quasi-static electric field, $\boldsymbol{E}$, and temperature gradient, ∇T. Because of $\boldsymbol{E}$, f acquires temporal dependence through the crystal momentum, $\boldsymbol{k}$, due to the induced semi-classical dynamics[36],

$$\begin{cases} \dot{\boldsymbol{v}} &= \frac{1}{\hbar}\nabla_{\boldsymbol{k}}\varepsilon(\boldsymbol{k}), \\ \hbar\dot{\boldsymbol{k}} &= -e\boldsymbol{E}. \end{cases} \tag{3.27}$$

In addition, the temperature has a spatial dependence because of the thermal gradient, $T = T_0 + \nabla_{\boldsymbol{r}} T x$ so that f also acquires a spatial dependence along the x-axis, in this case.

At this point, it is useful to introduce the concept of *relaxation time*, τ. Intuitively, it could be argued that, on average, $\boldsymbol{k}$ is displaced by the electric field by an amount equal to $\delta\boldsymbol{k} \sim -e/\hbar\boldsymbol{E}\tau$. Also, electrons will tend, on average, to equilibrate the local temperature at a rate given by $\delta T/\tau \sim \nabla_{\boldsymbol{r}} T \cdot \boldsymbol{v}$ [70]. In this simplistic and qualitative picture, which is nevertheless ubiquitous in the electronic transport literature[70], τ represent the average time between two thermalizing collisions[5]. In this work, I will go beyond this simple representation of an average or constant relaxation time and calculate $\tau_m(\boldsymbol{k})$ by solving exactly the linearised BE.

Having introduced the semi-classical dynamics and $\tau_m(\boldsymbol{k})$, it is now possible to proceed with the linerisation of the BE.

Explicit form of the steady-state quasi-particles distribution function.

On a general basis, the steady state distribution function, $f_m(\boldsymbol{k})$, depends on the external driving forces in some non-trivial manner. Starting from the observation that at equilibrium, quasi-particles bands are occupied according to the Fermi-Dirac distribution, it seems reasonable to suppose the steady state distribution function can be calculated, in linear response, by

[5] A relaxation time can also be introduced make a correspondence with effective electronic scattering rates, $1/\tau$ and then calculate the transport coefficients of Sec. 3.2 without solving the transport equation: this popular approach is called Relaxation Time Approximation (RTA) and will be introduced formally in Sec. 3.6.1.

adding a correction to the equilibrium one,

$$f_m(\boldsymbol{k}) = f_m^0(\boldsymbol{k}) - \delta f_m(\boldsymbol{k}). \tag{3.28}$$

In this chapter, it is assumed by definition that the correction to the equilibrium distribution, $\delta f_m(\boldsymbol{k})$, is linear in the perturbing fields. $\delta f_m(\boldsymbol{k})$ can be refined further as,

$$\delta f_m(\boldsymbol{k}) \equiv \frac{\partial f_m^0(\boldsymbol{k})}{\partial \varepsilon} \chi_m(\boldsymbol{k}), \tag{3.29}$$

where $\chi_m(\boldsymbol{k})$ is the unknown function that is calculated solving the BE. Inspired from but not restricted to the concept of relaxation time (cft. Sec. 3.3.2, 3.6.1),

$$\chi_m(\boldsymbol{k}) = -\boldsymbol{v}_{m\boldsymbol{k}} \cdot \left[\boldsymbol{E} e \tau^E{}_m(\boldsymbol{k}) + \frac{\nabla_{\boldsymbol{r}} T}{T} \left(\varepsilon_{m\boldsymbol{k}} - \mu\right) \tau^T{}_m(\boldsymbol{k}) \right] \tag{3.30}$$

without loss of generality from Eq. 3.29. The two functions, $\tau_m^E(\boldsymbol{k})$ and $\tau_m^T(\boldsymbol{k})$ are the output of the BE (see Eq. 3.46) in the presence of an electric field and thermal gradient, respectively. Their reciprocal can be used to define an effective scattering rate for a charge carrier in the state $m\boldsymbol{k}$. $\tau_m^E(\boldsymbol{k})$ and $\tau_m^T(\boldsymbol{k})$ are the solutions of a linear system under the action of $\boldsymbol{E}$ and ∇T, respectively, meaning that the total solution of the LBE $\chi_m(\boldsymbol{k})$ of Eq. 3.30, is the sum of the two solutions,

$$\chi_m^E(\boldsymbol{k}) = -e\boldsymbol{E} \cdot \boldsymbol{v}_m(\boldsymbol{k}) \tau_m^E(\boldsymbol{k}), \tag{3.31a}$$

$$\chi_m^T(\boldsymbol{k}) = -\nabla_{\boldsymbol{r}} T \cdot \boldsymbol{v}_m(\boldsymbol{k}) \frac{\left[\varepsilon_m(\boldsymbol{k}) - \mu\right]}{T} \tau_m^T(\boldsymbol{k}). \tag{3.31b}$$

Notice that the τ^E, τ^T defined above are different from the ones that will be defined in RTA (discussed in Sec. 3.6.1), as they are the exact solutions of the LBE. This notation is just due to the fact the have the units of time. In terms of these solutions of the LBE, τ^E and τ^T, the kinetic coefficients L_{ij} of Sec. 3.2 have the following form,

$$L_{11} = -\frac{e^2}{4\pi^3} \sum_m \int_{BZ} \mathrm{d}_3 k \frac{\partial f_m^0(\boldsymbol{k})}{\partial \varepsilon} \left[\frac{\boldsymbol{v}_m(\boldsymbol{k}) \cdot \boldsymbol{E}}{|\boldsymbol{E}|} \right]^2 \tau_m^E(\boldsymbol{k}), \tag{3.32a}$$

$$L_{12} = \frac{e}{4\pi^3 T} \sum_m \int_{BZ} \mathrm{d}_3 k \frac{\partial f_m^0(\boldsymbol{k})}{\partial \varepsilon} \left[\frac{\boldsymbol{v}_m(\boldsymbol{k}) \cdot \nabla_{\boldsymbol{r}} T}{|\nabla_{\boldsymbol{r}} T|} \right]^2 \left[\varepsilon_m(\boldsymbol{k}) - \mu\right] \tau_m^T(\boldsymbol{k}), \tag{3.32b}$$

$$L_{21} = \frac{e}{4\pi^3} \sum_m \int_{BZ} \mathrm{d}_3 k \frac{\partial f_m^0(\boldsymbol{k})}{\partial \varepsilon} \left[\frac{\boldsymbol{v}_m(\boldsymbol{k}) \cdot \boldsymbol{E}}{|\boldsymbol{E}|} \right]^2 \left[\varepsilon_m(\boldsymbol{k}) - \mu\right] \tau_m^E(\boldsymbol{k}), \tag{3.32c}$$

$$L_{22} = -\frac{1}{4\pi^3 T}\sum_m \int_{BZ} \mathrm{d}_3 k \frac{\partial f_m^0(\boldsymbol{k})}{\partial \varepsilon}\left[\frac{\boldsymbol{v}_m(\boldsymbol{k})\cdot\nabla_{\boldsymbol{r}} T}{|\nabla_{\boldsymbol{r}} T|}\right]^2 [\varepsilon_m(\boldsymbol{k})-\mu]^2 \tau_m^T(\boldsymbol{k}). \tag{3.32d}$$

Driving forces term

At this point, the task of linearising the left-hand side of the BE, Eq. 3.26 is straightforward.

From the discussion presented at the beginning of Sec. 3.3.2, the two differential operators on the left-hand side of the BE, Eq. 3.23 are proportional to external perturbations. For the term in which the position is differentiated, it is clear that $\frac{d}{d\boldsymbol{r}} = \frac{\partial T}{\partial \boldsymbol{r}}\frac{\partial}{\partial T}$ is of first order in the temperature gradient. It also is immediate to recognize the force, proportional to the electric field, in the term arsing from the wave-vector differentiation. The result is that, in the left-hand side of equation Eq. 3.26, only the Fermi-Dirac distribution, f^0 will be differentiated. In fact, δf depends by definition on the external perturbations: explicitly, $\mathscr{L}(f^0-\delta f) = \mathscr{L}(f_0) + o(E) + o(\nabla T)$ [6], so that the left-hand side becomes

$$\mathscr{L}(f_0) = -\frac{\partial f_0(\boldsymbol{k})}{\partial \varepsilon}\bigg|\boldsymbol{v}(\boldsymbol{k})\left\{\boldsymbol{E}e + \nabla_r T\frac{\left[\varepsilon(\boldsymbol{k})-\mu\right]}{T}\right\}, \tag{3.33}$$

where T indicates the equilibrium temperature. In Eq. 3.33 a possible, explicit dependence on time has been excluded because of the assumption that the system is at the steady-state. Similarly to Eq. 3.30, Eq. 3.33 is the result of the sum of the contributions from the two driving forces,

$$X_m^{\boldsymbol{E}}(\boldsymbol{k}) = -e\boldsymbol{E}\cdot\boldsymbol{v}_m(\boldsymbol{k})\frac{\partial f_m^0(\boldsymbol{k})}{\partial \varepsilon} \tag{3.34}$$

$$X_m^{T}(\boldsymbol{k}) = -\nabla_{\boldsymbol{r}} T\cdot\boldsymbol{v}_m(\boldsymbol{k})\frac{\partial f_m^0(\boldsymbol{k})}{\partial \varepsilon}\frac{[\varepsilon_m(\boldsymbol{k})-\mu]}{T} \tag{3.35}$$

Collision integral

Once it has been clarified that δf has a first-order dependence on $\boldsymbol{X}$ (see Eq. 3.30), the linearised form of the collision integral is found by plugging the definition $f = f^0 - \delta f$ into the integrand of Eq. 3.24.

The first step is accomplished by expanding the definition of f, Eq. 3.29,

$$\delta f_m(\boldsymbol{k}) = \frac{\partial f_m^0(\boldsymbol{k})}{\partial \varepsilon}\chi_m(\boldsymbol{k}) = -\beta f_m^0(\boldsymbol{k})\left[1-f_m^0(\boldsymbol{k})\right]\chi_m(\boldsymbol{k}), \tag{3.36}$$

[6] $o(X)$ means small "o" and indicates terms of higher order in X, that can then be neglected.

with $\beta = 1/(k_B T)$. Because of the principle of *detailed balance*,

$$f^0_{m'}(\boldsymbol{k}')P_{m\boldsymbol{k}'\to m\boldsymbol{k}}\left[1-f^0_m(\boldsymbol{k})\right] = f^0_m(\boldsymbol{k})P_{m\boldsymbol{k}\to m'\boldsymbol{k}'}\left[1-f^0_{m'}(\boldsymbol{k}')\right], \tag{3.37}$$

terms that depends on f^0 only in the collision integral cancel out. Eq. 3.37 is the mathematical formalization of the physical intuition for which currents are absent at equilibrium. With the definition of the number of transition per unit time at equilibrium,

$$\Pi^0_{m\boldsymbol{k},n'\boldsymbol{k}'} = f^0_m(\boldsymbol{k})P_{m\boldsymbol{k}\to m'\boldsymbol{k}'}[1-f^0_m(\boldsymbol{k}')], \tag{3.38}$$

the final form of the linearised collision integral is the following,

$$\begin{aligned}
&\frac{V}{(2\pi)^3}\beta\sum_{m'}\int_{BZ}\mathrm{d}_3k' f^0_m(\boldsymbol{k})P_{m\boldsymbol{k}\to m'\boldsymbol{k}'}[1-f^0_m(\boldsymbol{k}')]\left[\chi_{m'}(\boldsymbol{k}')-\chi_m(\boldsymbol{k})\right]) = \\
&\qquad = \beta\frac{V}{(2\pi)^3}\sum_{m'}\int_{BZ}\mathrm{d}_3k'\Pi^0_{m\boldsymbol{k},m'\boldsymbol{k}'}\left[\chi_{m'}(\boldsymbol{k}')-\chi_{m'}(\boldsymbol{k})\right] = \\
&= \frac{V}{(2\pi)^3}\beta\sum_{m'}\int_{BZ}\mathrm{d}_3k'\left\{\Pi^0_{m\boldsymbol{k},m'\boldsymbol{k}'}-\delta^3(\boldsymbol{k}-\boldsymbol{k}')\sum_n\int_{BZ}\mathrm{d}_3q\Pi^0_{n\boldsymbol{q},m\boldsymbol{k}'}\right\}\chi_{m'}(\boldsymbol{k}'),
\end{aligned} \tag{3.39}$$

where the linear dependence on the unknown function χ, and consequently on the external perturbation, is explicit.

To make this equation more compact, it is possible to define the integral kernel $\mathscr{C}_{m\boldsymbol{k},m'\boldsymbol{k}'}$ as proportional to the terms inside of the curly brackets[7],

$$\mathscr{C}_{m\boldsymbol{k},m'\boldsymbol{k}'} \equiv -\beta\left[\Pi^0_{m\boldsymbol{k},m'\boldsymbol{k}'}-\delta^3(\boldsymbol{k}-\boldsymbol{k}')\sum_n\int_{BZ}d_3q\Pi^0_{n\boldsymbol{q},m\boldsymbol{k}'}\right]. \tag{3.40}$$

In numerical application, the Brillouin zone is discretized on a k-point mesh, and $\mathscr{C}$ becomes effectively a matrix, called the *collision matrix* (CM). $\mathscr{C}$ in Eq. 3.40 can be decomposed as the sum of two matrices,

$$\mathscr{C} \equiv -\mathscr{C}^{in}+\mathscr{C}^{out}, \tag{3.41}$$

$$\mathscr{C}^{in}_{m\boldsymbol{k},m'\boldsymbol{k}'} \equiv \Pi^0_{m\boldsymbol{k},m'\boldsymbol{k}'}-\delta_{m'm}\delta(\boldsymbol{k}'-\boldsymbol{k})\Pi^0_{m\boldsymbol{k},m'\boldsymbol{k}'}, \tag{3.42}$$

$$\mathscr{C}^{out}_{m\boldsymbol{k},m'\boldsymbol{k}'} \equiv \delta_{m'm}\delta(\boldsymbol{k}'-\boldsymbol{k})\left[\Pi^0_{m\boldsymbol{k},m'\boldsymbol{k}'}-\sum_{m''\boldsymbol{q}}\Pi^0_{n\boldsymbol{q},m'\boldsymbol{k}'}\right]. \tag{3.43}$$

[7]Notice that in the formalism presented here, both sides of BE have been multiplied by -1

It is evident from (3.43) that $\mathscr{C}^{out}$ has just its diagonal terms that are non null and conversely that $\mathscr{C}^{in}$ has a zero diagonal, implying that,

$$\mathscr{C}_{m\boldsymbol{k},m'\boldsymbol{k}'} = -\mathscr{C}^{in}_{m\boldsymbol{k},m'\boldsymbol{k}'} \quad \forall m,\boldsymbol{k} \neq m',\boldsymbol{k}', \tag{3.44}$$

$$\text{diag}\left[\mathscr{C}_{m\boldsymbol{k},m'\boldsymbol{k}'}\right] = \mathscr{C}^{out}_{m\boldsymbol{k},m'\boldsymbol{k}'} = \text{diag}\left[\mathscr{C}^{out}_{m\boldsymbol{k},m'\boldsymbol{k}'}\right]. \tag{3.45}$$

From a physical point of view, remembering the derivation of the BE in section (3.3.1), $\mathscr{C}^{in}$ takes into account the re-population of state $m\boldsymbol{k}$ and contributes with the off-diagonal entries, while $\mathscr{C}^{out}$ adds the collision kernel diagonal, which physically represent depopulation of $m\boldsymbol{k}$.

3.3.3 Linearised BE

Combining Eq. 3.33 and 3.39 in 3.26, it possible to write the LBE,

$$-\frac{\partial f^0_m(\boldsymbol{k})}{\partial \varepsilon}\boldsymbol{v}_{m\boldsymbol{k}} \cdot \left[\boldsymbol{E}e + \frac{\nabla_{\boldsymbol{r}} T}{T}\left(\varepsilon_{m\boldsymbol{k}} - \mu\right)\right] = \frac{V}{(2\pi)^3}\sum_{m'}\int_{BZ} d_3k' \mathscr{C}_{m\boldsymbol{k},m'\boldsymbol{k}'}\chi_{m'}(\boldsymbol{k}'). \tag{3.46}$$

Solving Eq. 3.46 in $\chi_m(\boldsymbol{k})$, allows the calculation of the transport coefficient discussed in Sec. 3.2, via Eq. 3.32 and the solution of the transport problem in the linear regime.

General remarks

Properties of the linearised collisions kernel The collision kernel posseses some interesting properties that it is useful to underline. They are the consequence of two mathematical features of Π^0: the first attribute is that $P_{m\boldsymbol{k}\to m\boldsymbol{k}'} \geq 0$ for all $m\boldsymbol{k}, m'\boldsymbol{k}'$ and the other is that the transition probabilities per unit time, $P_{m\boldsymbol{k}\to m\boldsymbol{k}'}$ are in detailed balance with the Fermi-Dirac distribution, f_0 as for Eq. 3.37. These basic requirements lead to these two other properties of the collision kernel: firstly it can be seen that $\mathscr{C}$ is *symmetric* upon interchange between $m\boldsymbol{k}$ and $m'\boldsymbol{k}'$, which can be readily verified from the identity Eq. 3.40 or with some algebra, by reformulating the first member of Eq. 3.39 as follows,

$$\langle\varphi|\mathscr{C}|\phi\rangle \equiv \int \mathrm{d}_3k\mathrm{d}_3k'\,\varphi_{\boldsymbol{k}}\mathscr{C}_{\boldsymbol{k}\boldsymbol{k}'}\phi_{\boldsymbol{k}'} = \frac{1}{2}\int \mathrm{d}_3k\mathrm{d}_3k'(\varphi_{\boldsymbol{k}} - \varphi_{\boldsymbol{k}'})\Pi^0_{\boldsymbol{k}\boldsymbol{k}'}(\phi_{\boldsymbol{k}} - \phi_{\boldsymbol{k}'}) \tag{3.47}$$

which is manifestly symmetric. The second is that the collision kernel is *semi-positive definite*, which means that for every function $\phi_{\boldsymbol{k}} \neq 0$ this inequality,

$$\langle \phi | \mathscr{C} | \phi \rangle \geq 0 \tag{3.48}$$

holds. This property can be checked against Eq. 3.47 and by noticing that the integral kernel satisfies this sum rule:

$$\langle \mathbf{1} | \mathscr{C} | \mathbf{1} \rangle = \int_{BZ} \mathrm{d}_3 k \mathrm{d}_3 k' \mathscr{C}_{\boldsymbol{k}\boldsymbol{k}'} = 0. \tag{3.49}$$

The corresponding null eigenvector is indeed,

$$|\mathbf{1}\rangle = \boldsymbol{u}_{\text{null}}, \quad u_m^{\text{null}}(\boldsymbol{k}) = 1 \quad \forall m, \boldsymbol{k}. \tag{3.50}$$

The resulting CM has columns (or rows) that are not linearly independent and it is a fact that will be taken into account in the discussion of the numerical solution of LBE in Sec. 4.4.

Conservation laws of the BE As physically expected, the BE in its full, non-linear form of Eq. 3.26 embodies the physical conservation laws. For classical, isotropic, short-ranged, two-body interactions, this can be readily verified for the desired conserved quantity. If both sides are multiplied by 1, $\boldsymbol{k}$ or $\varepsilon_m(\boldsymbol{k})$ and then integrated in $m\boldsymbol{k}$, the corresponding continuity equations are found [73]: the continuity equation is in fact equal to the integrated l.h.s while the integrated collision kernel, vanishes.

On a more general footing, the principle reads: *for every quantity*, O *that is conserved in the transition*, $m\boldsymbol{k} \rightarrow m'\boldsymbol{k}'$, *a continuity equation for that quantity can be written in the form*,

$$\sum_m \int \mathrm{d}_3 k O_m(\boldsymbol{k}) \frac{\mathrm{d} f_m(\boldsymbol{k})}{\mathrm{d}t} = \sum_m \int \mathrm{d}_3 k O_m(\boldsymbol{k}) \left[\frac{\delta f_m(\boldsymbol{k})}{\delta t} \right]_{coll}. \tag{3.51}$$

The class of transitions that this paper focuses on, as put forward in the introductory section e.g. the ones due to electron-phonon coupling, do not conserve neither energy nor momentum of the electronic system alone, but just the number of particles, so that this last one is the only conserved quantity.

3.4 Electron scattering mechanisms

The physical entities that define the microscopic details of electronic transport are the transition probabilities per unit time, inside the collision kernel $\mathscr{C}$ on the right-hand side of

Eq. 3.46. It is a common approach to write these transition probabilities to the first order in the interaction potential using the Fermi golden rule[8],

$$P_{m\boldsymbol{k}\to m'\boldsymbol{k}'} = \frac{2\pi}{\hbar} \left\langle u_{m'\boldsymbol{k}'} \left| \mathscr{H}_{\text{pert.}} \right| u_{m\boldsymbol{k}} \right\rangle \delta \left[\varepsilon_{m'}(\boldsymbol{k}') - \varepsilon_m(\boldsymbol{k}) \right]. \tag{3.52}$$

In the following paragraphs, the most important sources of electronic scattering for doped-semiconductors[9] and metals are reported. Notably, also the impact on electronic transport of non-equilibrium phonon effects[75] is considered from first-principles and is discussed in Par. 3.5.

3.4.1 Phonon scattering

In Sec. 2.4 the calculation of the EPC matrix element was derived from first principles. The transition probability between Bloch states is simply [60],

$$\begin{aligned} \left| \langle m\boldsymbol{k} | \mathscr{H}_{\text{el-ph}} | m'\boldsymbol{k}+\boldsymbol{q} \rangle \right|^2 &= \sum_{\lambda} \frac{\hbar}{2\rho V_{\text{pc}} \omega_\lambda(\boldsymbol{q})} \\ &\times \left| \langle m\boldsymbol{k} | \partial_{\lambda \boldsymbol{q}} V | m'\boldsymbol{k}+\boldsymbol{q} \rangle \right|^2 \{ n_\lambda(\boldsymbol{q}) + [n_\lambda(-\boldsymbol{q})+1] \} \\ &= \sum_{\lambda} \left[g^{\lambda}_{mm'}(\boldsymbol{k};\boldsymbol{q}) \right]^2 \{ n_\lambda(\boldsymbol{q}) + [n_\lambda(-\boldsymbol{q})+1] \}, \end{aligned} \tag{3.53}$$

where $n_\lambda(\boldsymbol{q})$ is the full, non-equilibrium phonon population, and $g^{\lambda}_{mm'}(\boldsymbol{k};\boldsymbol{q})$ is equivalent to $g^{\lambda}_{mm'}(\boldsymbol{G}=0,\boldsymbol{k};\boldsymbol{q})$ which is the EPC function defined in Eq. 2.33, with λ being the phonon branch and $\boldsymbol{q}$ the phonon wave-vector. Writing down the above expression, we have explicitly taken into account that the electronic transition from $m\boldsymbol{k}$ to $m'\boldsymbol{k}+\boldsymbol{q}$ takes place in both the cases of absorption and emission of a phonon in the state $\lambda\boldsymbol{q}$ or $\lambda-\boldsymbol{q}$, respectively.

The calculation of $n_\lambda(\boldsymbol{q})$ represents a task that, in many respects, is similar to the problem of calculating the steady-state electronic distribution in presence of external perturbations. The BT picture that is being applied to electrons is also valid for phonons. Indeed phonon transport and thermal resistivity phenomena can be described microscopically from phonon

[8] The notation $|u_{m\boldsymbol{k}}\rangle$ has been chosen because electronic quasi-particles in periodic crystals are best described by Bloch functions.

[9] The electron-plasmon interaction, which is relevant in semiconductors near the degenerate regime was not considered here. Semi-empirical models have been developed and applied in the past[74], but the presence of adjustable parameters would compromise the purpose of the approach presented in this work

scattering events [10]. This means that the steady-state phonon distribution in presence of a temperature difference can be calculated by solving the corresponding phonon BE [76]. The phonon population in the presence of the thermal gradient has the form,

$$n_\lambda(\boldsymbol{q}) = n^0_\lambda(\boldsymbol{q}) - \delta n_\lambda(\boldsymbol{q}). \tag{3.54}$$

where $n^0_\lambda(\boldsymbol{q})$ is the phonon population at equilibrium in the form of the Bose-Einstein distribution.

The effect of the EPC on the electronic system is twofold. Substituting Eq. 3.54 in Eq. 3.53, it is possible to recognize that n^0 is responsible for what is usually regarded as *diffusive scattering* of electrons by phonon and results in a transition probability in the scattering kernel of the BE. The out-of-equilibrium phonon population, δn adds a separate contribution to the BE and results in an additional driving force on the right-hand side of BE: this effect is called *phonon drag* and will be discussed separately in Sec. 3.5. The effect of diffusive phonon scattering is determined by the following transition probability per unit time,

$$\begin{aligned} P^{\text{diff}-\text{ph}}_{m\boldsymbol{k}\to m'\boldsymbol{k}+\boldsymbol{q}} = \frac{2\pi}{\hbar}\sum_\lambda \left[g^\lambda_{mm'}(\boldsymbol{k};\boldsymbol{q})\right]^2 \\ \times \left\{n^0_\lambda(\boldsymbol{q})\delta\left[\varepsilon_{m'\boldsymbol{k}+\boldsymbol{q}} - \varepsilon_{m\boldsymbol{k}} - \hbar\omega_\lambda(\boldsymbol{q})\right]\right. \\ \left. + \left[n^0_\lambda(\boldsymbol{q})+1\right]\delta\left[\varepsilon_{m'\boldsymbol{k}+\boldsymbol{q}} - \varepsilon_{m\boldsymbol{k}} + \hbar\omega_\lambda(\boldsymbol{q})\right]\right\}. \end{aligned} \tag{3.55}$$

In this first-principles approach described in Sec. 2.3 and 2.4, further assumptions on the details of the potential felt by electrons, V are not made, thus enabling the same treatment of intra-valley acoustic phonons, usually modelled with deformation potentials and inter-valley transition, for which the rigid-ion potential is commonly used[61].

3.4.2 Ionized impurities

A first-principles treatment of scattering between electrons and ionized impurities has been developed and applied in recent years[77, 78] and it surely is an important milestone for a complete, first-principles approach of transport in semiconductors. For this work, we decided to rely on an analytical approach instead that has been proved to be reliable in the temperature and doping concentration considered here[61]. Among all the possible choices[79, 80], it

[10] In the semiconducting system that have been studied in this work, the main phonon scattering processes are anharmonicities, which involve three-phonon processes and can be calculated from DFPT from third order derivatives and boundary scattering.

has been preferred the model of Brooks and Herring (1951) (BH) for its simplicity and effectiveness. The resulting transition probability per unit time is,

$$P^{\text{ion}-\text{imp}}_{m\boldsymbol{k}\to m'\boldsymbol{k}+\boldsymbol{q}} = \frac{2\pi Z^2 n_i e^4}{\hbar V_{ws}(\varepsilon_r\varepsilon_0)^2}\frac{\delta\left(\varepsilon_{m'\boldsymbol{k}+\boldsymbol{q}}-\varepsilon_{m\boldsymbol{k}}\right)}{\left({\beta_s}^2+|\boldsymbol{q}|^2\right)^2}, \tag{3.56}$$

where Z is the number of charge quantum in each impurity, n_i is the impurity density, ε_r and ε_0 are the relative and the vacuum permittivity.

The reciprocal of the screening length, β_s is what defines the BH model,

$$\beta_s = \sqrt{\frac{e^2 n_i}{\varepsilon_r\varepsilon_0 k_B T}}. \tag{3.57}$$

This model is also referred to as the Debye screening length [81] and presents a picture in which all the elementary charges in the conduction bands compose a degenerate, free electron gas that screens the perturbing potential of the ionized impurity [11].

3.4.3 Neutral impurities

In semiconductors, the interaction of charge carriers with a neutral impurity can be model as a case of elastic electron scattering by neutral hydrogen-like center [82]. Here the path of Meyer and Bartoli [83] is followed, where the the scattering cross section of neutral impurities is obtained from phase-shift calculations,

$$\sigma_{\text{ni}}(\omega) = \frac{A(\omega)a_0}{|\mathbf{k}|} \tag{3.58}$$

$$A(\omega) \equiv \frac{35.2}{\sqrt{\omega}}\frac{(1+e^{-50\omega})(1+80.6\omega+13.7\omega^2)}{1+41.3\omega+133\omega^2}\left[\frac{\ln(1+\omega)}{\omega}-\frac{1+\omega/2-\omega^2/6}{(1+\omega)^3}\right], \tag{3.59}$$

where $\omega \equiv {(\varepsilon_m(\boldsymbol{k})-\varepsilon_{vt})}/{E_a}$, E_a is the activation energy of the implanted impurities, ε_{tv} is the top of the valence band, and $a_0 = \frac{\hbar k}{m_{h,dos}e^2}$ is the Bohr radius of the neutral impurity scattering centre and $m_{h,dos}$ is the hole density of state mass. The resulting total scattering rate per incident electron becomes [84],

$$\frac{1}{\tau_{\text{ni}}(m\boldsymbol{k})} = \frac{\hbar|\mathbf{k}|}{m_{h,dos}}\sigma_{\text{ni}}n_{\text{ni}}, \tag{3.60}$$

[11] Needless to say, in the degenerate regime the impurity scattering is overscreened by the BH model. Electron-plasmon interaction, as well as other screening effects on band structure and electron-phonon coupling, become important.

where $n_{\rm ni} = n_{d/a} - n_{e/h}$ is the density of neutral impurities, $n_{d/a}$ is the density of donors/acceptors and $n_{e/h}$ is the density of electrons/holes.

This model has been successfully applied to doped semiconductors in the case of Silicon [83], Germanium[85] and Diamond[86] (see Chap. 7 for a detailed study of electronic transport in Diamond). Eq. 3.60 can be used to add the effects of neutral impurities to $\mathscr{C}$ in a relaxation-time approximation picture as it will be shown in Eq. 3.70.

3.5 Phonon drag

In the presence of a thermal gradient, the phonon drag effect adds up to the diffusive effect (see Sec. 3.4.1) and originates from the steady-state correction to the equilibrium phonon population in presence of a temperature gradient[12]. From a physical point of view, phonon drag is responsible for the enhancement of some thermoelectric phenomena, notably the Seebeck effect, particularly at low temperatures in many semiconducting systems. Large Seebeck coefficients at low temperatures were observed decades ago in covalent-bond semiconductors such as Ge[87], Si[88] and Diamond[89], and have been imputed to phonon-drag, which can add to S a contribution orders of magnitude larger than the diffusive effect[75]. This interesting effect in Si will be discussed in detail in Chap. 6, where it will be shown how it can be exploited as a path to enhance thermoelectric performance [90, 27]. Below, is presented a theoretical approach within BT to treat phonon drag in linear response.

3.5.1 Decoupling phonons from electrons

In general, thermoelectric phenomena are by definition the result of the coupling between the electronic and vibrational, degrees of freedom. In BT, electron and phonon kinetics in presence of a thermal gradient is coupled in the pair of BE,

$$\boldsymbol{v}_m(\boldsymbol{k}) \cdot \nabla_{\boldsymbol{r}} T \frac{\partial f_m(\boldsymbol{k})}{\partial T} = \left(\frac{\delta f_m(\boldsymbol{k})}{\delta t} \right)_{\rm coll}, \tag{3.61a}$$

$$\boldsymbol{c}_\lambda(\boldsymbol{q}) \cdot \nabla_{\boldsymbol{r}} T \frac{\partial n_\lambda(\boldsymbol{q})}{\partial T} = \left(\frac{\delta n_\lambda(\boldsymbol{q})}{\delta t} \right)_{\rm coll}, \tag{3.61b}$$

[12] Phonons' contribution to thermal transport is in fact the most important in semiconductors, while plays a smaller role in metals at low temperatures.

where $\boldsymbol{c}_\lambda = \nabla_{\boldsymbol{q}}\omega_\lambda$ is the phonon group-velocities. Eq. 3.61 have to be solved to calculate the steady-state electron and phonon populations, $f_m(\boldsymbol{k})$ (see Eq. 3.30), and $n_\lambda(\boldsymbol{q})$, that is one-body distribution function for the phonon branch λ and phonon wave-vector $\boldsymbol{q}$.

Eq 3.61a and Eq. 3.61b are coupled because of the transition probability arising from the electron-phonon interaction, Eq. 3.53, in the collision integral in their right-hand sides. Nevertheless, the most important phonon scattering sources are anharmonicities, isotopic disorder and sample's boundaries [76], while at high doping levels also scattering with impurities and charge carriers at equilibrium becomes important [27, 75]. Following these considerations, it is sensible to decouple the two equations by just retaining anharmonic effects in the scattering kernel of the phonons BE[13]. This implies that Eq. 3.61b can be solved standalone and then the resulting steady-state phonon population, $n_\lambda(\boldsymbol{q})$ inserted in the collision integral of the electronic BE Eq. 3.61a, to calculate $\chi_m^T(\boldsymbol{k})$ of Eq. 3.31b. Similarly to the electronic case of Eq. 3.30, the steady-state phonon population can be defined as,

$$n_\lambda(\boldsymbol{q}) = n_\lambda^0(\boldsymbol{q}) - \delta n_\lambda(\boldsymbol{q}), \tag{3.62a}$$

$$\delta n_\lambda(\boldsymbol{q}) \equiv -\tau_\lambda(\boldsymbol{q})\frac{\boldsymbol{c}_\lambda(\boldsymbol{q})\cdot\nabla_{\boldsymbol{r}}T}{k_B T^2}\hbar\omega_\lambda(\boldsymbol{q})n_\lambda^0(\boldsymbol{q})\left[n_\lambda^0(\boldsymbol{q})+1\right] \tag{3.62b}$$

where $\tau_\lambda(\boldsymbol{q})$ is the effective phonon relaxation time. The anharmonic phonon lifetimes $\tau_\lambda(\boldsymbol{q})$ can be calculated for the purposes of this work in the Single Mode Relaxation Time Approximation (SMRTA) [14] from the third order force constants[15]. Once $\tau_\lambda(\boldsymbol{q})$ is calculated, it possible to take into account the phonon drag effect of steady-state phonon populations on the electronic system.

3.5.2 The *phonon drag* driving force

Since the steady state phonon population of Eq. 3.62 is linear in the thermal gradient by definition, the phonon drag scattering contribution will depend just on the equilibrium electronic distributions, in the current linear response setting. In fact, the action of the phonon

[13] The effect of this choice in Si will be discussed in Sec. 6.2.2

[14] See Sec. 3.6.1 for a discussion about approximated solution of the phonon LBE in the SMRTA, that is equivalent of the RTA for electrons.

[15] The procedure that was followed has been described in Ref. 91

drag is effectively equal to another driving force term in the direction of the thermal gradient,

$$\left(\frac{\delta f_m(\boldsymbol{k})}{\delta t}\right)_{\text{Ph drag}} = -\frac{V_{ws}}{2\pi^2\hbar k_B T}\sum_{m',\lambda}\int_{BZ} \mathrm{d}_3 q \left[g^{\lambda}_{mm'}(\boldsymbol{k};\boldsymbol{q})\right]^2 \times \left\{\delta n_\lambda(\boldsymbol{q})\delta\left[\varepsilon_{m'\boldsymbol{k}+\boldsymbol{q}} - \varepsilon_{m\boldsymbol{k}} - \hbar\omega_\lambda(\boldsymbol{q})\right] + \delta n_\lambda(-\boldsymbol{q})\delta\left[\varepsilon_{m'\boldsymbol{k}+\boldsymbol{q}} - \varepsilon_{m\boldsymbol{k}} + \hbar\omega_\lambda(\boldsymbol{q})\right]\right\} \times \left[f^0_{m'}(\boldsymbol{k}+\boldsymbol{q}) - f^0_m(\boldsymbol{k})\right]. \quad (3.63)$$

This has interesting implication in the definition of the transport framework discussed in Sec. 3.2 and on the resulting transport coefficient as will be discussed in Sec. 6.2.5.

3.6 Comparison with approximated methods

3.6.1 Relaxation time approximation

One of the most employed set of assumptions to avoid solving the BE goes under the name of *relaxation-time approximation* (RTA). It relies on two fundamental hypotheses, [36] that strictly define the role of collisions in the thermalisation process. The first is that the number of particles per phase-space unit volume immediately after a collision is equal to $f^0_m(\boldsymbol{k})/\tau_m(\boldsymbol{k})\delta t$, without any reference to the non-equilibrium distribution function prior to the scattering event. The second assumption states that collisions do not alter the equilibrium distribution f^0, as observations of the system at equilibrium suggest. As a result of the RTA, the rate of change of inbound particles in a unit volume of the phase space due to collision (which was labelled δN_+ in Sec. 3.3.1) is equal to $f^0_m(\boldsymbol{k})/\tau_m(\boldsymbol{k})$, while the rate of outbound particles (δN_-) is $f_m(\boldsymbol{k})/\tau_m(\boldsymbol{k})$. The effect of collisions in RTA simplifies to,

$$\left(\frac{\delta f_m(\boldsymbol{k})}{\delta t}\right)_{coll} \approx -\frac{f_m(\boldsymbol{k}) - f^0_m(\boldsymbol{k})}{\tau_m(\boldsymbol{k})}. \quad (3.64)$$

If this assumption is plugged into the LBE and compared to its right-hand side Eq. 3.33, δf takes the form,

$$\delta f_m(\boldsymbol{k}) = -\frac{\partial f^0_m(\boldsymbol{k})}{\partial\varepsilon}\boldsymbol{v}_m(\boldsymbol{k})\cdot\left\{\boldsymbol{E}e + \nabla_r T\frac{\left[\varepsilon_m(\boldsymbol{k}) - \mu\right]}{T_{eq}}\right\}\tau_m(\boldsymbol{k}). \quad (3.65)$$

Eq. 3.65 leads to the form of $\delta f = {}^{\partial f^0}/_{\partial \varepsilon}\chi$ of Eq. 3.29 that exposes some physical features of the the BE without the restraints of the RTA, such as the energy dependence of χ or the definition of effective relaxation times τ.

To clarify the origin of the name of the relaxation-time approximation, let's consider a situation where the system is in its steady-state and the external perturbations are suddenly removed; on the left-hand side of the LBE all the terms proportional to the fields disappear, but since we are in a transient situation, it is reasonable to suppose that an explicit time dependence is acquired by the distribution function. In this case, the BE takes the form,

$$\frac{\partial \delta f_m(\boldsymbol{k})}{\partial t} = -\frac{\delta f_m(\boldsymbol{k})}{\tau_m(\boldsymbol{k})} \tag{3.66}$$

and its solution gives the explicit form of the time-dependent distribution function,

$$\delta f(\boldsymbol{k};t) = \delta f(\boldsymbol{k};0) e^{-\frac{t}{\tau_m(\boldsymbol{k})}}. \tag{3.67}$$

The physical interpretation is unambiguous: τ sets the time scale on which the electronic system loses trace of the effect of the external perturbations and reaches the equilibrium.

Another path to get to the same result can be followed observing that, because of the semi-classical dynamics (cft. Sec. 3.3.2), the presence of weak, homogeneous $\boldsymbol{E}$, together with ∇T, result in a distortion of the Fermi-Dirac distribution with the occupations shifted in the direction of the perturbations [70]. It is then possible to postulate that the steady-state distribution function will resemble a distorted equilibrium one,

$$f \approx f^0(T_{eq} + \nabla T \cdot \boldsymbol{v}(\boldsymbol{k})\tau_{\nabla T}, \boldsymbol{k} - e\boldsymbol{E} \cdot \boldsymbol{v}\tau_E) \tag{3.68}$$

If Eq. 3.68 is expanded in the perturbing fields, the zeroth order contribution in the fields is the equilibrium distribution, f^0 and first order is equal to minus Eq. 3.65.

Solution of the BE within the Energy RTA

A way to reconnect the RTA with the formalism of Sec. 3.3 is to cast RTA assumptions on the collision kernel, where only $\mathscr{C}^{out}$ is retained (cft. Eq. 3.41). This simplification goes under the name of Energy RTA (ERTA) ans leads to the definition of τ^{ERTA},

$$\mathscr{C}_{m\boldsymbol{k},m'\boldsymbol{k}'} \approx \mathscr{C}^{out}_{m\boldsymbol{k},m'\boldsymbol{k}'} = \mathrm{diag}\left[\mathscr{C}_{m\boldsymbol{k},m'\boldsymbol{k}'}\right] \tag{3.69}$$

In this fashion, the relaxation time can be added to the collision matrix of the BE,

$$\mathscr{C}^{out} \approx \frac{f_m^0(\boldsymbol{k})\left[1-f_m^0(\boldsymbol{k})\right]}{\tau_m^{ERTA}(\boldsymbol{k})}. \tag{3.70}$$

Eq. 3.70 can be regarded as a definition of $\tau_m^{ERTA}(\boldsymbol{k})$ if the electronic transition probabilities are available, and thus $\mathscr{C}^{out}$ can be computed as defined in Eq. 3.43. This formalism is concise and effective and can be immediately applied also to phonon transport, where it goes under the name of *single mode relaxation time approximation* (SMRTA). This is a useful technique to calculate, for example, the steady state phonon population needed to incorporate phonon drag effects in electronic transport (cft. 3.63) [16]. For phonons the collision matrix has a different structure: the diagonal takes into account normal processes, while the out-of-diagonal entries represent *umklapp* [36] processes. On a general basis, SMRTA is reliable at room to high temperature and for $3D$ systems [17].

With this correspondence, it is possible to incorporate in the LBE the effect of scattering mechanism for which transition probabilities are not immediately available but scattering rates can be obtained [18], such as in the case of scattering due to neutral impurities[83], as mentioned in Sec. 3.4.3.

ERTA as a correct LBE solution We can push ERTA further by assuming that collisions are velocity-randomizing [92], that translates into the requirement for transition probabilities that,

$$P_{m\boldsymbol{k}\to m'\boldsymbol{k}'} = P_{m\boldsymbol{k}\to m'-\boldsymbol{k}'}. \tag{3.71}$$

This condition is true in particular for isotropic scattering, where the transition probability depends just on the energy of the final state and not on the direction of scattering. In this case, the dependence of τ on the electronic wave vector becomes implicit and the relaxation time depends on the electron's energy only,

$$\tau_m^{ERTA}(\boldsymbol{k}) \approx \tau^{ERTA}\left(\varepsilon_m(\boldsymbol{k})\right). \tag{3.72}$$

The simplification shown in Eq. 3.72 is responsible of the name of ERTA.

[16] In this work it was used to obtain the steady-state phonon population in Silicon

[17] These are just qualitative arguments. In fact, in the case of Diamond the LBE has to be solved for phonons to obtain good thermal conductivities as shown by Fugallo et al. [76]

[18] In phonon transport, this is a common approach for isotopic and boundary scattering[76].

As a result, it follows from Eq. 3.64 that,

$$\frac{1}{\tau_m^{ERTA}(\boldsymbol{k})} = \frac{V}{(2\pi)^3}\sum_{m'}\int_{BZ} P_{m\boldsymbol{k}\to m'\boldsymbol{k}'}\mathrm{d}_3k', \tag{3.73}$$

in analogy with the formulation presented in Eq. 3.69

Momentum RTA

In the case of elastic collisions, $\mathscr{C}$ reshuffles electrons within surfaces of constant energy. For spherical iso-energy surfaces [19], this implies that transition probabilities depend just on the length and the angle, θ, between the initial and final states wave-vectors,

$$P_{m\boldsymbol{k}\to m'\boldsymbol{k}'} = P_{k\theta}. \tag{3.74}$$

This leads to a simplified LBE that admits solution of the form [92],

$$\delta f_m(k,\varphi) = \chi_m(k)\cos\varphi, \tag{3.75}$$

φ being the angle with the $\boldsymbol{X}$ vector [20]. Continuing along this line, we can use the RTA ansatz Eq. 3.64 to define the Momentum RTA (MRTA),

$$\frac{1}{\tau_m^{MRTA}(\boldsymbol{k})} = \frac{V}{(2\pi)^3}\sum_{m'}\int P_{m\boldsymbol{k}\to m'\boldsymbol{k}'}(1-\cos\varphi)\mathrm{d}_3k'. \tag{3.76}$$

Constant RTA

Another simplifying assumption found in the literature is to set τ in Eq. 3.65 constant, and its called for this reason the Constant RTA (CRTA). In CRTA, τ^{CRTA} is effectively regarded as an empirical input parameter; the main consequence is that the details of the carriers scattering are completely lost. Although this approximation may look rather crude, the calculation of S in CRTA in materials, where obtaining P is a challenging task, leads to results in surprisingly good agreement with experiments. This approximation is carefully examined in Silicon in Chap. 6.

[19] This argument can be extended by introducing a tensor relaxation time for ellipsoidal valleys via a Herring and Vogt [93] transformation.

[20] In absence of magnetic field [92].

3.6.2 Variational formula for transport coefficients

As extensively discussed by Ziman [70] the LBE satisfies a variational principle that is useful under many aspects. As a preamble, the inner product between two generic function, $F(\boldsymbol{k})$, $Y(\boldsymbol{k}')$ integrable in the BZ can be defined as, $\langle F|Y\rangle = \int_{BZ} \mathrm{d}_3 k F(\boldsymbol{k}) Y(\boldsymbol{k})$. With this remark, the statement of the variational principle is the following: *among all the functions*, $\tilde{\chi}$, *that satisfy the condition*,

$$\langle \tilde{\chi}|X\rangle = \langle \tilde{\chi}|\mathscr{C}|\tilde{\chi}\rangle\,, \tag{3.77}$$

the solution of the linearised Boltzmann transport equation (3.23), χ *maximizes the quantity*, $\langle \chi|\mathscr{C}|\chi\rangle$. This theorem follows from the observation that $\mathscr{C}$ is positive semi-definite, as shown in Para. 3.3.3.

Thanks to the variational principle, it is possible to calculate the kinetic coefficients avoiding the solution of LBE with the aid of a set of trial functions. Indeed, if a distribution function of the form Eq. 3.30 is inserted in the definition of current density Eq. 3.4, it can be seen that the electric conductivity is proportional to, $\sigma_e \propto \langle \tilde{\chi}|X\rangle = (\langle \tilde{\chi}|X\rangle)^2 / \langle \tilde{\chi}|\mathscr{C}|\tilde{\chi}\rangle$, if $\tilde{\chi}$ belongs to the variational ensemble, which is the set of functions satisfying Eq. 3.77; recalling the definition of χ in terms of Eq. 3.30, the formula for the electric conductivity is as follows,

$$\sigma_e(\tau) = \frac{4e^2 m_e^2}{V\beta} \frac{\left\{\sum_m \int \mathrm{d}_3 k \frac{\partial f^0}{\partial \varepsilon}(\boldsymbol{k}) \left[\boldsymbol{v}_m(\boldsymbol{k})\cdot \boldsymbol{E}/E\right]^2 \tau_m^E(\boldsymbol{k})\right\}^2}{\sum_{mm'} \int \left\{\left[\boldsymbol{v}_m(\boldsymbol{k})\cdot\boldsymbol{E}/E\,\tau(\boldsymbol{k})\right] - \left[\boldsymbol{v}_{m'}(\boldsymbol{k}')\cdot\boldsymbol{E}/E\,\tau_{m'}(\boldsymbol{k}')\right]\right\}^2 \Pi^0_{m\boldsymbol{k}m'\boldsymbol{k}'} \mathrm{d}_3 k \mathrm{d}_3 k'}. \tag{3.78}$$

For every possible approximation of $\tilde{\tau} \propto \tilde{\chi}$ this formula gives a *variational approximation* of electric conductivity, $\tilde{\sigma}_e(\tilde{\tau})$ that is a lower bound of the actual kinetic coefficient, σ_e which is obtained when the exact solution of the LBE, $\tau \propto \chi$, is inserted in the same formula. The true effectiveness of this formula is disclosed upon observing that it applies not only to the relaxation times that satisfy the condition Eq. 3.77, but to every function that is integrable in the Brillouin zone. Indeed, every integrable function, $|Y\rangle$ can be re normalized by a factor $\langle X|Y\rangle / \langle Y|\mathscr{C}|Y\rangle \equiv \alpha$, to fit in the variational ensemble. Then, if it is plugged in Eq. 3.78, the trial function Y appears squared in both the numerator and the denominator so that the factor α cancels out and does not need to be computed explicitly, nor affects the results.

As a side comment pertaining the theory of irreversible thermodynamics (cft. Sec. 3.2), that is presented in more detail by Ziman [70], it is possible to draw a link between the variational principle and a physical principle that is known as the *maximum entropy production principle*. It states: *the exact solution of the LBE maximizes the entropy production*

of the system, as prescribed by the Onsager theory. The proof of this principle is given by noticing that the entropy production of the electronic system due to the action of the fields is equal to $\dot{S}_X = -\langle\chi|X\rangle/T$, while the production due to the scattering events is proportional to $\dot{S}_{\text{scatt}} \propto -\langle\chi|\mathscr{C}|\chi\rangle/T$. Indeed, recalling how the BE was derived from the conservation of the particle density (3.22), it is correct to affirm that both members of Eq. 3.77 are equal to $\int \mathrm{d}_3 k \chi_{\boldsymbol{k}} \dot{f}_{\boldsymbol{k}|_{\text{fields}}}$, and $-\int \mathrm{d}_3 k \chi_{\boldsymbol{k}} \dot{f}_{\boldsymbol{k}|_{\text{scatt}}}$. These expressions are also equal to the total time derivative of the Boltzmann entropy, $S = -k_B \int \mathrm{d}_3 k f(\boldsymbol{k}) \ln f(\boldsymbol{k}) + [1 - f(\boldsymbol{k})] \ln [1 - f(\boldsymbol{k})]$ linearised with respect to χ. The final results reads,

$$\dot{S}_{\text{fields}} = -\frac{1}{T} \boldsymbol{X} \cdot \boldsymbol{J},$$
$$\dot{S}_{\text{scatt}} = \frac{1}{2 k_B T^2} \sum_{mm'} \int \mathrm{d}_3 k \mathrm{d}_3 k' \left[\chi_m(\boldsymbol{k}) - \chi_{m'}(\boldsymbol{k}')\right]^2 \Pi^0_{m\boldsymbol{k}m'\boldsymbol{k}'}.$$

At the steady state, the total entropy density in the sample is constant because these two entropy sources are equal in magnitude and opposite in sign. In a transient situation, on the l.h.s. of the BE the explicit temporal dependence of the distribution function appears: this new term accounts for an implication of the *Boltzmann H theorem* which can be formulated as: *in a system undergoing an irreversible thermodynamical transformations there is an increase in the system entropy*.

Chapter 4

HPC methods for the exact LBE solution

In this chapter, I discuss briefly the novel HPC software infrastructure that I implemented from scratch to solve exactly the LBE with accurate, first-principles EPC. In Sec. 4.1, I give an overview of the code. In Sec. 4.2, I describe how a multi-sampling scheme of the BZ can be exploited to efficiently calculate EPC and $\mathscr{C}$ with the aim of enhancing the feasibility of these demanding transport calculations. In Sec. 4.3, it is discussed how the implementation of a cartesian topology of the processes is beneficial to the computational management of matrices: they can be efficiently distributed among processes to obtain a neat speed-up both in the calculation of the matrix elements and in the linear algebra operations needed to the solution of the LBE, and to increase the efficiency in memory allocation, which represent a hard limit in the resources available to any numerical calculation. In the last section, Sec. 4.4, the theory and application of the preconditioned Conjugate Gradient algorithm that solves the LBE are described.

4.1 `eBET`: exact Boltzmann Electronic Transport

Numerical methods for the solution of the BE have been developed in many sectors of physics and engineering for a multitude of tasks [94–96]. The numerical results in this work have been obtained with a novel implementation of an LBE solver that efficiently exploits Wannier interpolation to calculate the electronic and vibrational properties, and the electron-phonon scattering from first-principles in realistic systems. This allows to solve the LBE on meshes with extremely high k-point densities (see App. C), even when compared to the most recent works on the same systems [28, 27], which will be discussed later in the result chapter, Chap. 6, .

The name of the code is `eBET`: exact Boltzmann Electronic Transport. Its functional structure is summarised in Fig. 4.1. This implementation is also easily adaptable to incorporate analytical models of electronic transition probability (see App. B) to find fitting parameters from first-principles or in case a first-principles treatment is not straightforward (see Sec. 3.4.3).

Given the numerical complexity of electronic transport calculations, special attention has been posed to performance enhancement. It has been implemented according to the `fortran2003` standard and parallelized with MPI communication[97] for distributed CPU computing. Basic symmetries have been exploited, such as the symmetry of the squared EPC function under exchange of electronic states (see Eq. 2.33). One of the features that allow the best performance enhancement is the fundamental integration of the LBE solver with Wannier interpolation. As argued in Sec. 2.5, MLWF are a convenient and accurate tight-binding basis set for all the quantities needed to solve the LBE. This is especially convenient for the EPC, which is the most computational burdening quantity in this first-principles approach.

ε, $\hbar\omega_\lambda$ and g are efficiently computed on arbitrary k-point meshes through Wannier interpolation (cft. Sec. 2.5), after the Wannier representation of $\mathscr{H}$, $\mathscr{D}$ and $\langle \quad |\partial V| \quad \rangle$ is provided as an input to eBET. This pre-processing procedure to obtain ε, $\hbar\omega_\lambda$ and g in Wannier representation is accomplished by the `wannier90` [65] and `EPW` [67] software packages which in turn work on top of a plane-wave DFT calculation that is carried out with `QUANTUM ESPRESSO` [58]. Making the Wannier interpolation work together with the LBE solver allows greater flexibility in the BZ sampling, leading to an improved accuracy in the calculation of the $\mathscr{C}$ elements, and a more accurate convergence of the transport quantities.

4.2 Multi-mesh interpolation for electronic transport

In `eBET` it is possible to store EPC matrix elements, $\left\langle m'\boldsymbol{k}+\boldsymbol{q}\left|\partial^\lambda_{\boldsymbol{q}}V\right|m\boldsymbol{k}\right\rangle$ on a $\mathbf{k}$-points grid that is less dense than the one used for transport i.e. solve the LBE and calculate the kinetic coefficients. Firstly EPC matrix elements are stored on ($N_{\mathrm{EPC}}\times N_{\mathrm{EPC}}\times N_{\mathrm{EPC}}$) mesh, and then a denser grid ($N_f\times N_f\times N_f$, with $N_f = p\cdot N_{\mathrm{EPC}}$ and $p\in\mathbb{N}$) is used to compute $\mathscr{C}$, solve the LBE, and compute the transport quantities.

This technique has been conceived to address an important issue related to the primitive cell sampling: transport quantities requires very dense $\mathbf{k}$-point grids around μ to converge[98, 66], while on the other hand, direct calculations suggest that the EPC is a rather smooth function in reciprocal space and it is well described with $\mathbf{k}$-points samplings of 30^3 to 40^3 in metals, and 50^3 to 70^3 in Silicon and Diamond. Upon closer inspection, it is possible

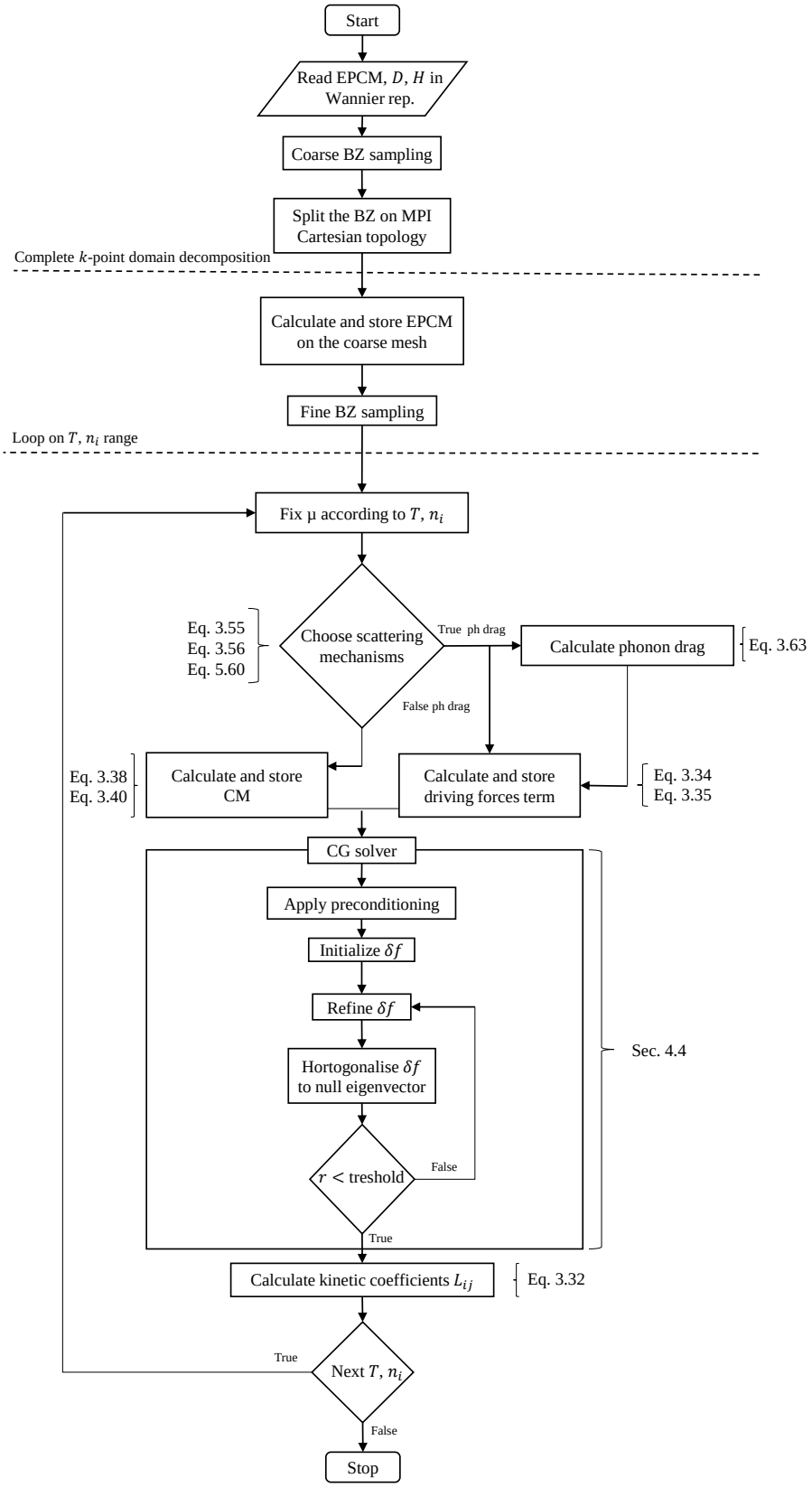

Fig. 4.1 Flow chart of the eBET software infrastructure which has been used to obtain all the results in this work. The Eq. numbers in the picture refer to the formulae that have been implemented to carry out the numerical calculations.

to observe that the energy derivative of the Fermi function has a more oscillatory behavior compared to the coupling function, g^{λ}: $\partial f_0/\partial\varepsilon$ is a gaussian-like function localised around the chemical potential, μ [1]. The same is true for the Dirac deltas ensuring energy conservation, approximated with normalised Gaussians, that are multiplied with the Fermi function energy derivatives in the matrix elements of $\mathscr{C}$ (see Eq. 3.40). Practically, this means that a very fine BZ discretization is required to accurately sample Π^0, rather than g^{λ}. A similar argument can be put forward for the integrand of the kinetic coefficients (cft. Eq. 3.32) in which the factor $\partial f^0/\partial\varepsilon$ explicitly appears.

To reconcile the two grids, the EPC in those fine-grid points that are not equivalent to the coarse ones is assumed to be equal to the closest coarse point, and this is the same as assuming that the EPC is constant within the sub-unit cell that encases each coarse mesh point[2]. Thanks to the efficiency of WF interpolation, all the other quantities of interests, $\hbar\omega_{\lambda}$ and ε_m needed to calculate $\mathscr{C}$ can be quickly computed on the fine mesh, leading to a very accurate sampling of Π^0 in the Primitive Cell (PC) of the lattice.

4.3 The MPI cartesian topology

The parallel MPI implementation was achieved mainly through domain decomposition e.g. splitting the PC and all the physical quantities defined within, in non-overlapping pieces, and assigning each one of the pieces to one of the processes. One of the aspects of the parallelisation that allows for the best performance enhancing results is that the processes have been arranged in 2-dimensional MPI *cartesian topology*. In the *open MPI* library [97] this is implemented invoking the command `MPI_CART_CREATE`. This is very convenient while dealing with quantities that are function of pairs of $\boldsymbol{k}$-points and are computationally demanding in terms of both time and memory requirements (see discussion about EPC in Sec. 4.2). By employing the cartesian topology, three milestones in performance enhancement are achieved: firstly a cut of run time proportional to the number of processes, n_{proc}, secondly a cut of the memory requirements of a factor equal to the number of computer nodes, and thirdly, a neat path to implement symmetry reductions and the double-mesh scheme of Sec. 4.2. The details and consequences of these three points are discussed below.

[1] Electronic states relevant to transport of converged calculations were selected within an energy window around μ of at most ± 0.25eV in semiconductors and ± 0.1eV in metals.

[2] See Fig. C.1 for the analysis of the convergence of the silicon electron mobility w.r.t. the two grids.

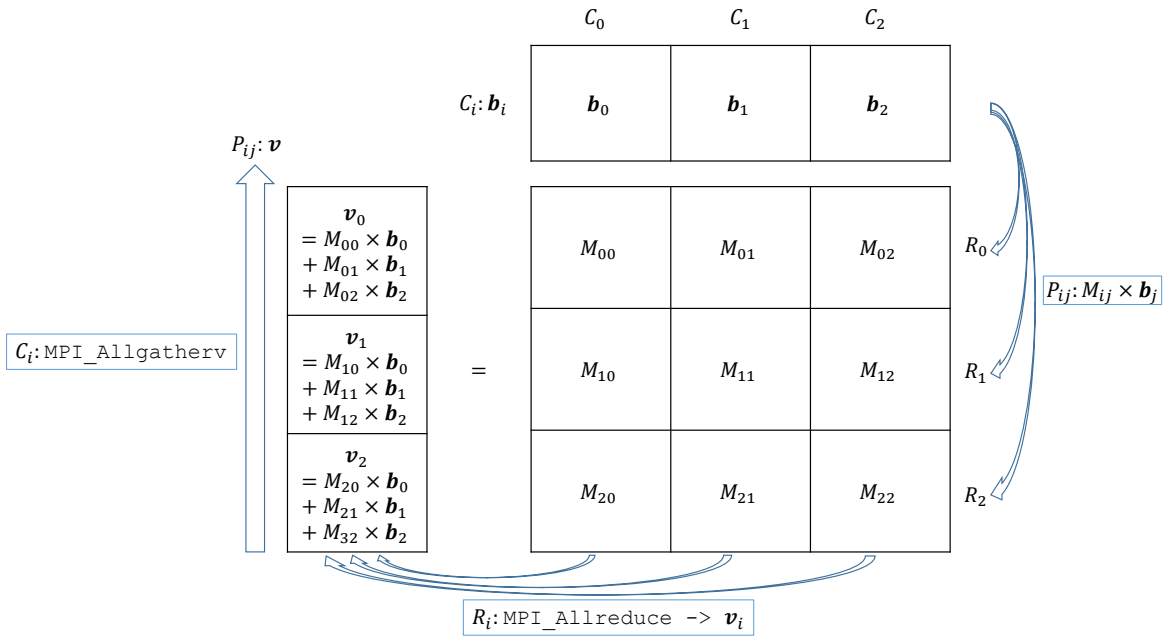

Fig. 4.2 Distributed matrix $\times$ vector operation ($M \times \boldsymbol{b}$) on the MPI cartesian topology of 9 processes (clockwise from top right corner). The process P_{ij}, is ranked according to a cartesian coordinate system: i, j indicate the coordinates so that, in this example $i, j \in 1, 2, 3$. The BZ has been split in 3 non-overlapping, complete pieces. Each one of the nine processes possesses a tile of the matrix, M_{ij}, and each column of processes, C_j, shares the corresponding portion of the vector $\boldsymbol{b}$, b_j. The $M_{ij} \times \boldsymbol{b}_j$ product is performed by each process with its local information: P_{ij} has been provided with the pieces i and j of the BZ and all the quantities defined therein. Each segment of the resulting vector $\boldsymbol{v}$, $\boldsymbol{v}_i$, is then computed with the collective `MPI_Allreduce` sum among each row of processes, R_i. As the last operation, each column of processes performs the `MPI_Allgatherv` operation so that each process P_{ij} has a local, identical copy of the complete vector $\boldsymbol{v}$.

The cartesian topology allows for matrices defined on $\boldsymbol{k}$-points to be *tiled* in square or rectangular sub-matrices [3]. For both EPCM and $\mathscr{C}$, this means that the loading time can be cut by a factor equal to n_{proc} and, most importantly, the memory requirements reduced by a factor equal to the number of computer nodes that compose the cluster. It is also quite easy to design an implementation that can exploit the fact that both EPCM and $\mathscr{C}$ are symmetric: it is sufficient for each process to just store its lower triangular part. This cuts memory and time requirements by another factor 2. Another great feature of the cartesian topology implementation is that all the linear algebra operations needed by CG e.g. the matrix-vector or scalar products can be easily performed locally by each process, achieving again a speedup of a factor n_{proc}. To then collect the complete result, just a standard `MPI_ALLREDUCE` call is performed among one or both of the cartesian directions, depending on if the global operation is a matrix-vector or a scalar product. An illustration of this operation is depicted in Fig. 4.2, in which both memory and computation time improvements can be appreciated.

Thanks to the cartesian topology arrangement, each process does not need to have access to all the BZ to perform local operations, but just to a fraction of its which is at most comprised of an number equal to $\sqrt{n_{\text{proc}}}$ of $\boldsymbol{k}$-points, for matrix quantities, leading to a great reduction in the redundancy of information stored in memory by each node. For quantities that depend on one variable ranging across the BZ such as the kinetic coefficients (see Eq. 3.32), the calculation can still be efficiently parallelised along one of the two dimensions of the cartesian topology (rows or columns). This is not the case of implementations where the matrices are divided in *stripes*, meaning that the sub-matrix stored by each process has one side equal to n_{kp} *div* n_{proc} or n_{kp} *div* $n_{\text{proc}} + 1$ and the other equal to n_{kp}, but still needs access to all the BZ. Also, linear algebra operations' speed-up is just linear in n_{proc}, rather than quadratic, in this "stripe" configuration of the processes, since matrix-vector and scalar products have to be performed by each process over all the BZ.

As an additional, non-secondary benefit, this novel implementation allows the scaling of the performance with the number of processes to remains consistent while employing thousands of CPU cores; this has proven to be particularly effective for HPC computer infrastructures such as national and international tier-0 and tier-1 HPC facilities. As an example, the code has been successfully executed on the ARCHER UK HPC facility employing up to 2304 processes.

[3] If the number of points in the BZ in not a multiple of the square root of the number of processes, $\sqrt{n_{\text{proc}}}$ they can be easily re-arranged among the processes so that the points per side of each tile is always equal to n_{kp} *div* $\sqrt{n_{\text{proc}}}$ or n_{kp} *div* $\sqrt{n_{\text{proc}}} + 1$, where *div* stands for *integer division*.

4.4 Preconditioned Conjugate Gradients solver

The task of solving the LBE (Eq. 3.46) once $\mathscr{C}$ (Eq. 3.40) has been calculated is accomplished using a preconditioned Conjugate Gradient algorithm (CG). The CG has already found application in fields such as electronic structure [99] and thermal transport [76]. The main mathematical features of this techniques will now be outlined along the lines of Ref. 100. As a preamble it is important to notice that each solution $\boldsymbol{x}$ to a linear system in which the matrix, M, is *symmetric* and *positive definite*,

$$\boldsymbol{b} - M\boldsymbol{x} = 0, \tag{4.1}$$

is linked to the quadratic form,

$$f(\boldsymbol{x}) \equiv \frac{\boldsymbol{x}^T M \boldsymbol{x}}{2} - \boldsymbol{b}^T \boldsymbol{x} + c. \tag{4.2}$$

Indeed, the gradient of f, ∇f, is

$$\nabla f(\boldsymbol{x}) = \boldsymbol{b} - M\boldsymbol{x}, \tag{4.3}$$

which is equal to the left-hand side of Eq. 4.1. Following from the properties of M, f is *convex*. This means that the solution to Eq. 4.1, $\boldsymbol{x}$, corresponds to f's global minimum.

As many other iterative methods (MINRES [101]), given a trial point $\boldsymbol{x}_0$, CG refines its *residual*, $\boldsymbol{r}_0 \equiv M\boldsymbol{x}_0 - \boldsymbol{b}$ iteration after iteration monotonically. This procedure converges when the residue's euclidean norm is zero, $\|\boldsymbol{r}_{n-1}\|_2 = 0$, and in the case of CG, this is guaranteed to happen exactly after n steps [101], if the problem is set in $\mathbb{R}^n$. What makes CG special is that the searching directions, $\boldsymbol{d}_m$, along which $\boldsymbol{r}_m$ is minimised at each step, are chosen to be M-orthogonal, or *conjugate* with respect to M, meaning that,

$$\boldsymbol{d}_m M \boldsymbol{d}_{m'} = 0, \qquad \forall m' \neq m \in \{0, \ldots, n-1\}. \tag{4.4}$$

The vectors $\{\boldsymbol{d}_m\}$ are chosen to be the directions of the search because this guarantees what can be referred to as the *optimality* of the error, $\boldsymbol{e}_m \equiv \boldsymbol{x}_i - \boldsymbol{x}$ has the smallest M-norm $\|\boldsymbol{e}_m\|_M \equiv \boldsymbol{e}_m M \boldsymbol{e}_m$ in the subspace spanned by $\{\boldsymbol{d}_0, \ldots, \boldsymbol{d}_m\}$.

To calculate $\{\boldsymbol{d}_m\}$ it is standard practice to start from the residuals $\{\boldsymbol{r}_m\}$ and then make them conjugate with respect to M. The intuition behind this choice comes from Eq. 4.3, according to which $\boldsymbol{r}_m = -\nabla f$. At each step, m, we move along the segment $\boldsymbol{d}_m$ of an amount

α_m so that we minimize f. With the staring point,

$$\boldsymbol{d}_0 = \boldsymbol{r}_0 = \boldsymbol{b} - M\boldsymbol{x}_0, \tag{4.5}$$

we are able to compute each $\boldsymbol{x}_m$ through the following set of equations,

$$\alpha_m = \frac{\boldsymbol{r}_m^T \boldsymbol{r}_m}{\boldsymbol{d}_m^T M \boldsymbol{d}_m}, \tag{4.6a}$$

$$\boldsymbol{x}_{m+1} = \boldsymbol{x}_m + \alpha_m \boldsymbol{d}_m, \tag{4.6b}$$

$$\boldsymbol{r}_{m+1} = \boldsymbol{r}_m - \alpha_m M \boldsymbol{d}_m, \tag{4.6c}$$

$$\beta_m = \frac{\boldsymbol{r}_{m+1}^T \boldsymbol{r}_{m+1}}{\boldsymbol{r}_m^T M \boldsymbol{r}_m}, \tag{4.6d}$$

$$\boldsymbol{d}_{m+1} = \boldsymbol{r}_{m+1} - \beta_{m+1} \boldsymbol{d}_m. \tag{4.6e}$$

Eq. 4.6, together with the initialization condition, Eq. 4.5, completely describe the non-preconditioned version of the CG at each iteration.

4.4.1 Preconditioning

The preconditioning subject is indeed a vast one[101] and it is not only linked to the solution of linear systems. To the extent of the subject discussed here, the convergence of CG can be significantly improved by trying to reduce the *condition number* of the matrix, M, by *preconditioning* the linear system defined by M and $\boldsymbol{b}$. The condition number, $\mathbb{k}$, is defined in the euclidean norm $\|\cdot\|_2$ and if M is a *normal matrix*, as the ratio of the largest eigenvalue, λ_{max}, over the smallest one, λ_{min},

$$\mathbb{k}(M) \equiv \frac{|\lambda_{\max}(M)|}{|\lambda_{\min}(M)|}, \tag{4.7}$$

$$\mathbb{k} \geq 1, \tag{4.8}$$

and it has a lower bound of one. Loosely speaking, $\mathbb{k}$ provides a measure of how a generic vector $\boldsymbol{v}$ is changed after successive application of M –think about $\boldsymbol{v}$ as linear combination of the M's eigenvectors. This is a particularly important aspect in the case of *Krylov space* techniques such as CG. These techniques approximate the solution to Eq. 4.1 at each step, $\boldsymbol{x}_m$, as linear combination of vectors obtained from the repeated application of M to an initial vector, span$\{\boldsymbol{r}_0 \mathrm{M}^{\mathrm{m}-1}, \boldsymbol{r}_0 \mathrm{M}^{\mathrm{m}-2}, \ldots, \boldsymbol{r}_0\}$, as in the case of CG. Another intuitive argument is the following: the easiest linear system to solve is the one with $M = \mathbb{1}$. It is immediate to

observe that $\mathbb{k}(\mathbb{1}) = 1$, so that we could informally say that the closer the condition number is to unity, the more similar M is to the identity in this context. If $M = \mathbb{1}$, the iso-surfaces of Eq. 4.2 are hyper-spheres, while for a general matrix which is still symmetric and positive definite they will be hyper-ellipsoids. The larger the condition number is, the more dishomogeneous the eigenvalues of M are: this means that the hyper-ellipsoid will have very different axis, requiring more frequent changes of directions to get to the bottom of the valley, if the starting direction is not chosen carefully. For the CG purposes, this means that $\boldsymbol{x}_m$ converges faster, in a finite precision sense, to the solution $\boldsymbol{x}$ if the condition number is closer to one.

The goal of preconditioning is to map Eq. 4.1 to a system with an improved condition number. This is achieved transforming M by a preconditioning matrix, L, so that the improved linear system will be defined as,

$$L^{-1}ML^{-T}\boldsymbol{y} = L^{-1}\boldsymbol{b}, \tag{4.9}$$

$$\boldsymbol{y} \equiv L^{T}\boldsymbol{x}. \tag{4.10}$$

The preconditioning that is implemented in `eBET` to solve the LBE defined by $\mathscr{C}$ is known as *diagonal preconditioning* [100], in which case L^{-1} is defined as,

$$L^{-1} = \frac{1}{\sqrt{\text{diag}(\mathscr{C})}}. \tag{4.11}$$

Referring to definition of $\mathscr{C}$, Eq. 3.40, it is possible to see that the largest element of each row/column is the diagonal one, that is made of the of the sum of all the off diagonal ones. In `eBET` the CG is used to solve the equivalent of Eq. 4.9 and then physical solution is recovered using Eq. 4.10.

4.4.2 Comparison with Steepest Descent

A comparison with the more simple and intuitive Steepest Descent (SD) algorithm helps clarifying the advantages of proceeding along the conjugate directions, $\{\boldsymbol{d}_m\}$ to minimise the quadratic form Eq. 4.2. SD just proceeds along the reversed direction in which the gradient of F, ∇f, is pointing locally (steepest descent) and set the length of step to get to the local minima along this direction. This is formalised in the following recursive algorithm, that

defines SD,

$$\boldsymbol{r}_m = \boldsymbol{b} - M\boldsymbol{x}_m, \tag{4.12a}$$

$$\alpha_m = \frac{\boldsymbol{r}_m^T \boldsymbol{r}_m}{\boldsymbol{r}_m^T M \boldsymbol{r}_m}, \tag{4.12b}$$

$$\boldsymbol{x}_{m+1} = \boldsymbol{x} + \alpha_m \boldsymbol{r}_m \tag{4.12c}$$

We can see that the bit that is added to obtain $\boldsymbol{x}_{m+1}$ in Eq. 4.12c is pointing in the local steepest direction because, by definition, the residual, $\boldsymbol{r}_m$ is equal to Eq. 4.3. α_m is chosen to nullify the directional derivative along $\boldsymbol{r}_m$, $\mathscr{D}_{\boldsymbol{r}_m}$. This can be seen by this identity,

$$\mathscr{D}_{\boldsymbol{r}_m} f(\boldsymbol{x}_{m+1}) = \nabla f(\boldsymbol{x}_m)^T \boldsymbol{r}_m = -\boldsymbol{r}_{m+1}^T \boldsymbol{r}_m \tag{4.13}$$

which then is combined with Eq. 4.12a and Eq. 4.12c to get rid of $\boldsymbol{x}_{m+1}$. Finally, the minimum point is found along $\boldsymbol{r}_m$ by solving,

$$\left[\boldsymbol{b} - M(\boldsymbol{x}_m + \alpha_m \boldsymbol{r}_m)\right]^T \boldsymbol{r}_m = 0, \tag{4.14}$$

which leads to Eq. 4.12b.

This method as two drawbacks that have the same origin. First, it is highly dependent on the initial starting point, if the condition number is not sufficiently close to one. Secondly, each step could have components in the reverse direction of some, if not all, of the previous one, which represents a major catastrophe. The root of these nuisances is that the directions along which the step are taken are not independent from the previous ones [99]. The fact that the CG exploration directions, $\{\boldsymbol{d}_m\}$ are conjugate, means that at each new step, we will be exploring the subspace, span$\{\boldsymbol{d}_{m+1}\} \supseteq$ span$\{\boldsymbol{d}_m\}$ so that the M-norm of the error, $\|e_{m+1}\|_M$ will be at its global minimum,

$$\|e_{m+1}\|_M \leq \|e_m\|_M, \tag{4.15}$$

which is a thing that it is not strictly guaranteed by SD. This means that, no matter how narrow is the valley, if the space is two-dimensional, CG will converge in two steps. On the contrary, SD will converge in one iteration if the staring point, $\boldsymbol{x}_0$ is chosen along one of the valley's axis, or might take countless iterations if bad luck picks $\boldsymbol{x}_0$ to be close to the axes' diagonal, as can be seen from Fig. 4.3b.

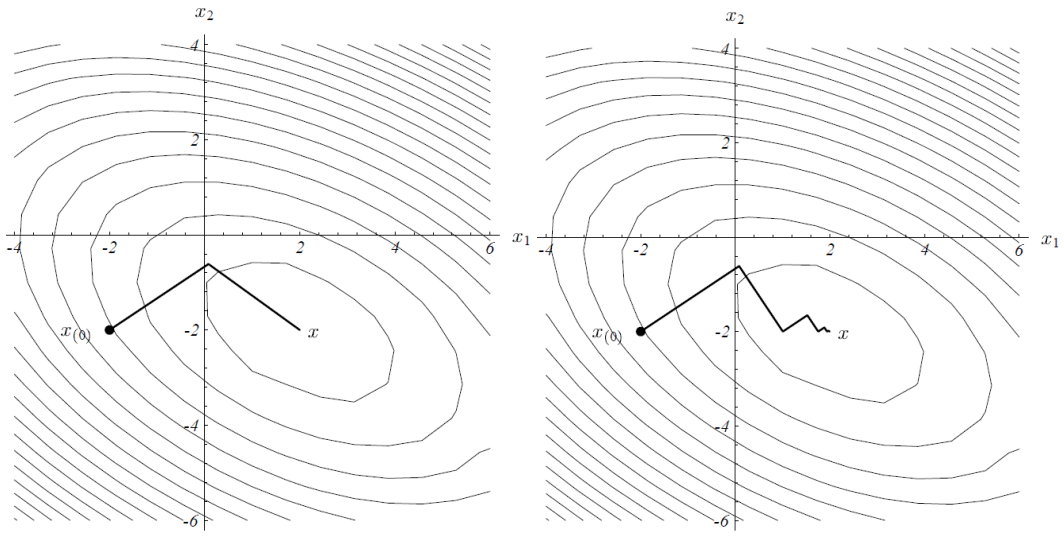

(a) CG path to minimum. (b) SD path to minimum.

Fig. 4.3 Comparison of convergence between CG and SD. In 2 dimensions, CG converges exactly after 2 steps. SD convergence is highly dependent on the initial point: the choice in picture (4.3b) isn a particularly poor one for this method.

4.4.3 Implementation and convergence

All the facts outlined in Sec. 4.4, especially the convergence bounds of CG, are true in an exact arithmetic context [101]. Despite this, executing the algorithm on a finite precision machine has more advantages than drawbacks. The most important theoretical drawback is that we lose the strict convergence bound, n steps in $\mathbb{R}^n$. This is not an issue at all since the preconditioned CG usually converges, in a finite precision sense, in few tens of iterations.

As shown in Subsec. 3.3.3, the collision matrix is semi-positive definite. This could lead to catastrophic consequences, e.g. the CG would not be appropriate, mainly because of possible singularities in the calculation of α (Eq. 4.6a) and β (Eq. 4.6d). Nevertheless, I numerically verified that the smallest eigenvalue of $\mathscr{C}$ (Eq. 3.40) is not zero, but just smaller than the others by few orders of magnitude. As already mentioned in Sec. 3.3.3, the null eigenvalue, $\boldsymbol{u}_{null}$ (Eq. 3.50) has all its components equal to 1. The component of the BE solution along $\boldsymbol{u}_{null}$ has no physical meaning since completely filled bands do not contribute to transport[36]. This means that to enhance the stability of the CG implementation, we can remove from each one of the relevant vectors in Eq. 4.6 their component along $\boldsymbol{u}_{null}$, avoiding possible singular values when computing the denominators of α and β.

Chapter 5

Elemental metals: framework validation

The validity of the first-principles transport framework described in the previous chapters is demonstrated by predicting electronic transport properties in bulk metals. Although the subject as been studied for many years, it is still a topic of great interest as demonstrated by recent works. As an example, it is possible to mention the work by Lanzillo et al. [102] on the effect of pressure on the electrical resistivity of metals or the work of Xu and Verstraete [103] on the anomalous Seebeck coefficient in alkali metals.

Simple metals are a good example of materials to test the effectiveness of the first-principles treatment of the EPC described in Chap. 2: well studied phenomena such as electrical and thermal conductivity, thermal expansion, renormalization of the electronic specific heat, superconductivity, *et cetera*, are direct manifestation of the interaction between electrons and phonons. In particular, the Eliashberg-Migdal theory (EM) [104] had been developed to treat EPC in superconductivity, and was later extended by Allen [105] and applied to more general electronic transport phenomena [103, 106, 107].

This chapter focuses on the electrical and thermal resistivity of electrons in Aluminium (Al) and Copper (Cu). In particular, Aluminium is considered a prototype system for the quasi-particle phenomenology of metals [106]. Bauer et al. [106] and Savrasov and Savrasov [107] studied the electronic transport of Al and Cu, respectively calculating ε, $\hbar\omega_\lambda$ and EPC from DFT in LDA. Specifically, EPC was calculated as a linear response of the electron density to ion displacements as outlined in Sec. 2.3 [1]. The first-principles treatment of Ref. 106 and Ref. 107 is similar of the one presented in this work, although the accuracy in terms of mesh size is vastly increased here thanks to Wannier interpolation (see Sec. 2.5) and the HPC software infrastructure that implements it (see Chap. 4). The transport theory used in

[1] The implementation of DFT in Ref. 106 used PW basis as in this work, whereas Ref. 107 employed the linear muffin-tin method.

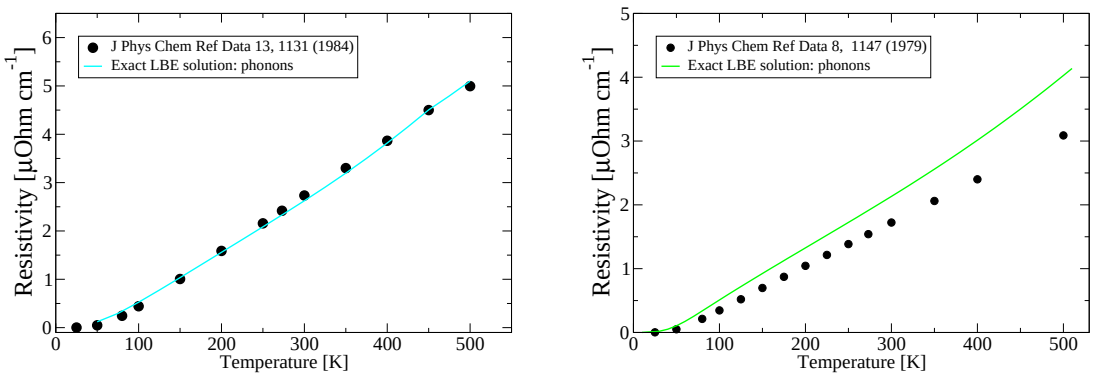

Fig. 5.1 Al (left panel) and Cu (right panel) electrical resistivity as function of temperature. Solid lines are the exact solution of the LBE. Circles are the experimental results (Ref. 108 for Al and Ref. 109 for Cu)

Ref. 106 and Ref. 107 to calculate conductivities is the one mentioned at the beginning of this chapter Allen [105], known as the Lowest Order Variational Approximation (LOVA) to BE, and provides a further element of comparison for the more general transport approach described in Chap. 3.

5.1 Electric resistivity

In pure metals, electric resistivity is only due to EPC. Our calculation of $\rho_e(T)$ in Al is shown in Fig. 5.1 left (solid cyan line): the agreement with experimental results (symbols) is excellent and confirm earlier successes [106, 107] in the first principles description of EPC in a DFPT LDA picture for this system as depicted in Fig. 5.1. The prediction of $\rho_e(T)$ in Cu is shown in Fig. 5.1 right (solid green line): the agreement with experiments (symbols) is reasonable, but the results slightly overestimate the experimental ones.

It is interesting to note that our predicted values are consistent with the ones computed by Savrasov and Savrasov [107] using the LOVA, and band structure and EPC from LDA (see Fig. 5.2). The agreement between the two approaches rules out the possibility that the discrepancy between theory and experiment is a result of the variational approach to transport in the LOVA employed in Ref. 107, that provides an upper bound to the observed resistivity. Such discrepancies could be instead related to the inaccurate description of the system in LDA. In order to asses this conjecture, further studies are required, possibly including GW corrections to the DFT parameters.

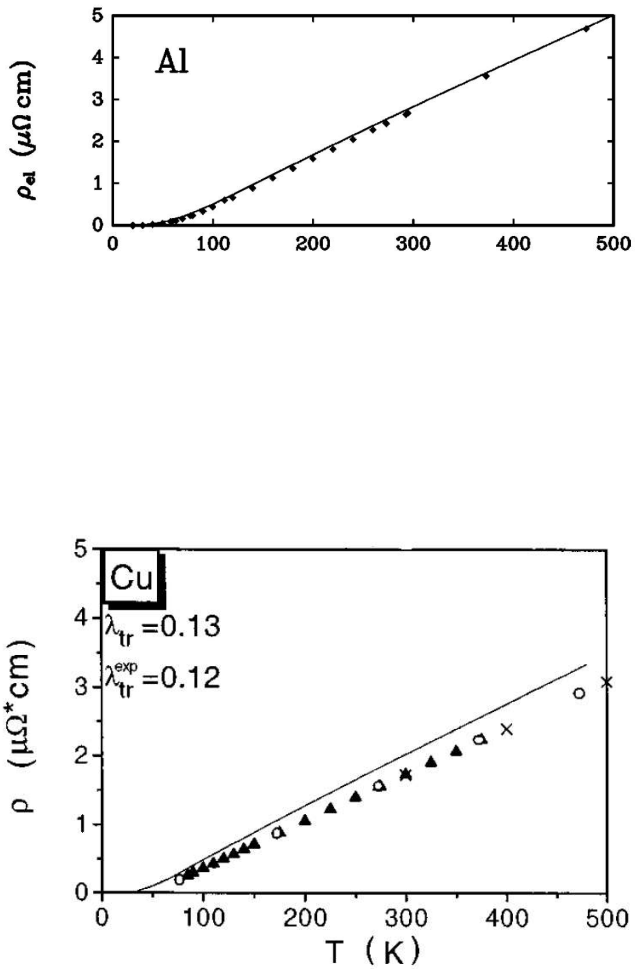

Fig. 5.2 Electrical resistivity (solid lines) calculated by Bauer et al. [106] in Al (upper panel) and by Savrasov and Savrasov [107] in Cu (lower panel). Both calculations used DFT in LDA, treated EPC as in the EM [104] and calculated ρ_e in the LOVA [105] of BT. Ref. 106 carried out DFT calculation using a PW basis while Ref. 107 used a linear muffin-tin orbital basis. Figures are adapted from Ref. 106 and Ref. 107.

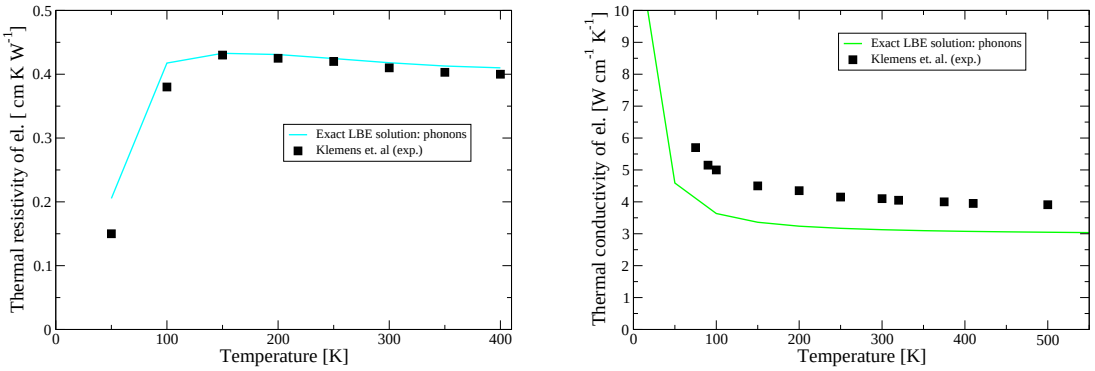

Fig. 5.3 Al thermal resistivity (left panel) and Cu thermal conductivity (right panel). Solid lines are the exact solutions of the LBE. The squares are the experimental results from Ref. 110.

5.2 Thermal transport by electrons

The thermal conductivity and resistivity, k_e and $1/k_e$ in Al and Cu are presented in Fig. 5.3. Also in this case, the calculations in this work agree with the ones of Ref. 106 and Ref. 107 (cft. Fig. 5.4) where the same DFT LDA first-principles approach was used together with the LOVA. Comparing the theoretical prediction with experiments (symbols), good agreement is found in both cases. It is important to notice however that also in this case Copper exhibits some discrepancy with experiments. As for electric resistivity this could be due to shortcomings of LDA, or also it could be due to a larger lattice contribution to thermal conductivity, especially at low temperatures. It is not straightforward to extract phonons' contributions to thermal conductivity from experimental data, although it would be certainly possible to estimate this quantity by solving the phonons' BE which is beyond the scope of this work. As a last remark, it is interesting to note that Al shows excellent agreement, as this system is often regarded as a paradigm of transport from electronic quasi-particles.

5.3 Wiedmann-Franz law from first-principles

Franz and Wiedemann [113] proposed a simple relation between thermal conductivity of electrons and electric conductivity in metals (cft. Eq. 3.19),

$$\frac{k_e}{\sigma_e} = LT, \tag{5.1}$$

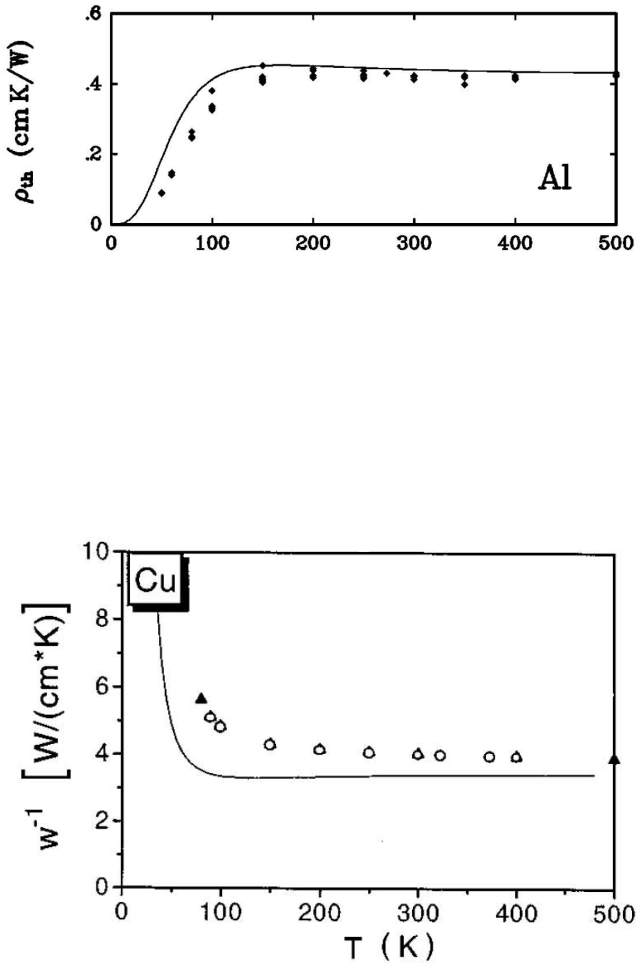

Fig. 5.4 Thermal resistivity of electrons from Bauer et al. [106] in Al (upper panel) and thermal conductivity of electrons from Savrasov and Savrasov [107] in Cu (lower panel) in the intrinsic regime. The details of the theoretical framework are the same of Fig. 5.2.

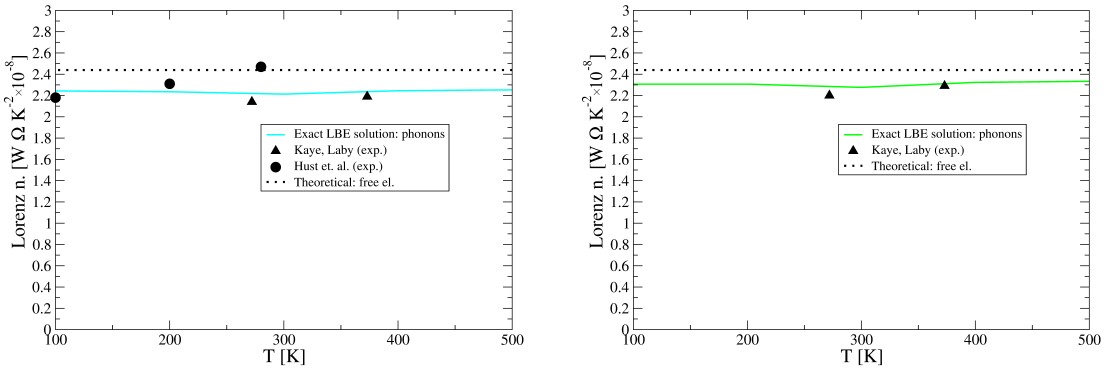

Fig. 5.5 Comparison of the Lorenz number (solid lines) as function of temperature for Al (left panel) and Cu (right panel) as calculated in this work. The symbols are experimental data from Hust et al. [111] and Kaye and Laby [112].

that defines the Lorenz number, L as discussed in Sec. 3.2. As stated in the original work in Ref. 113 and supported by modern observation [112], in simple metals L is close with good approximation to the theoretical value of [36],

$$L = 2.44 \times 10^{-8} \mathrm{W\Omega K^{-2}}, \tag{5.2}$$

as predicted for the free-electron gas [2].

In Fig. 5.5 the temperature dependence of L is shown in Al (left panel) and Cu (right panel): these first-principles calculations (solid lines) confirm the statement of the Wiedemann-Franz law, and are in agreement with experimental observations [112, 111]. Nevertheless, it is important to note that in the case of Copper, this agreement is due to error cancellation between thermal conductivity and electrical conductivity, that are both underestimated in these first-principles predictions.

5.4 Conclusion

Calculation in Al and Cu confirm the validity of the transport framework presented in Chap. 2 and Chap. 3 both against previous seminal works[106, 107] and experimental findings [108–110]. Al is a paradigm of transport by non-interacting quasi-particles in simple metals

[2] This value can be deduced within the simple context of the Sommerfeld theory of metals [36].

and the excellent overall agreement of the DFT in LDA description with experiments is confirmed.

The case of Cu is more interesting. This work establishes for the first time that the discrepancies between theory and experiment reported in earlier works are not a consequence of the variational approximation to the BE (LOVA). This preliminary test of this novel computational framework already highlights that the field of ab-initio electronic transport still presents important open questions, even in relatively simple systems such as bulk Copper.

Chapter 6

Silicon: first-principles thermoelectricity with non-equilibrium phonon effects

Silicon (Si) is the most successful functional material with ubiquitous technological applications ranging from microelectronics to energy harvesting and conversion[114]. With the rise of nanotechnology, thermoelectric material engineering[115, 116] has regained interest thus leading to a renewed scientific attention on the fundamental aspects of thermoelectricity. In this section, I present a first-principles prediction of electronic transport properties of Si with a focus on its thermoelectric applications[1].

Silicon represents an excellent test case to validate my approach since its electronic transport properties have been extensively studied in the past. In particular, there are several works focusing on the prediction of transport coefficients using different levels of approximation: one of the outstanding challenges is to find suitable approaches for the best trade-off between the accurate solution of the of the transport theory e.g. the BE, and a reliable description of the physical system. Restrepo et al. [77], Zhou et al. [27] employed a first-principles picture of the fundamental physics but avoided the BE, calculating the steady-state electron population in RTA. Wang et al. [117] used semi-empirical models of scattering while solving the LBE in its ε-dependence only. Li [28] combined the two approaches but focused on the intrinsic transport regime, which is of limited applicative interest. In addition, the role of the coupled electron-phonon dynamics on thermoelectricity has very recently received a renewed interest as a path to enhance thermoelectric efficiency at room-to-low temperatures[27]. It is well known indeed that in covalent-bonding semiconductors[75] such as Silicon[88], Germanium[87], Diamond[89] there is a conspicuous enhancement, even at room temperature of S caused by phonon drag.

[1] The results of this chapter were published in Ref. 90

With the novel computational implementation (see. Chap. 4) of BT, this work is able to achieve a greater level of accuracy on both the solution of the transport theory and the first-principles description of the physical system. In this chapter, the thermoelectric properties of Si electronic system in a wide range of donor concentration and temperature are predicted.

This work aims to quantify how phonons and donors influence electronic transport and thermoelectric coefficients. Particular care is taken to accurately describe the effect of the coupling between electron and phonons and the consequences of a temperature gradient driving phonons out of equilibrium. Another purpose is to clarify why rather crude approximations such as CRTA give correct answers for some thermoelectric quantities and whether or not the solution of the LBE is essential to reproduce the experimental findings [2]; the main issue with these approximations it that, in spite of their effectiveness, they make any *ab initio* approach less transparent, hindering a first-principles understanding of the predicted phenomena. As a last interesting highlight, I comment on the accuracy of DFT in the electron-phonon interaction calculation and how this affects transport coefficients.

6.1 System simulation from first principles

The advantages of investigating n-doped Silicon are that the conduction band is easily calculated within LDA DFT [3].

The scattering events of interests in Si are due to phonons and ionised impurities. Arsenic and Phosphorus are commonly utilised as donor impurities and in the range of temperatures investigated are completely ionised. Also, given the efficient implantation techniques, compensation between donor and acceptor impurities plays no role in highly pure samples[4]. For these reasons, neutral impurity scattering is not relevant in this system. EPC has a central role both in its diffusive and phonon drag effects.

No compensation has been assumed so that the donor density is equal to charge density in the conduction band. The effect of the donors on the electronic structure has been modelled with a Fermi level shift, to match the extrinsic carrier concentration in the conduction bands.

[2] See Sec. 3.6.1 for a theoretical discussion

[3] The limitations of DFT in LDA regarding the accuracy of the band gap are well known. Nevertheless, for the temperature considered here, conduction electrons are not excited by thermal excitation in the conduction band so that valence band can be disregarded and μ is determined relatively to the bottom of the conduction band to fix the charge carrier density.

[4] As it will be discussed for Diamond in Sec. 7, the main effect of compensation is to degrade electronic transport.

The full list of values of computational parameters is reported in App. C.2. A detailed assessment and discussion of the convergence of all the transport quantities as function of the numerical parameters is available in App. C.2.1 and Sec. 6.2.4.

6.2 Transport coefficient

6.2.1 Mobility and resistivity

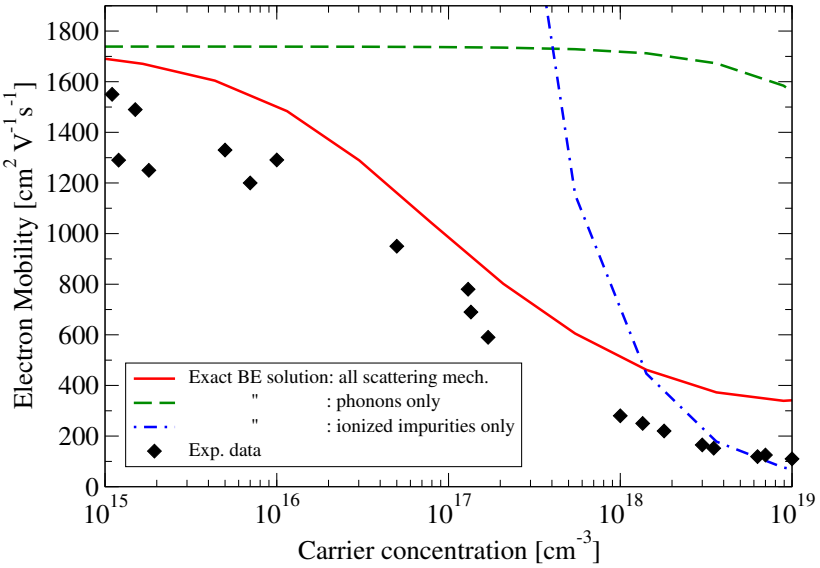

Fig. 6.1 Electron mobility against donor concentration at $T = 300K$. The red line is obtained by solving the LBE accounting for the effect of both charged impurities and phonons. The green dashed line is the solution with just phonon scattering, while the blue dashed line is obtained by just considering charged impurities. The experimental data reported are an average of many experimental measures done by different research groups[118].

Mobility calculations in Fig. 6.1, 6.2 are obtained from electrical resistivity calculation, reported in Fig. 6.3, according to the formula in Eq. 3.12. The room temperature results (Fig. 6.1) show that for carrier concentrations close to 10^{15} cm^{-3} (and lower), the mobility is mainly limited by electron-phonon interactions [5]; at higher carriers concentrations, instead, the mobility decreases as a result of an increased electron-impurity scattering. Considering $\mu_e(T)$, as the temperature increases the mobility decreases (Fig. 6.2) mainly because of a stronger electron-phonon scattering.

[5]For even smaller doping concentrations phonons keep increasing their importance until total mobility (Fig. 6.1, red solid line) reaches the upper bound represented by the intrinsic electron mobility (Fig. 6.1, green dashed line)

My results at room temperature are within the values of the many experiments reported in the literature[118–121], and it is worth mentioning that the experimental uncertainty peaks at around 10% at low doping concentration. In the case of $n_i = 10^{15}\text{cm}^{-3}$ a value of $\mu_e = 1700\text{cm}^2V^{-1}s^{-1}$ is the result of my calculations. Theoretical lattice-limited μ_e (Fig. 6.1, green dashed line) is of 1750 $\text{cm}^2V^{-1}s^{-1}$ [6]. The low-doping discrepancy with experimental results could be related to an underestimation of the electron-phonon coupling computed within standard DFT at the level of LDA. Indeed, similar shortcomings of LDA have been reported quite recently for other materials, including simple sp-bonded compounds, such as graphene[123] and diamond.[124]. Also, at high doping, the differences in the experimental data could be related to additional scattering mechanisms involving electron-plasmon interactions[74] that have not been included in this work.

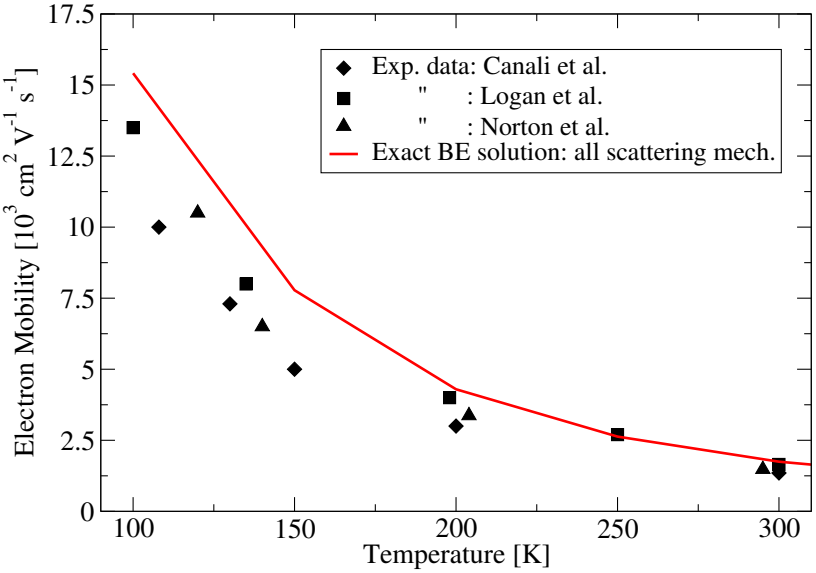

Fig. 6.2 Electron mobility as a function temperature at $n_i = 10^{14}$ cm^{-3}. The solid red line is obtained from the solution of the LBE. The experimental data are from Canali et al.[119] (diamonds), Logan et al.[120] (squares) and Norton et al.[121] (triangles).

It is interesting to compare these room temperature results with previous DFT-based theoretical work. My predictions show an improvement on other calculations employing first-principles electron-phonon coupling: Li [28] reported an intrinsic mobility value of 1860 $\text{cm}^2\text{V}^{-1}\text{s}^{-1}$ and the discrepancy is possibly due to the much denser grids used in this work, as the convergence study in App C.2.1 suggests. The importance of solving the BE on very

[6] Even for n_i of an order of magnitude equal to 10^{14}cm^{-3}, charged impurities decrease μ_e of few tens of units compared to the phonon-only limit. To not overestimate μ_e in the very low donor concentration regime, $n_i \lesssim$1E+15cm^{-3}, it is important to consider inter-valley optical phonon modes, as shown in Fig. 6.4, and the second conduction band[122].

dense k-points grid is highlighted comparing the results of Fig. 6.1 to the work of Restrepo et al. [77], where a lattice induced μ_e in the intrinsic regimes of 1970 $\mathrm{cm^2V^{-1}s^{-1}}$ was reported: in fact, in Ref. 77 the BE was not solved, and data regarding the k-points grid on which electron-phonon coupling was calculated are not available. A recent work[27] reports 1550 $\mathrm{cm^2}V^{-1}s^{-1}$ in good agreement with experimental data. It is not easy to comment on the difference between Ref. 27 and this work since first-principles calculation have been carried out in LDA as well and the Wannier interpolation scheme in very similar- however, it is interesting to note that the RTA used in Ref. 27 to calculate the electronic scattering rates, leads to a few percent points (4-5%) underestimation of μ_e as discussed in Sec. 6.3.

In passing, it is worth mentioning that many theoretical calculations in the literature are based on deformation potentials with adjustable parameters[61] to analytically model EPC in Si. In App. B, the deformation-potential approach is validated; additionally, the ab-initio deformation potential parameters obtained in this work (see Tab. B.1, B.2) are compared to both empirical[61] and other first-principles parameters[117].

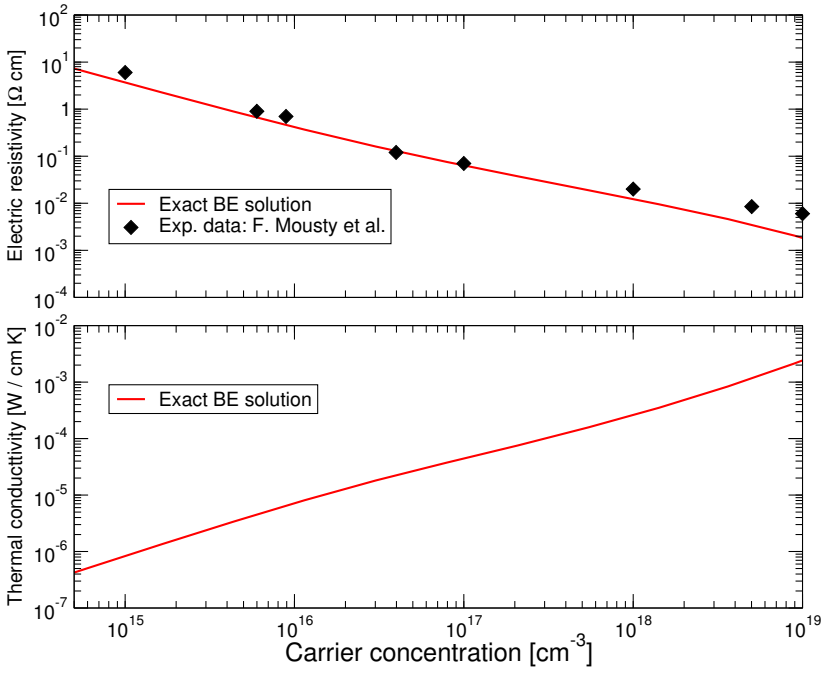

Fig. 6.3 Upper panel: electrical resistivity as function of donor concentration, n_i. Lower panel : thermal resistivity of the electrons as function of the donor concentration. $T = 300\mathrm{K}$

It is interesting at this point to analyse in more detail the contribution of the different scattering channels to the electrical transport. As shown in Fig. 6.1, information about the role of different mechanisms can be obtained switching on and off interactions when solving the

BE. This analysis, however, is only qualitative as the effects are not additive. It is possible to quantitatively inspect all scattering channels that will be defined in detail below, by exploiting the variational formula for ρ_e, Eq. 3.78, where the effect of each scattering channel on electric resistivity $\rho_e = 1/\sigma_e$ is additive. Conventionally, electron-phonon scattering mechanisms are classified not only after the branch of the phonon involved but also according to the relative location of the initial and final electronic states. To clarify this point, let's recall that the 6 Si conduction band minima are located on the three cartesian axes at around $\pm 0.75 2\pi/a_{latt}$ in the BZ; around these minima, energy iso-surfaces form *valleys* that have an ellipsoidal shape with the major axis along the cartesian direction on which the minima is located. Given these remarks, transitions are called *intra*-valley, if the electronic states lie in the same valley, *inter*-valley *f-process* if the states lie in valleys that are on different cartesian axes and finally *inter*-valley *g-process* if the states are in valleys lying on the same cartesian axis.

The panels in Fig. 6.4, show contributions to electrical resistivity from each scattering channel: ionised impurities and the 6 phonon branches from intra-valley, f-, and g-processes. In the low donor concentration regime (Fig. 6.4 upper panel), impurities are negligible. Around 55% of the contributions to ρ_e come from the intra-valley acoustic modes, which are the only relevant intra-valley modes while the remaining 45% is from inter-valley transitions. It is interesting to observe that around 35% of the ρ_e values is given by inter-valley optical mode. As n_i increases (Fig. 6.4 lower panel), impurity scattering becomes dominant, accounting for almost 70% of the resistivity value. Inter-valley channels also increase their importance relatively to intra-valley ones.

It is possible to define two electrical transport regimes: lightly-doped semiconductor, heavily-doped semiconductor. For low donor concentration, there are higher resistivity and mobility, and scattering is essentially due to the interaction between charge carriers and lattice, (see Fig. 6.4, upper panel). In the increased doping regime, resistivity further decreases because it was assumed that every donor atom is ionised at room temperature. Mobility decreases because the number of ionised impurities increases and carrier density is not sufficient yet to provide adequate screening.

6.2.2 Seebeck coefficient

While it is well known that phonon drag strongly affects the Seebeck coefficient at low temperature, T$\lesssim$ 200 K, my calculations, along with recent works[27], demonstrate that this non-equilibrium phonon effect has a conspicuous signature even at room temperature. From Fig. 6.5 it is possible to see that the phonon drag adds an almost constant contribution to

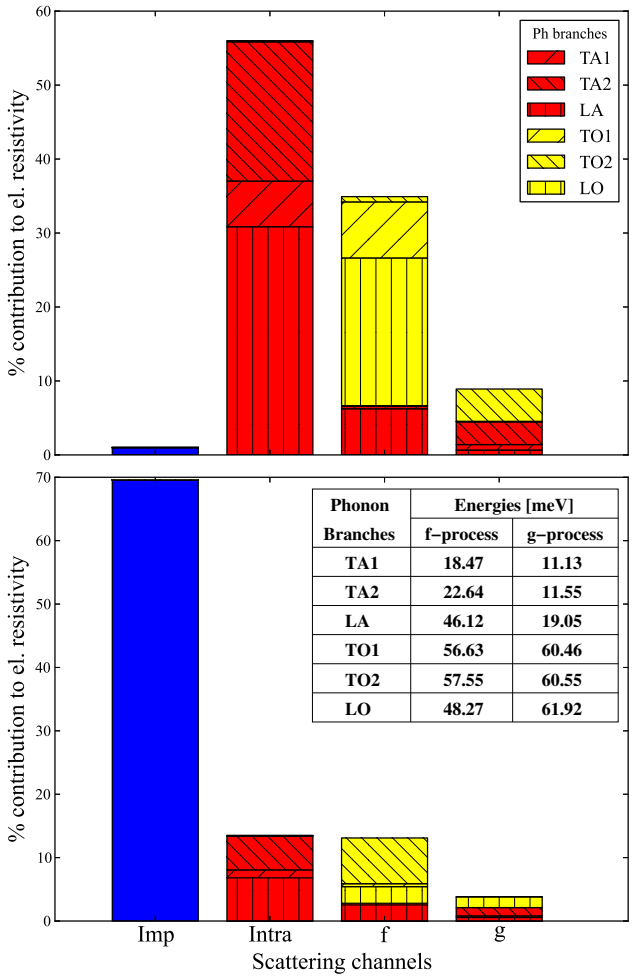

Phonon Branches	Energies [meV] f–process	g–process
TA1	18.47	11.13
TA2	22.64	11.55
LA	46.12	19.05
TO1	56.63	60.46
TO2	57.55	60.55
LO	48.27	61.92

Fig. 6.4 Breakdown of the contribution of all the scattering mechanisms to electrical resistivity at $T = 300K$. Donor concentrations are (upper), $n_i = 2.4 \times 10?14$ cm^{-3}, (lower) $n_i = 1.3^{19}$ cm^{-3}. The charged ion impurities' contribution (blue), have been separated from the one of phonons (red and yellow) across the different valleys. The phonons' processes have been further divided in intra-valley transitions and, f-processes and g-processes, that take place between perpendicular and parallel valleys respectively. As it is possible to see, the dominant f-processes are from optical phonons (yellow).

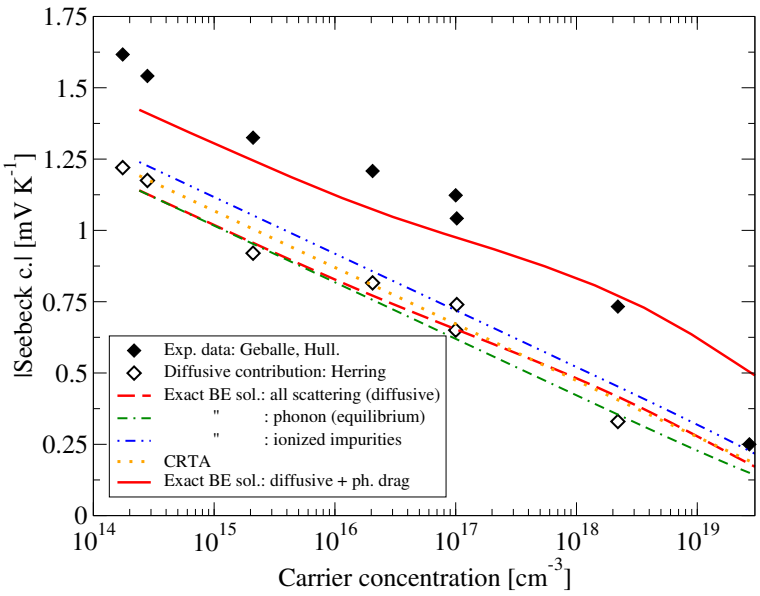

Fig. 6.5 Seebeck coefficient as function of donor concentration at $T = 300$ K. The solid red line shows the value when the phonon drag effect is taken into account along with all other scattering mechanisms, and it is in good agreement with the low-doping experimental symbols. Dashed lines represent the diffusive contribution and are in good agreement with the extimate extrapolated from the experimental results[88, 75] (open symbols).

the diffusive term from low to intermediate donor concentrations at $T = 300$K. The general trend at room temperature of total S shown in Fig. 6.5 (red solid line) for increasing n_i is determined by its diffusive part (red dashed line).

The comparison between my results for the diffusive S and the experimental findings points out that the features of S at room temperature are determined mostly by band structure rather than the details of scattering. It is interesting to note that the diffusive S agrees quite well with the prediction of the CRTA, a popular and often quite successful approximation implemented in codes such as Bolztrap[29] and Boltzwann[30]. The reason for this is that the diffusive S depends very little on the nature of the scattering mechanisms: in fact, as shown in Fig. 6.5, switching off phonon or impurity scattering when solving the BE affects the resulting value of S by less than 8%.

At low doping, my theoretical calculation slightly underestimates the measured S but the overall agreement between theory and experiment is good. This small discrepancy could be imputed to, firstly the out-of-equilibrium phonon populations that have been calculated using the SMRTA, secondly the anharmonic force constants computed on a $3 \times 3 \times 3$ supercell, that tend to underestimate the lattice thermal conductivity [91], and thirdly my calculations seem to slightly underestimate the strength of the electron-phonon coupling, as mentioned earlier.

At very high doping, for $n_i \gtrsim 10^{19}\text{cm}^{-3}$, my results are higher than the experimental data. This is due to the fact that I do not include the additional contribution of electron-phonon scattering when computing the out-of-equilibrium phonon populations [7]. In fact, as noted in Ref. 27, at high doping this *saturation effect*[75] of charge carriers on phonons should results in a substantial decrease of the phonon drag contribution and the Seebeck coefficient approaches the diffusive S. In addition, employing analytical models Mahan et al. [125] argued that finite size effects could have a noticeable impact on S when phonon drag is taken into account.

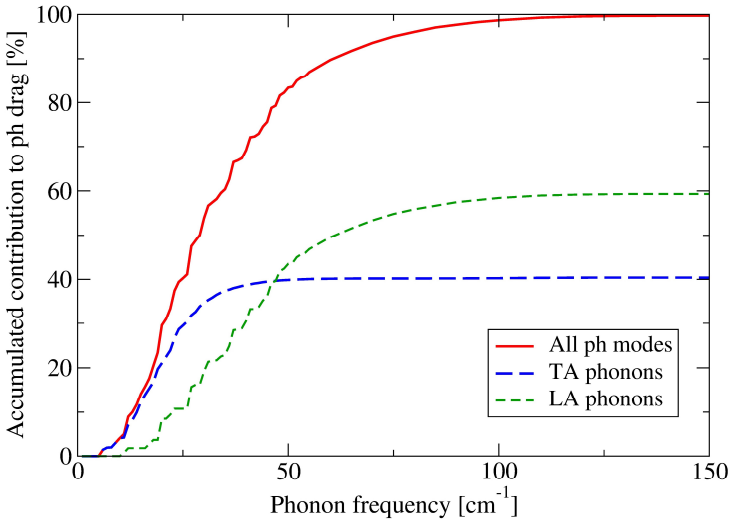

Fig. 6.6 Contribution of phonon modes to the phonon drag part of the Seebeck coefficient at $T = 300$ K and for $n_i = 1.75 \times 10^{14}$ cm^{-3}. The solid red line is the contribution from all the modes; the blue long-dashed (green short-dashed) line is the contribution from TA (LA) phonon.

The analysis of the contribution of the different phonon modes to the phonon drag part of S indicates that low-frequency acoustic phonon modes play a crucial role. For instance, Fig. 6.6 shows that phonons with frequency below 50 cm^{-1} contribute to almost 80% of the phonon drag effect, with the longitudinal acoustic (LA) modes contributing almost 60% of the total. These data confirm previous findings obtained on the basis of the relaxation time approximation[27]. As also mentioned in Ref.27, an interesting strategy to enhance the ZT could be based on a phonon frequency filtering approach in which engineered scattering of high-frequency phonons reduces the thermal conductivity without affecting the long-wavelength phonons that determine the phonon drag. Specifically, Fig. 6.6 shows that more than 98% of $S_{\text{ph}-\text{drag}}$ is accumulated already for phonon frequencies smaller and equal to

[7] See in Sec. 3.5 the discussion about the calculation of the phonon populations.

100 cm^{-1} = 3 THz, while comparing with Fig. 6.7, the lattice thermal conductivity receives most than half of its contributions from higher-frequency phonons.

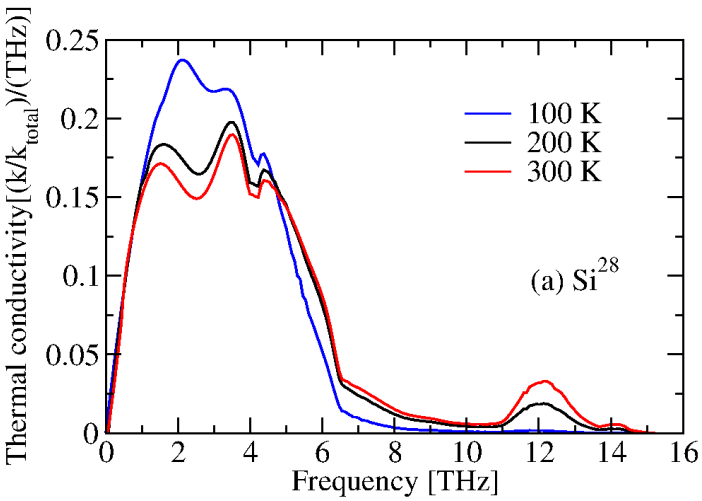

Fig. 6.7 Contribution of phonon modes to the lattice thermal 5conductivity. The red solid line refers to $T = 300$ K and shows how more than 50% of the accumulation of the lattice thermal conductivity is due to phonon frequency larger than 3 THz = 100 cm^{-1}, which is above the accumulation range of $S_{\text{ph}-\text{drag}}$ (Fig. from Ref. 91).

Fig. 6.8 shows the Seebeck coefficient as a function of temperature at low doping. It is known that the phonon drag becomes more important at low temperature, resulting in a larger correction to the diffusive S[88]. As Fig. 6.8 shows, my results capture the disagreement between theory and experiment becomes more pronounced at low temperature. This is the result of the fact that the small underestimation that I pointed out for the results at 300 K becomes more marked at lower temperature. In particular, as shown in Ref. [91], my results for the lattice thermal conductivity of silicon show slightly larger deviations at low temperatures.

6.2.3 Lorenz number

The Lorenz number, L, relates the electrical conductivity, σ_e, to the thermal conductivity of the electrons, k_e, and it is defined as in Eq. 3.19. This quantity was initially formulated for simple metals where L is almost a constant[36, 112] as prescribed by the *Wiedemann-Franz* law[113] [8]. Good thermoelectric compounds display a high degree of electronic and

[8]The Wiedemann-Franz law predicts a constant value for the Lorenz number equal to $L = 2.44 \times 10^8 \text{W}\Omega K^{-2}$. This law was formulated for systems that exhibit a free-electron-like behaviour, with elastic phonon scattering e. g. simple metals (cft. Chap. 5).

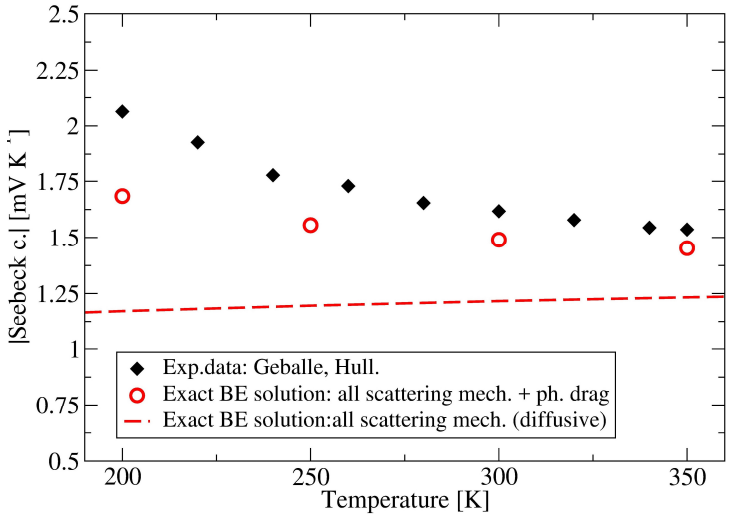

Fig. 6.8 Seebeck coefficient as a function of temperature for $n_i = 1.75 \times 10^{14}$ cm^{-3}. The black squares are the experimental data[88], the solid red line is the theoretical total Seebeck coefficient while the blue long-dashed line is the diffusive part of S.

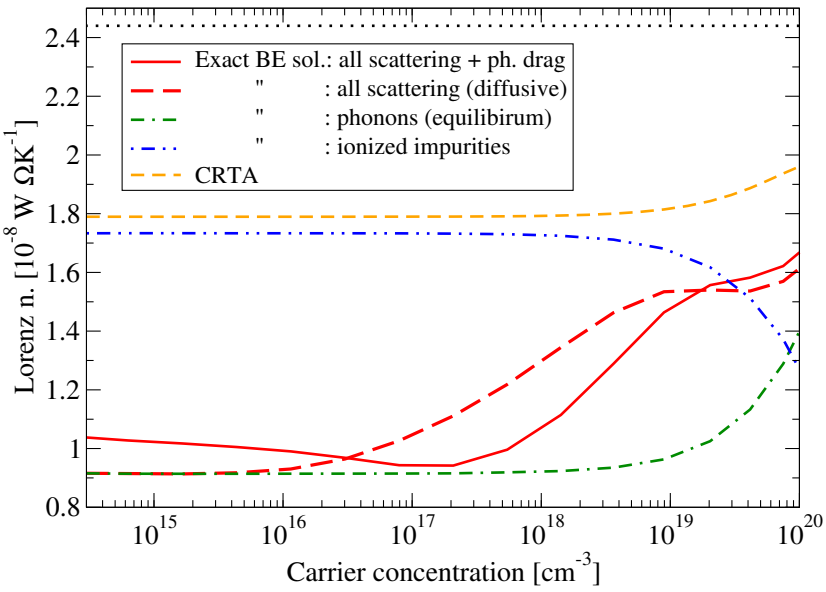

Fig. 6.9 Lorenz number, L as a function of donor concentration n_i at $T = 300K$. The red solid line has been obtained solving exactly the BE while taking into account all equilibrium phonon and impurity scattering, and phonon drag. The other lines are obtained by selecting relevant scattering mechanisms as highlighted in the legend.

structural complexity, and it is not obvious that the Wiedemann-Franz law remains valid. In fact, the Wiedemann-Franz law implies a direct proportionality between the electrical and the thermal conductivity of the electrons, making it difficult to purse the *phonon-glass, electron-crystal*[9] paradigm to enhance ZT[10]. As a consequence, a precise knowledge of L is important to accurately characterize and compare different compounds and to determine successful routes towards higher thermoelectric performance [22].

For the first-principles analysis of L at $T = 300$K, I refer to Fig. 6.9, where the Lorenz number is plotted against donor concentration. At low doping, L (red solid line) tends asymptotically to the value of 1.05×10^{-8} WΩK^{-2}. In the high doping regime, L increases towards the value predicted in simple metals by the Wiedemann-Franz law, $L = 2.44 \times 10^{-8}$WΩK^{-2}, but is still significantly smaller, with the maximum of $L = 1.65 \times 10^{-8}$ WΩK^{-2} for the range of donor concentration investigated. It is interesting to observe that while the Seebeck coefficient depends very little on the nature of the scattering mechanisms, the Lorenz number is instead quite sensitive at low concentration (see Sec. 6.2.4). As an example, the result with impurity scattering only (blue double-dotted dashed line) is quite different from the one obtained from just equilibrium phonons (green dotted-dashed line) and the CRTA (orange dashed line). This was noted also in simple single parabolic band models[17, 126].

Solving exactly the BE in a realistic system allows the theoretical evaluation of simplified models of L, that are especially useful in complex materials, such as thermoelectrics. At this point, it is interesting to discuss the model proposed by Kim et al. [127] for semiconductors and thermoelectric materials, that allows the calculation of L from the experimental observation of S,

$$L^{\text{model}}(S) = (1.5 + e^{-\frac{|S|}{116\times\text{mVK}^{-1}}}) \times 10^{-8}\text{WΩK}^{-2}. \tag{6.1}$$

This empirical formula was developed from a model-system with a single parabolic band and acoustic phonon scattering only [127]. In fact, a comparison with experimental findings shows that the model applies also to materials that should require more complex electronic band structure and additional scattering mechanisms. The transport framework developed in this work is particularly suitable to test Eq. 6.1 in a realistic scenario, since it allows to switch on and off the different scattering mechanisms, and the key physical aspects of the model system that lead to Eq. 6.1, which are the electronic bands and electron-phonon scattering,

[9] This concept has been mentioned and briefly discussed in Sec. 1.1.

[10] ZT is defined in Eq. 1.1, where σ_e appears a the numerator and k_e in the denominator.

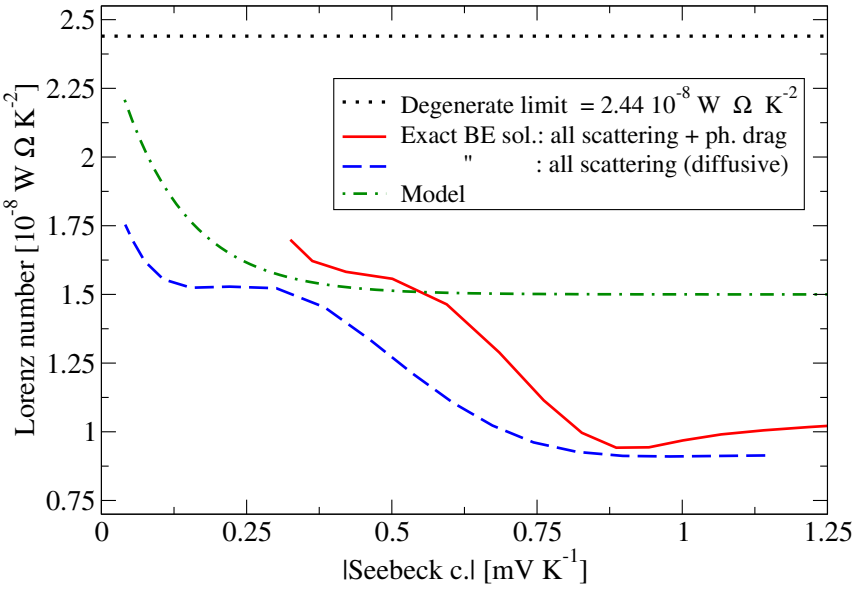

Fig. 6.10 Lorenz number, L as a function of Seebeck coefficient S. Calculations were made at $T = 300K$ varying donor concentration n_i and matching the two quantities L and S at fixed n_i . The red solid line has been obtained solving exactly the LBE while taking into account all equilibrium phonon and impurity scattering, and phonon drag. For the blue dashed line, the LBE was solved exactly as in the case before but neglecting phonon drag. The green dashed dotted line represent a simplified model [127]. The black dotted line is the Wiedemann-Franz law value.

are here considered in a genuine first-principles approach. For this purpose, I investigated L as function of S in n-doped silicon at room temperature by calculating the two quantities independently in the same range of doping concentration for which Fig. 6.5 was obtained. In this setting, low S values corresponds to high n_i and conversely, high S means low n_i.

In Fig. 6.10, L is plotted against S. The BE was solved exactly to obtain the red solid and blue dashed lines, with the former accounting for both diffusive and phonon drag effects while the latter was calculated only from diffusive scattering – impurity scattering was considered in both cases. The green dash-dotted line represents the value given by Eq. 6.1 and the black dotted line marks the value prescribed by the Wiedemann-Franz law of 2.44×10^{-8} WΩK^{-2}. As discussed in Sec. 6.2.2, it was shown that for high n_i the phonon drag effect is negligible: referring to Fig. 6.10, this implies that the blue dashed line describes L at small Seebeck coefficients $S \lesssim 0.5$ mVK^{-1}, where phonon drag is expected to be absent, while the red solid line gives the correct L prediction at higher S. The relevant regime for most thermoelectric materials is the one at low S, up until a value of $S = 0.7$ mVK^{-1}. In this range of S, the discrepancy between my first-principles calculation (blue dashed line) and the simplified formula (green dotted-dashed line) reaches the highest values of 29% at the lowest S considered; it is then fair to say that this model provides a better estimate of L than the Wiedemann-Franz law. Remarkably, in n-doped Si, I was able to explore a range of S that is larger compared to the range for which the simplified model was fitted, and this allows to report some additional features about how L depends on S. Inspecting larger values of $S > 0.7$ mVK^{-1} my first-principles calculation of L that includes phonon drag (red solid line) does not reach an asymptote at around 0.3 mVK^{-1}, as prescribed by Eq. 6.1, but decreases further, reaching an asymptotic value at high-Seebeck of around 1.05×10^{-8} WΩK^{-2}. This difference between the first-principles predictions and the model of Ref. 127 could be due to the fact that Eq. 6.1 was derived accounting just for elastic, intra-valley acoustic phonon scattering, while it was shown also in Fig. 6.4 that optical and intra-valley transitions play an important role in the high-S / low n_i regime.

6.2.4 Sensitivity of the kinetic coefficient on the scattering mechanisms

Comparing S (Fig. 6.5) with L (Fig. 6.9) it is possible to discuss the dependence of these two quantities on the scattering mechanisms. Both quantities are ratios of the kinetic coefficients of Eq. 3.32, but interestingly, they show different sensitivities to the scattering mechanisms and solution methods employed to calculate them. The most remarkable example is given by the comparison between the two CRTA results in Fig. 6.5 and Fig. 6.9: diffusive S is almost

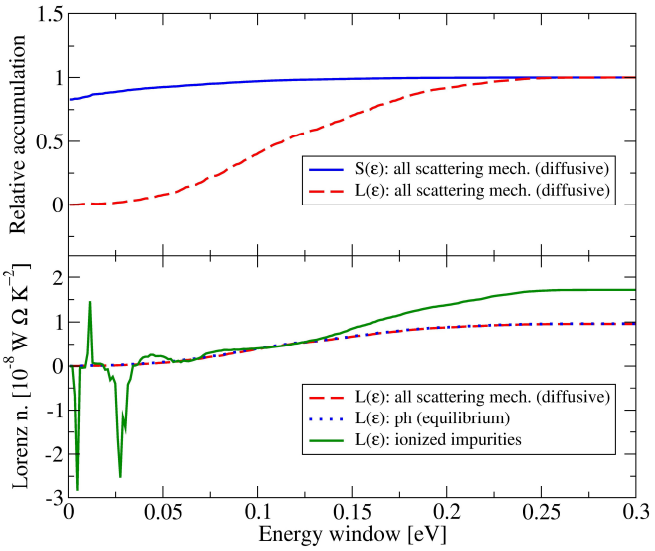

Fig. 6.11 L and S as a function of the energy window used to compute the integrals of the transport coefficients in Eq. 3.32. Panel above: relative accumulation of S (solid blue line) and L (dashed red line) computed under the assumption of phonons in thermal equilibrium. Panel below: L as a function of the energy window for different scattering mechanisms. Dashed red line corresponds to L computed with all scattering terms, while the solid green line (dotted blu line) is for the impurity (phonon) contribution. In all cases the BE at room temperature and for $n = 10^{14}$ cm^{-3} is is solved for all the states up to 0.32 eV above the bottom of the conduction band.

the same as the LBE result while L varies with discrepancies of up to a factor 2. The origin of this marked dependence on the scattering mechanisms is the result of the sensitivity of k_e on the details of these processes. Referring to equation Eq. 3.16, k_e is made of the difference of two positive quantities that accumulates in the energy spectrum over different ranges, as shown in Fig. 6.11: convergence of S with respect to the energy window is achieved in a much smaller interval than for L. This behaviour is linked to the integrand of L_{12} and L_{22} and their explicit energy dependence on $(\varepsilon - \mu)$ and $(\varepsilon - \mu)^2$ respectively. The integrand of L_{12} decays more rapidly far form μ, leading to a quicker energy convergence, less sensitive S. On the other hand, the integrand of L_{12} is more spread around μ so that a larger energy interval is available to the different scattering mechanisms to influence this quantity.

6.2.5 Kelvin relation for the electronic system with phonon drag

The Kelvin relation Eq. 3.18 is a particularly interesting finding because it suggests that the various thermoelectric phenomena that relate the reversible conversion of thermal fluxes with charge currents and vice versa have indeed a common nature[36]. In the past, doubts have been raised regarding its validity for the electronic system alone in the presence of phonon drag [128]. As discussed in Sec. 3.2, to correctly identify the kinetic coefficients, a transport formalism has to be defined first: the allowed choices of driving forces and fluxes are the ones that do not alter the entropy production [71].

Since observable quantities such as electrical and thermal conductivities are defined empirically in terms of electrical, $\boldsymbol{J}_e$, and thermal, $\boldsymbol{J}_\varepsilon$, currents (3.11), a natural pair of driving forces, $\boldsymbol{X}_{ij}$, would be the electrochemical potential, $\boldsymbol{E} = \nabla_{\boldsymbol{r}}(\phi - \mu/e)$, and the temperature gradient over the temperature, $\nabla_{\boldsymbol{r}} T/T$. I verified the Kelvin relation in the absence of phonon drag by explicitly calculating the currents, in agreement with the literature [70] as shown in Fig. C.2 This means that, in this formalism, the kinetic coefficient L_{12} corresponds to the Peltier coefficient, Π.

If the phonon drag is taken into account, I noticed that in my calculation the Kelvin relation is not satisfied. The reason for this, as made explicit by Eq. 3.63 is that the phonon drag acts as an additional driving force on the left-hand side of the BE. This implies that the new conjugate heat flux that keeps the entropy production invariant is simply not $\boldsymbol{J}_\varepsilon$ anymore. To validate the Onsager relations when electrons and phonons are dragging each other [129], first, it is necessary to solve the full BE including the steady-state electron drag on phonons, and secondly, the total thermal current has to be considered, by adding the phonon contribution to $\boldsymbol{J}_\varepsilon$. A verification of the Kelvin relation has been provided in these circumstances in the relaxation-time approximation [27].

As a final remark, my specific choice of currents and fluxes simplifies the solution the BE and provides a clear link between the currents I calculate and observable quantities. The calculations presented here lead to the correct results since S and k_e are defined experimentally: S is the ratio between the voltage and thermal difference at zero current, while k_e is the kinetic coefficient relating the temperature gradient to the thermal current when no charge is flowing.

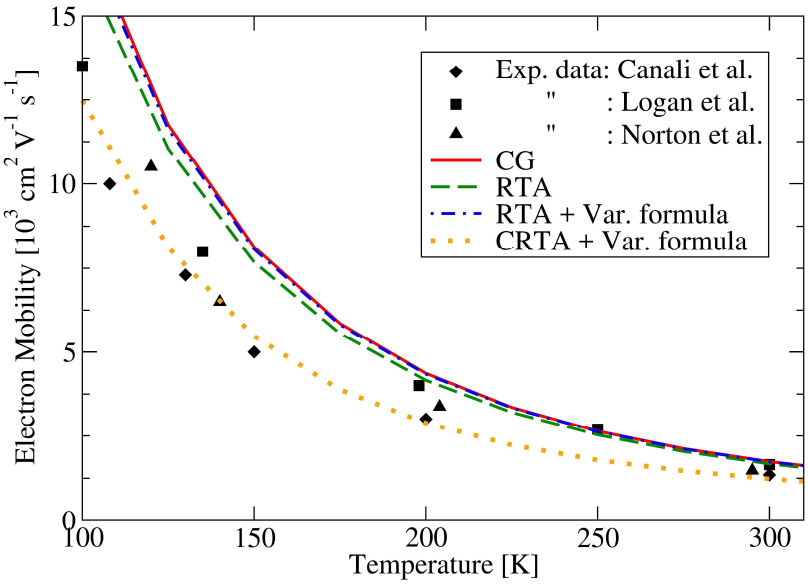

Fig. 6.12 Intrinsic electron mobility as a function of temperature computed with different approaches: solution of the BE (solid red line), relaxation time approximation (dashed green line), $v\tau_{\mathrm{RTA}}$ as trial function in the variational formula (dot dashed blue line), v as trial function in the variational formula (dotted orange line), where v is the magnitude of electron velocity. The symbols are the experimental data as in Fig. 6.2.

6.3 Approximate approaches to BE

Fig. 6.12 compares different approximate approaches within the BE framework to estimate the phonon-limited electron mobility at low doping. A popular approach is the ERTA approach, in which the effective relaxation time of Eq. 3.31 are computed according to the formula,

$$\frac{1}{\tau^{\mathrm{ERTA}}_{m\boldsymbol{k}}} = \frac{2\pi}{\hbar}\frac{1}{N_{\boldsymbol{q}}}\sum_{m',\lambda,\boldsymbol{q}} |g^{\lambda}_{mm'}(\boldsymbol{k};\boldsymbol{q})|^2 \times \Big\{ \left[f^0_{m'}(\boldsymbol{k}+\boldsymbol{q}) + n^0_{\lambda}(\boldsymbol{q})\right] \delta\left[\varepsilon_{m'\boldsymbol{k}+\boldsymbol{q}} - \varepsilon_{m\boldsymbol{k}} - \hbar\omega_{\lambda}(\boldsymbol{q})\right] + \left[1 + n^0_{\lambda}(\boldsymbol{q}) - f^0_{m'}(\boldsymbol{k}+\boldsymbol{q})\right] \delta\left[\varepsilon_{m'\boldsymbol{k}+\boldsymbol{q}} - \varepsilon_{m\boldsymbol{k}} + \hbar\omega_{\lambda}(\boldsymbol{q})\right] \Big\} \quad (6.2)$$

which is analogous to Eq. 3.72. As shown in Fig. 6.12 this approach gives mobilities that are around 4-5 % lower than the exact solution of the BE.

It is interesting to see how well the variational formula for σ_e (Eq. 3.78) reproduces the exact LBE calculation when used with the approximate approaches of Sec. 3.6.1. Using this formula with the exact solution of the LBE, $\tau = \tau^{LBE}$ would, of course, give the same result

as the one pictured by the red solid line, that will be used as a reference. Using τ^{ERTA} gives a μ_e that is less than 1% below the exact result. Surprisingly τ^{CRTA} leads to a result that is in excellent agreement with the experimental results, but that is 30% below reference values, suggesting that the agreement with observation is just due to fortuitous error cancellations.

Chapter 7

Diamond: electronic transport for next-generation electronics

Diamond is one of the most promising materials for a new generation of energy-efficient, high-performance and tough electronic devices for applications ranging from power electronics to bio-sensors and high-energy-physics detectors [130]. This is due to its superior thermo-mechanical, chemical and transport properties: it is very hard, chemically inert and heat tolerant, and it has extraordinary high values of breakdown voltage, thermal conductivity and carrier mobility [131]. Although significant progress towards diamond-based electronics has been made in the last two decades, further advances are needed to better understand and take full advantage of the exceptional potential of this material.

The aim of this chapter is to study Diamond for nano-electronic applications, so that the attention will be posed on those transport regimes that lead to the best electronic transport performance. For this reason, the theoretical investigation refers to p-doped single-crystal samples, in the intrinsic and in the valence-band conductivity regimes (with acceptor density $\lesssim 10^{19}\text{cm}^{-3}$), and in the case where compensation between acceptor and donor impurities is absent. Compensation is a key aspect of Diamond syntheses and plays an important role in degrading the electric transport performance because of the reduction of the number of available carriers, and of the increased neutral impurity scattering [132].

From an experimental point of view, the dependence of σ_e on T and boron density has been interpreted phenomenologically with the sum of three Arrhenius terms [133, 134] accounting for different hole conductivity mechanisms. The first contribution comes from valence-band conduction, the second from hopping between occupied and unoccupied acceptors and the third from impurity-band conduction, the first two being the most important. In the case of nano-crystalline and poly-crystalline samples, a model for carriers' hopping

between grain boundaries has been proposed [135] but the expected contribution at room temperature appears small[132]. At $T = 300$K and for $n_a \lesssim 10^{19}\text{cm}^{-3}$, transport is mainly regarded as being of the valence-conduction kind, whilst nearest-neighbor hopping becomes important at concentrations between $n_a \gtrsim 10^{19}\text{cm}^{-3}$ and the Mott transition threshold [136],which takes place at around $n_a = 3 \times 10^{20}\text{cm}^{-3}$.

The analysis presented in this chapter is mainly focused on the hole mobility, μ_h. This quantity has been at the centre of intense research efforts but still presents important open questions. For instance, the values reported in literature for the intrinsic hole drift mobility at room temperature vary significantly, ranging from 2000 to 3800 $\text{cm}^2\text{V}^{-1}\text{s}^{-1}$. Indeed, Isberg and coworkers [137, 138] performed Time-of-Flight (ToF) measurements on photo-excited carriers in intrinsic single-crystal CVD diamond and reported exceptionally high hole mobilities, between 2600 and 3800 $\text{cm}^2\text{V}^{-1}\text{s}^{-1}$, significantly larger than in other group IV semiconductors such as silicon (500 $^2\text{V}^{-1}\text{s}^{-1}$) and 4H-SiC (100 $^2\text{V}^{-1}\text{s}^{-1}$). Similar measurements (using photo-induced and α-particle-induced currents) have been reported to be around 2000 $\text{cm}^2\text{V}^{-1}\text{s}^{-1}$ [139] and between 2000 to 2250 $\text{cm}^2\text{V}^{-1}\text{s}^{-1}$ [140]; more recently, Jansen et al.[141] reported values of 2500 $\text{cm}^2\text{V}^{-1}\text{s}^{-1}$.

The $\mu_h(T)$ temperature dependence is another feature that is at present unclear. For instance, in both undoped synthetic diamond and natural diamond the measured hole mobility varies as T^α, with $\alpha \approx -1.5$ at temperatures below ~ 350 K, while for higher temperatures a steeper dependence, with α between -2.8 and -3.2, was observed [142, 140, 143]. While the low-temperature behaviour has been ascribed to acoustic phonon scattering [142, 86], the origin of the steeper dependence above 350 K is still unclear, and it has been attributed by some authors [142, 86] to optical phonon scattering and by others [144] to ionised impurity scattering. The accurate characterisation of the relevant scattering mechanisms and their temperature dependence is important for the development of diamond-based devices operating at high temperature.

7.1 Boron ionization in Diamond

A correct comparison between theoretical predictions and experiments is possible only if the Boron concentration, n_a, its ionised fraction, n_i, and the hole density, n_p, are known. The precise experimental investigation of these three quantities is non-trivial. To measure n_a, the technique that is considered to give most reliable outcomes is Secondary Ion Mass Spectroscopy (SIMS) [145], but it is a destructive analysis tool that is not always used in diamond research. Another aspect that has been mentioned earlier is the compensation

between ionised acceptor and donor impurities, that is characterised by specifying the donor density and the ionised donor fraction. The uncertainties in n_a, n_i and n_p are the main reasons why experimental measures are so spread out (cft. symbols in Fig. 7.3, 7.2), especially if older works are compared with more recent ones [145]. As a result of this complicated, and sometimes incomplete, experimental characterisation, the comparison between theoretical predictions (lines) and experiments (symbols) is not immediate. When presenting my calculation in Sec. 7.2 and Sec. 7.3, I will explicitly point out which experimental sample are the most suitable for a direct comparison.

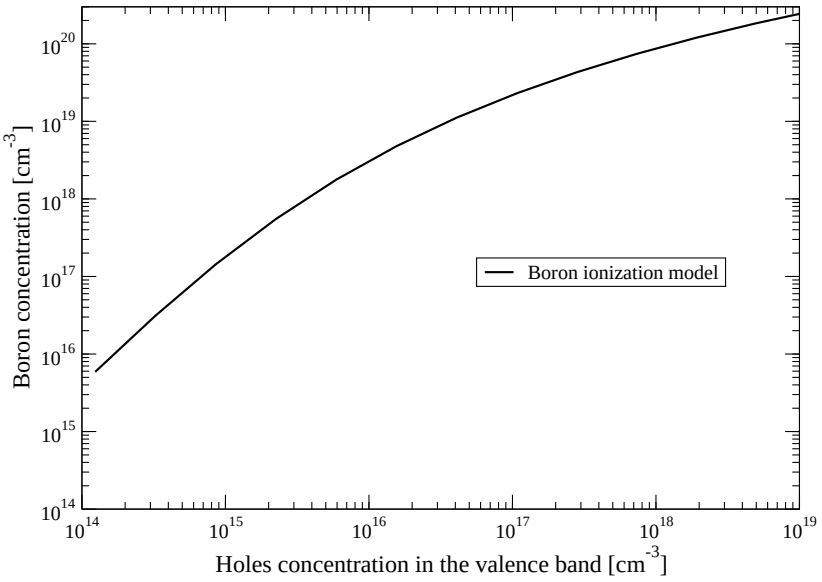

Fig. 7.1 Total acceptor concentration versus ionised acceptor concentration as predicted by model in Eq. 7.1, 7.2 at $T = 300$K.

The neutrality equation has been resolved in order to obtain the density of free holes, ionised impurities, and neutral impurities: these are the key ingredients that are used in the BE. Boron is effectively an acceptor impurity and its ionised fraction determines the valence band holes at $T \lesssim 1000$K: intrinsic carries can be neglected due to the wide gap (5.57eV)[146]. The relation between the densities of acceptors, n_a, donors, n_d, holes n_p is given by Isberg [146],

$$\frac{n_p(n_p+n_d)}{n_a-n_p-n_d} = \frac{N_v}{g_a} e^{-\frac{E_a}{k_B T}} \tag{7.1}$$

where $N_v = 2\left[m_{h,dos}k_BT/2\pi\hbar^2\right]^{3/2}$ is the valence band effective density of states, with $m_{h,dos} = 0.8m_e$ is the holes' density of state effective mass. $g_a = 6$ and E_a are the spin degeneracy factor and the activation energy of Boron. E_a is another important qunatity and depends itself on n_a. Pearson and Bardeen [147] developed a model of this dependence in Silicon which has been successfully applied to Diamond[132],

$$E_a = E_{ion} - \alpha_a \sqrt[3]{n_A}. \tag{7.2}$$

The parameters that best fit the experimental observations are discussed in Ref. 132 and were reported as $E_{ion} = 0.37$ eV and $\alpha_a = 0.51 times 10^{-8}$ eV cm^{-1}, where E_{ion} corresponds to the ionization energy for an isolate impurity center. The combination of these two models holds for acceptor densities below $\approx 3 \times 10^{20}$cm^{-3} where a Mott transition takes place, and for a range of temperature around 200K to 1000K [146, 132]. In Fig. 7.1 is shown the density of ionised impurities versus the donor density as given by the combination of Eq. 7.1 and Eq. 7.2.

7.2 Mobility and resistivity at room temperature

Our calculations at $T = 300$K give a theoretical prediction of ρ_e and μ_h versus boron concentration for single-crystal diamond with no compensation. The sample type theoretically investigated here is the one that's most suitable for electronic application, leading to the best electronic transport performance, and provides a theoretical reference for experimental characterisation.

In Fig. 7.2 the predicted value of $\rho_e(n_a)$ is presented (red solid line). As expected, the resistivity decreases with increasing boron concentration. A comparison between this result and the first-principles lattice-limited calculation (green dashed line) suggests that the value calculated is due to electron-phonon interaction in the lower doping regime: the difference between the red solid and green dashed lines ranges is around 17% at $n_a = 10^{16}$cm^{-3}, $n_p \approx 2 \times 10^{14}$cm^{-3}; also, in this regime, the prediction agrees with phenomenological valence band conduction models [145]. At around $n_a = 10^{17}$cm^{-3} scattering from both neutral and ionised impurities starts to play an important role and becomes the dominant mechanism above $n_a = 10^{18}$cm^{-3}.

Comparing with experiments (Fig. 7.2, symbols), the theoretical value (red solid line) acts as reference for best electronic performance, providing a lower bound for ρ_e. Also, it is worth mentioning the good agreement with samples that show the lowest compensation,

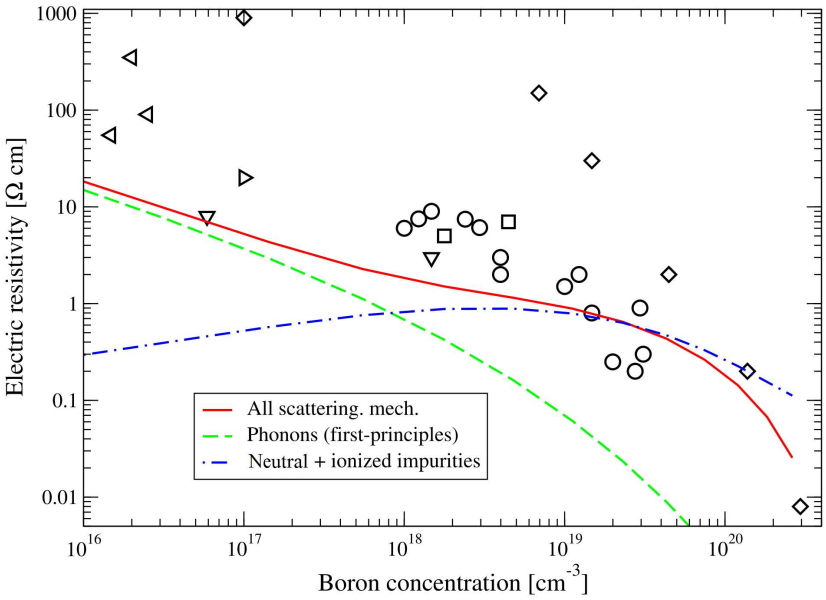

Fig. 7.2 Electrical resistivity as function of the Boron concentration, $T = 300$K. This calculation refers to a single crystal system with no compensation and accounts for valence hole conduction. The symbols represent several experimental observation from the literature, collected by Barjon et al. [145].

which are the symbols that, for a given n_a have the smallest resistivity, particularly the samples pictured with open circles and open diamonds, for which Boron concentration was measured via SIMS[134, 145]. This results confirm the overall good quality of both the ab-initio calculation and doping models put in place for the calculation.

It is possible to note that the theoretical prediction overestimates some of the open circles at around $n_a \gtrsim 10^{19}\text{cm}^{-3}$. This can be imputed to the onset of hopping conductivity, which is a conductivity mechanisms that is not considered in the theoretical calculation and contributes to lowering the total ρ_e; to this extent, it is worth mentioning that phenomenological models underestimate ρ_e much more severely [145].

At even higher Boron densities $n_a \gtrsim 10^{20}\text{cm}^{-3}$, the agreement between my calculation and the experiment is stronger. Interestingly, the electrical resistivity calculated from impurity scattering only (blue dashed-dotted line) sits above the value calculated considering all the scattering mechanisms. This finding could highlight a regime in which the well know and widely used Matthiessen's rule [70] is violated, thus providing an example in which the

exact solution of the BE is absolutely necessary to predict the correct value of the electric resistivity.

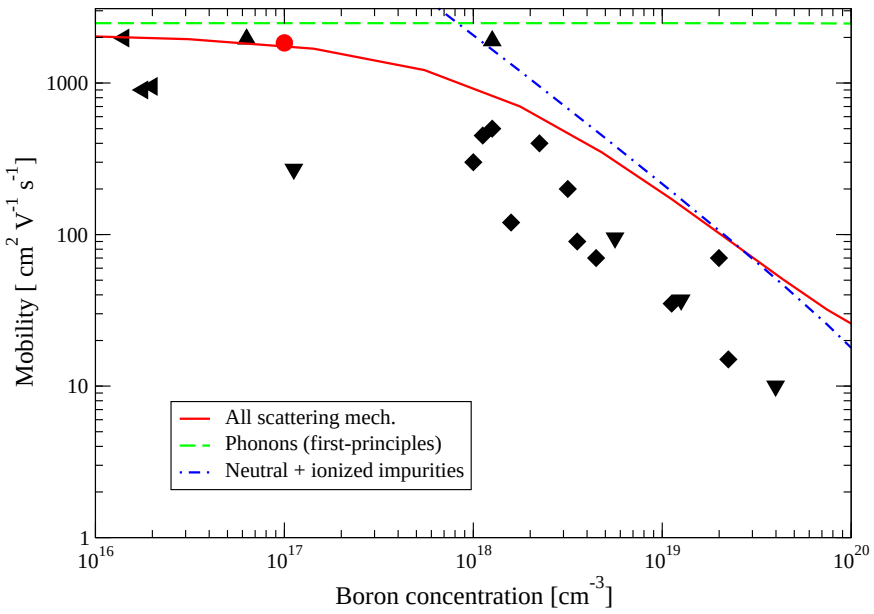

Fig. 7.3 Hole drift mobility against Boron concentration, $T = 300$K. As in the case of resistivity, this theoretical prediction applies to a single diamond crystal with no compensation exhibiting valence conduction only. Experimental symbols account for many different experiments and has been taken from Barjon et al. [145]

In Fig. 7.3, the predicted $\mu_h(n_a)$ at room temperature (red solid line) is shown. Our data agree with other theoretical studies base on RTA that employ similar models for impurity scattering with adjustable EPC parameters[86], and with semi-empirical valence band mobility models [145]. The presented predictions serve, as in the case of ρ_e, as a upper-bound reference for samples with the best electronic transport performance, that have the highest mobility at a given n_a; as an example, we can cite natural type II Diamond[1], with measured μ_h values between $2050-2140$ cm^{2}V^{-1}s^{-1} using ToF techinque [142], and the samples of Yamanaka et al. [148] (red full circle) that is accurately characterized in its n_a and compensation values and shows good agreement with the prediction of this work (red solid curve).

[1] In this type of sample Boron impurity in low density are naturally presents. It also shows low levels of compensation by Nitrogen donors.

The green dashed line shows the calculated lattice-limited μ_h, where a value of 2500 $\mathrm{cm^2V^{-1}s^{-1}}$ has been obtained in the near intrinsic regime, at an hole density of $n_p = 10^{14}\mathrm{cm^{-3}}$: experimental values of intrinsic μ_h in artificial samples[2] have been reported in the range of 2000-3800 $\mathrm{cm^2V^{-1}s^{-1}}$; the predicted value is within the experimental uncertainty with the experiment performed by Tranchant et al. [143] while is not compatible with the extraordinary results of Isberg and coworkers [137, 138]. In this regard, it is important to notice that my ab-initio results based on DFT in LDA, could slightly overestimate the intrinsic mobility value; indeed, it has been recently shown that LDA tends to underestimate the electron-phonon coupling in simple sp-bound compounds[3], diamond [124] and graphene [123].

As a side-note, it is interesting to notice that in diamond, $\mu(n_a)$ spans two orders of magnitude in the doping range of Fig. 7.3, while in other semiconductors (cft. for instance Si, Ge, GaAs) the variation of μ is within one order of magnitude in the same doping range. This difference is due to a complex dependence of carrier concentration and impurity scattering on boron density, as opposed to a complete ionization of donors/acceptors in other systems at $T = 300\mathrm{K}$. Partial boron ionization in diamond results in the presence of both neutral and charged impurity scattering centres with charged ones poorly screened because of the low carrier density. As a consequence of these observations, impurity scattering fully determines the pronounced decrease of $\mu(n_a)$ at high boron concentration, as can be seen by comparing the results with all scattering mechanisms (red solid line) with the one from impurity scattering only (blue dashed-dotted line) in Fig. 7.3.

7.3 Temperature dependence of Mobility

In Fig. 7.4, the lines show the calculated mobility as function of temperature for boron concentrations ranging from $n_a = 10^{13}\mathrm{cm^{-3}}$, which represent the near intrinsic regime, to $n_a = 10^{16}\mathrm{cm^{-3}}$. Mobility decreases with temperature but still has a value of around $500\mathrm{cm^2V^{-1}s^{-1}}$ at 500K, which is a high value if compared to other wide-gap semiconductors important for high temperature electronics: for instance, 4H-SiC shows a hole mobility of around $30\mathrm{cm^2V^{-1}s^{-1}}$ at the same temperature [149]. We compare our predicted $\mu_h(T)$ with the experimental findings of Reggiani et al. [142] where drift mobility[4] was measured in

[2]These samples were growth using CVD technique, therefore are absolutely pure, insulating samples. By exciting valence electrons, holes are created and their mobility can be measured with ToF techniques.

[3]This possible overestimation is also noticeable in silicon a mentioned in Chap. 6 and in Ref. 90.

[4]Drift mobility measures provides direct access to μ_h with the formula, $\boldsymbol{v}_d = \mu_h \boldsymbol{E}$, where $\boldsymbol{v}_d$ is the *drift velocity* of carriers and $\boldsymbol{E}$ is the electric field. Another popular experimental technique is Hall mobility, in which

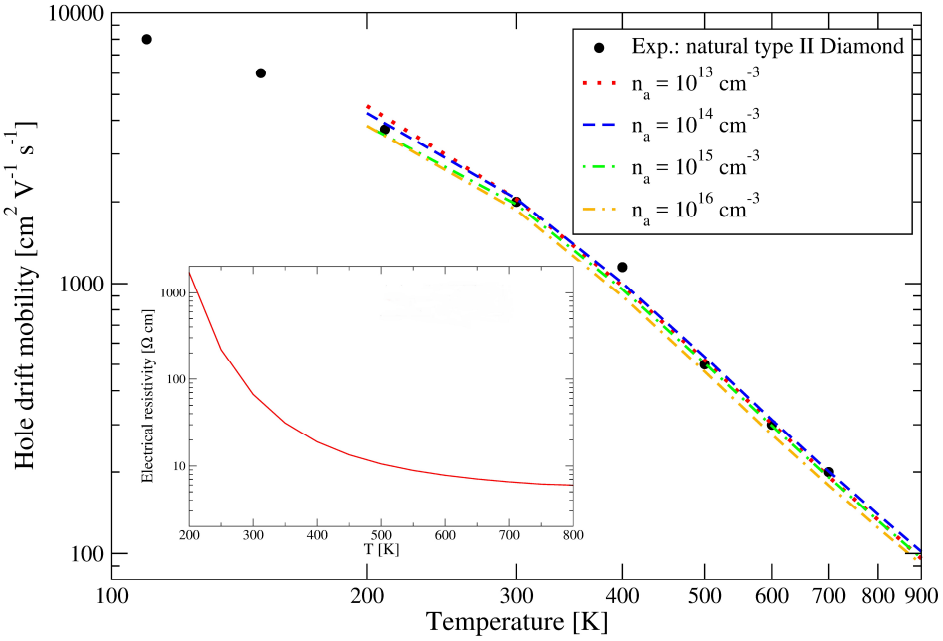

Fig. 7.4 Hole drift mobility against temperature, for a natural type II Diamond sample of [142]. The experimental mobility has been calculated by ToF measurements. Calculated values are pictured for different boron concentrations. Theoretical electrical resistivity is presented in the inset for $n_a = 10^{14}$ cm^{-3}.

samples of natural type II Diamond that naturally contains light boron concentrations and very low compensation from nitrogen donors [137]. Our predicted mobility in the nearly intrinsic regime, dominated by phonon scattering, reproduces very well the experimental data (Fig. 7.4, symbols)

As mentioned in the introduction to this chapter, it is interesting to note that the dependence of μ_h on the temperature exhibits two regimes with different slopes in the log/log plot [138], with the change between the two taking place between 300-400K. It is evident from Fig. 7.4 that the two regimes are present for all the doping values investigated, which hints at an important role of phonons. A precise explanation is available by inspecting the effect of the different scattering mechanisms on $\rho_e(T)$ and consequently $\mu_h(T)$, which are discussed in the next paragraph.

case $\mu_h = R_H \sigma_e$, and R_H in the *Hall coefficient*. R_H can be estimated with some degree of approximation[86, 150] and the Hall experimental results can differ from drift-velocity measures[138].

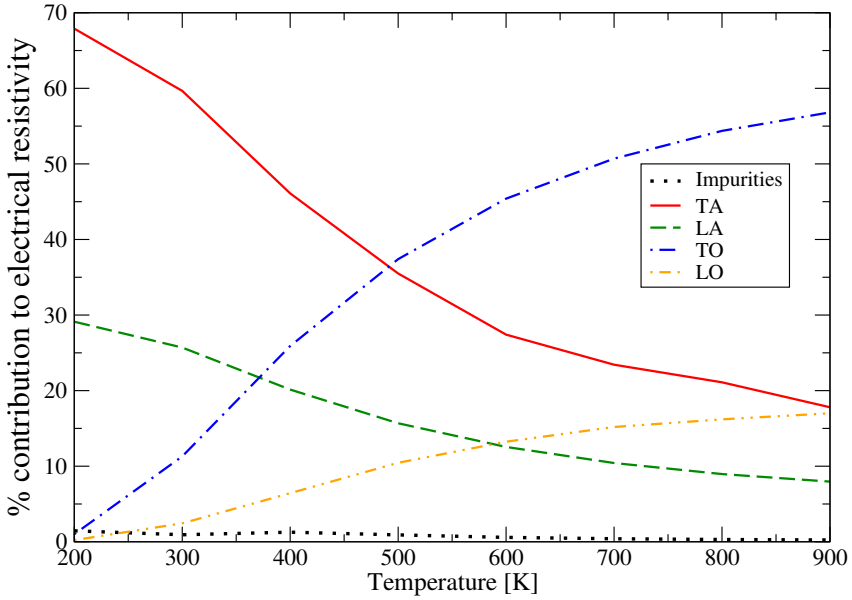

Fig. 7.5 Percentage contribution to ρ_e of the different scattering mechanisms as function of the temperature at $n_a = 10^{15}\text{cm}^{-3}$. The corresponding ρ_e values are shown in the inset of Fig. 7.4.

In Fig.7.5, the contributions of the different scattering mechanisms to $\rho_e(T)$ for $n_a = 10^{14}\text{cm}^{-3}$ (inset Fig. 7.4, red solid line) are discussed[5], as calculated with Eq. 3.78. Impurities have a small role because of the near-intrinsic regime. A trend is clear for increasing temperature: optical phonon modes gain importance over the acoustic ones [6]. This observation can be explained inspecting the energy and temperature dependence of the equilibrium phonon distribution, n^0_λ on the basis of the large difference in energy between the two sets of branches: close to the Γ point, optical modes have an energy of approximately 160 meV, while acoustic branch energy reaches at most one eighth of this value at the limits of the relevant transport volume of the BZ. The exponent $\hbar\omega_\lambda/k_BT$ in n^0_λ penalizes high energy modes over low energy ones: this effect is stronger at low temperatures and diminishes at higher temperatures.

Inspecting the values of the different contributions in Fig. 7.5, it is possible to see that at $T = 300\text{K}$, acoustic modes dominate with 87% over the optical ones, nevertheless, optical

[5]This analysis is similar to the one of Si in Sec. 6.2.1

[6]Notice that since the valence band maximum in diamond is at Γ, only phonon modes around Γ are relevant for transport in p-doped samples.

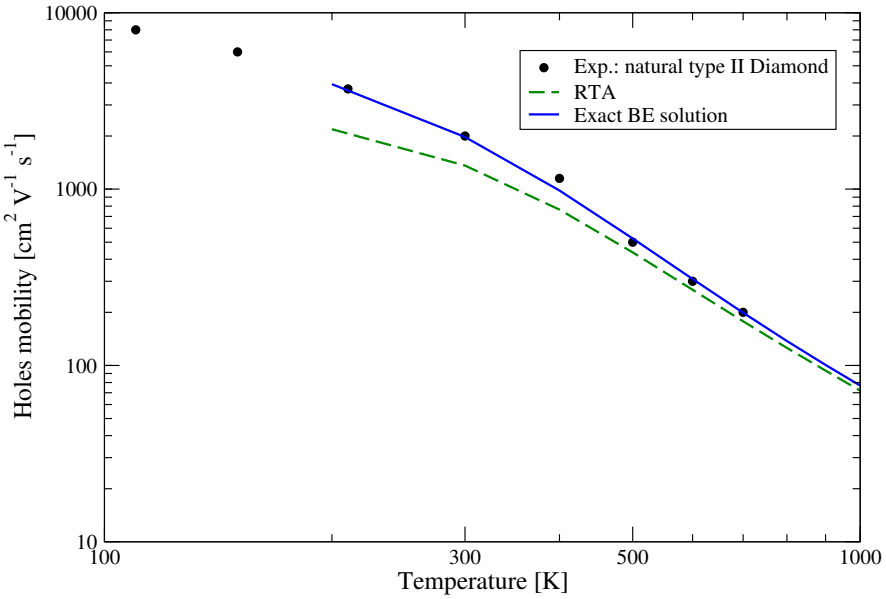

Fig. 7.6 Comparison between $\mu_h(T)$ obtained from the exact BE solution (blue solid line) and RTA (gree dashed line) in Diamond, $n_a = 10^{15}\text{cm}^{-3}$. The RTA underestimate the hole mobility especially at low temperature.

modes contributions add up to 11%. It is then interesting to compare this result with our findings for Silicon (see. Fig. 6.4, upper panel) [7]. Si optical modes at Γ have energies that are around 2.5 times smaller than in Diamond, thus resulting in larger populations, but in spite of this give no contributions to ρ_e (see intra-valley phonons in Fig. 6.4). This comparison indicates that EPC of optical modes in Diamond is stronger than the EPC of acoustic modes in the same system and than the EPC of optical modes in Si, thus giving a noticeable contribution even a room temperature. Increasing the temperature, the split is almost even at around $T \approx 525$K. Eventually, optical modes become the most important with a total amount of 76% over a 24% of acoustic modes.

This analysis of the different scattering contributions to $\rho_e(T)$ also explains the temperature dependence of μ_h. The slope change in the log/log plot of $\mu_h(T)$ between 300-400K (Fig. 7.4, blue solid curve) is imputable to the change in electrons' main scattering channel: from acoustic phonons for $T \lesssim 300$K to optical phonons for $T \gtrsim 500$. This clarifies earlier experimental observation of intrinsic drift mobility[138].

[7] Notice that Silicon was doped with donor impurities

Finally, it is interesting to notice (see Fig. 7.6) that a simpler approach such as the relaxation time approximation significantly underestimates the result obtained from the full solution of the linearised Boltzmann equation, especially in the low-temperature regime.

Chapter 8

Conclusion

In this work the eBET HPC infrastructure for electronic transport was developed and implemented (Chap. 4) and succesfully applied to a number of materials (Chaps. 5, 6 and 7). eBET allows the calculation of a range of transport coefficients (electrical conductivity, mobility, electronic thermal conductivity, Seebeck coefficient and Lorenz number) in bulk homogeneous metals and doped semiconductors. This infrastructure is characterized by two main highlights: firstly the electronic transport coefficients are calculated from the exact solution of the linearized BE via a fast and stable conjugate gradient algorithm, and secondly band structure, phonon dispersion and EPC are computed via Wannier interpolation on arbitrarily fine meshes in reciprocal space, starting from DFT results. This second feature allows a vast increase in the accuracy and performance of these demanding calculations. In addition, the bottleneck represented by calculating EPC from first principles has been further mitigated by means of a double mesh scheme in which EPC matrix elements are stored on a coarse grid, while the BE is solved on a fine grid with an interpolation of the EPC function g^{λ} between the two meshes. The input of this software infrastructure is obtained through standard DFT and DFPT calculation using Quantum-ESPRESSO [58] and then stored on the MLWF basis using wannier90 [65] and EPW [67].

The current implementation also includes other useful features. For instance, it allows the use of phenomenological models for the interaction between electrons and ionised or neutral impurities, which is crucial to treat doped semiconductors. The code also provides the opportunity to use deformation potential models for the EPC, which is a very interesting option in case the EPC from DFT is not available or simply not accurate enough. Another interesting feature is the possibility to compute transport coefficients with approximate methods, such as the relaxation time approximation or variational approaches; this option is useful as it provides a way to test and compare with works done in the past and to

characterise in alternative ways the relative importance of the different scattering channels. Finally, it is important to mention that the code also allows the calculation of effects due to non-equilibrium populations of phonons that arise in presence of a thermal gradient. The study of these effects is important to understand the coupled electron-phonon dynamics in doped semiconductors and accurately predict transport quantities, such as the Seebeck coefficient, that are essential to engineering thermoelectric and semiconductor devices.

In this PhD work this computational infrastructure has been used to predict electronic transport coefficients in a number of systems.

Aluminium and Copper (Chap. 5) were chosen to initially test and validate the computational approach. Indeed, the transport properties in the intrinsic regime of these simple metals have been extensively studied in the past also within a DFT framework. Overall good agreement with experiments and with previous first-principles results was achieved. The findings of this work confirmed earlier theoretical predictions where the simplification of LOVA to BE was employed to calculate transport coefficients [107, 106]. In the case of copper, the slight disagreement with experiments suggests possible inaccuracies of the LDA band structure or EPC that will require further studies.

As a second application, the thermoelectric properties of n-doped silicon (Chap. 6) were studied in wide temperature and donor concentration ranges. Overall, a good agreement with experiments was obtained. Using the developed framework, it was possible to accurately characterise the role of the different scattering mechanisms on the various transport coefficients. For instance, it was possible to highlight the importance of optical phonons on ρ_e even at room temperature. In addition, the analysis of the individual phonon mode contributions to S due to phonon drag confirmed the possibility, proposed in Ref. 27, to enhance ZT through a phonon frequency filtering approach, in which phonon scattering is engineered in such a way to preserve the beneficial effect of low-frequency phonons on the Seebeck coefficient while reducing the contribution to the thermal conductivity of high-frequency modes. As a final interesting outcome of this study, it was possible to assess the accuracy of simplified models and approximations popular in the electronic transport community; firstly, first-principles parameters were provided for deformation potential models of EPC (App. B), secondly the accuracy of the various flavors of RTA was quantified against the exact solution of the BE, and thirdly an empirical model for L [127] useful in TE material characterization was validated.

As a final application, the electronic transport in Boron-doped Diamond was investigated for high-performance electronics. The additional challenge here with respect to the case of Silicon is the non-trivial doping mechanisms for which it was necessary to rely on

phenomenological models. The details of the Boron ionisation and impurity scattering models were studied to assess their effectiveness in simulating scenarios of technological interest. ρ_e and μ_e were calculated in a wide range of temperature and Boron concentration in order to determine the theoretical limits for the best electronic properties attainable with synthetic samples. An intrinsic room-temperature hole mobility of 2500 $cm^2\ V^{-1}\ s^{-1}$ was predicted, confirming the high values obtained with ToF measurement on undoped synthetic and natural diamond. Finally, the analysis of the scattering mechanisms provided a clear explanation for the slope change in the log/log plot of $\mu_e(T)$; optical phonons in diamond play a non-negligible role even at room temperature and become the dominant scattering mechanism above 500K, fully determining the mobility in the high-temperature regime.

8.1 Future outlook

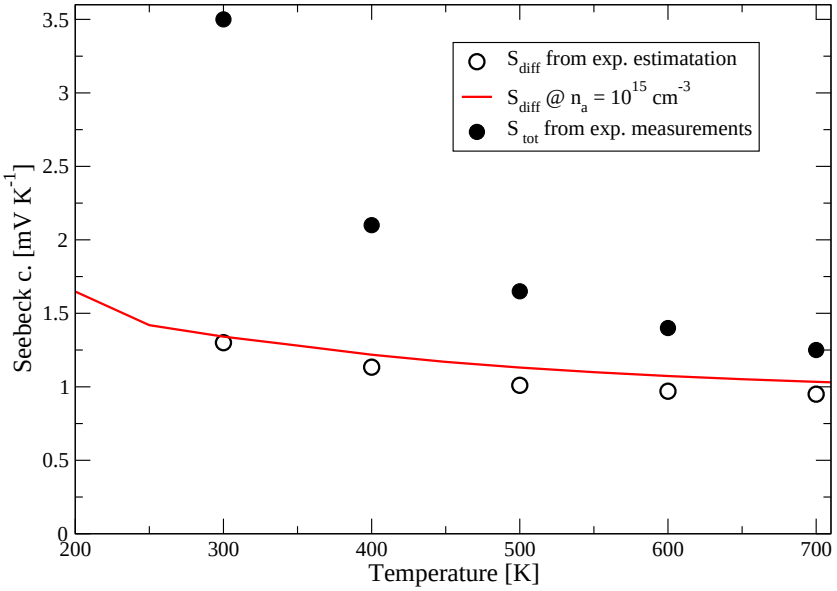

Fig. 8.1 Seebeck coefficient against temperature, for a natural type IIb Diamond sample (solid red lines). Open circles are an estimation from the experimental observation of total S [89].

Immediate interesting developments of the work presented insofar involve the study of the large phonon drag contribution to S in Diamond. In Fig. 8.1, the prediction is shown for the

temperature dependence of the diffusive contribution to S of a single-crystal, uncompensated sample that represents a good description of the type IIb Diamond investigated by Goldsmid et al. [89]. This calculation quantifies the effect of phonon drag on total S as function of T (Fig. 8.1 solid black circles). Here it is possible to observe that the phonon drag contribution ranges from $S_{\mathrm{ph-drag}} \approx 150\% S_{\mathrm{diff}}$ at room temperature, to $S_{\mathrm{ph-drag}} \approx 40\% S_{\mathrm{diff}}$ even at $T = 700$K which is the highest temperature for which the sample has been experimentally investigated[89]. The magnitude of this enhancement is remarkable, especially if compared to other covalent-bond semiconductors[75] such as Silicon [90, 88, 27] and Germanium[87], where the phonon drag contribution is smaller and less extended in temperature range (see Sec. 6.2.2 for comparison with Si). To proceed with the investigation of the total S, it is necessary to compute the steady-state phonon population in presence of a thermal gradient; in the case of diamond this requires the full solution of the phonon BE that includes anharmonicities, and eventually boundaries and isotopic scattering [76]. Once these phonon populations are known the methodology used for silicon can be directly applied.

Another possible direction of research concerns the temperature dependence of the Seebeck coefficient in elemental metals. In particular, it will be interesting to perform a systematic study of Cu, Ag, Pt, Pd and Al bulk systems to understand the origin of the anomalous sign of S in Group 11 metals, particularly Copper and Silver. Materials with n-type carriers usually display a negative S, as electrons diffuse from the hot side of the sample to the cold side. Quite surprisingly, Group 11 metals have a positive S at all temperatures [151]. The RTA fails badly in these systems (as it always predicts a sign for S equal to that of the carriers) and the explanation of this puzzling behaviour is still missing and necessarily requires the exact solution of the BE.

As this work focused mainly on metallic and covalent systems, it will be interesting to extend its scope to polar materials. This is a particularly important step because, for instance, good thermoelectrics are often polar compounds and usually heavily doped. These features may introduce additional important scattering mechanisms that have not been considered in this work: the polar character may give rise to macroscopic electric fields (due to the lattice vibration of the polar LO phonons) that can couple to electrons (Fröhlich interaction), while large carrier concentrations may lead to screening effects and even plasmon oscillations that can also affect carrier transport. It is already possible to deal efficiently with Fröhlich corrections to the EPC within a Wannier function representation (this is part of the latest implementation of the `EPW` package [67]), and it will be interesting to test this new development on standard and well-characterized polar semiconductors such as GaAs. Screening effects can be added starting with phenomenological models and building on all

the modelling work done in the semiconductor physics community (see for instance Lowney and Bennett [152]).

Appendix A

Deriving the BE from the BBGKY hierarchy

In a system of N interacting particles, the value of observables will be determined by the system's collective state, defined by the N-body distribution function. According to the kinetic theory of gases, such an amount of information is not necessary and macroscopic quantities can be regarded as depending just on the single-particle distribution, that can be calculated from the N-body one. With the aid of the Liouville theorem, that governs the time evolution of the density function, it is possible to demonstrate that the dynamics of an N-body distribution function is determined by the one for $(N+1)$ bodies. This chain of equations is called the Bogoliubov-Born-Green-Kirkwood-Yvon (BBGKY) hierarchy,

$$\frac{\partial f_s}{\partial t} - \{\mathscr{H}_s, f_s\} = \sum_{n=1}^{s} \int d_3 p_{s+1} d_3 q_{s+1} \Big[\nabla_{\boldsymbol{q}_n} U(\boldsymbol{q}_n - \boldsymbol{q}_{s+1}) \cdot \nabla_{\boldsymbol{q}_n} f_{s+1}\Big], \tag{A.1}$$

where $\{,\}$ are the Poisson brackets. Defining the Hamiltonian to be,

$$\mathscr{H} = \sum_{n=1}^{s} (\frac{p_n^2}{2m} + V_n) + \frac{1}{2} \sum_{n,m=1}^{s} U_{nm}, \tag{A.2}$$

the first two equations of the hierarchy are,

$$\Big(\frac{\partial}{\partial t}+\frac{\boldsymbol{p}_1}{m}\cdot\nabla_{\boldsymbol{q}_1}+\boldsymbol{F}_1\cdot\nabla_{\boldsymbol{p}_1}\Big)f_1(\boldsymbol{p}_1,\boldsymbol{q}_1;t)= \tag{A.3a}$$

$$=-\int d_3p_2d_3q_2\boldsymbol{I}_{12}\cdot\nabla_{\boldsymbol{p}_1}f_2(\boldsymbol{p}_1,\boldsymbol{q}_1;\boldsymbol{p}_2,\boldsymbol{q}_2;t),$$

$$\Big[\frac{\partial}{\partial t}+\frac{\boldsymbol{p}_1}{m}\cdot\nabla_{\boldsymbol{q}_1}+\frac{\boldsymbol{p}_2}{m}\cdot\nabla_{\boldsymbol{q}_2}+\boldsymbol{F}_1\cdot\nabla_{\boldsymbol{p}_1}+\boldsymbol{F}_2\cdot\nabla_{\boldsymbol{p}_2}+\frac{1}{2}\boldsymbol{I}_{12}\cdot(\nabla_{\boldsymbol{p}_1}-\nabla_{\boldsymbol{p}_2})\Big] \tag{A.3b}$$

$$f_2(\boldsymbol{p}_1,\boldsymbol{q}_1,\boldsymbol{p}_2,\boldsymbol{q}_2;t)=-\int d_3p_3d_3q_3(\boldsymbol{I}_{13}\cdot\nabla_{\boldsymbol{p}_1}+\boldsymbol{I}_{23}\cdot\nabla_{\boldsymbol{p}_2})f_3(\boldsymbol{p}_1,\boldsymbol{q}_1;\boldsymbol{p}_2,\boldsymbol{q}_2;\boldsymbol{p}_3,\boldsymbol{q}_3;t), \tag{A.3c}$$

with $\boldsymbol{F}_i=-\nabla_{\boldsymbol{q}_i}V(\boldsymbol{q}_i)$ being the force exerted on the i-th particle by the external field V, $\boldsymbol{I}_{ij}=-\nabla_{\boldsymbol{q}_i}U(|\boldsymbol{q}_i-\boldsymbol{q}_j|)$ the interaction force between the i-th and j-th particles and f_N the N-bodies distribution function.

All the terms that are coupled with the distribution functions have the dimension of the inverse of a time and through dimensional analysis it is possible to give and estimate of their average order of magnitude. We can start considering the term $\frac{\boldsymbol{p}}{m}\cdot\nabla_{\boldsymbol{q}}\sim\frac{1}{\tau_d}$, that suggest a typical time in which the variation of the distribution function occurs due to particles' free diffusion. Then, there is $\boldsymbol{F}\cdot\nabla_{\boldsymbol{p}}\sim\frac{1}{\tau_f}$ that refers to the time in which the change of the distribution happens due to the action of the external fields. Another typical time is set by $\boldsymbol{U}\cdot\nabla_{\boldsymbol{p}}\sim\frac{1}{\tau_i}$, that regards variations due to an interaction with another particle. Finally, there is the time scale of the integral on the r.h.s. of the Eq.s A.1, that is related to the diffusion of particles due to the collision with all the other one present within the typical interaction range, that will be called τ_c.

The time τ_c is proportional to the time scale set by two-body interaction but involves also the integrated density of the additional scattering particles in the relevant interaction neighborhood. For short-ranged couplings, this gives rise to a factor of the order of the number of colliding bodies so that $\frac{\tau_i}{\tau_c}\sim nl^3\ll 1$, in the case of diluted, weakly interacting gas, where n is the average density of particles and l is the typical interaction length. Amongst the first three time scales, considering some experimental observation, it is possible to argue that τ_i is again the smaller one. This lead to the conclusion that the most prominent contribution to the Eq.s A.1 comes from the terms linked with τ_i, providing a criterion for the truncation of the BBGKY hierarchy.

Upon a closer inspection, it is possible to notice that the first Eq. A.3, in contrast to all the other ones, isn't provided with a $\boldsymbol{U}\cdot\nabla_{\boldsymbol{p}}$ term on its left-hand side. Physically, this means that the variations of the one-body distribution take place on a slower time scale with respect

to the other distributions; from this observation it is reasonable to suppose that *the lowest order contribution to macroscopic observables comes from the 1-body distribution function*. This conclusion gives a semi-quantitative explanation of the validity of the kinetic theory of gases. It is thus reasonable to neglect the collision integral of Eq. A.3c to disentangle the first two order distribution functions from the higher order ones.

To obtain the most common form of the Boltzmann transport equation for gases with two-body interactions from Eq. A.3, just few more elements are needed. The most important one is the assumption introduced by Boltzmann of *molecular chaos*. Formally, this results in the factorization of the 2-body distribution function in a product of 1-body distributions $f_2(\boldsymbol{p}_1,\boldsymbol{q}_1;\boldsymbol{p}_2,\boldsymbol{q}_2;t) \sim f_1(\boldsymbol{p}_1,\boldsymbol{q}_1;t) f_1(\boldsymbol{p}_2,\boldsymbol{q}_2;t)$, so that Eq. A.3 has now a closed form. This statement accounts for the observation that the correlations between two particles that are more apart than several interaction radii are negligible due, for example, to the effect of external perturbations and additional collisions. However, 2-body correlations are implicitly added to the steady state distribution function, which is solution of the BTE, by the differential operator in the r.h.s., that takes interactions into account, so that the physics of the equation is still sound. More details are discussed, in the case of classical, two-body collision, in the Ref. [72].

Appendix B

Deformation potential models in Silicon

In Ref. 61, transition probabilities are calculated with the Fermi golden rule employing deformation potentials. The phonon modes that are relevant in transport are the ones that bridge the six energy pockets of Silicon. In the temperature and doping concentration regimes that are considered, the electronic states for which transitions are allowed occupy a rather localized volume of the Brillouin zone, compared to the variation of the phonon dispersion relation. As a consequence, only nine scattering channels are effectively considered in this model. EPC and phonon dispersions are approximated with the average values of the modes that bridge the six Silicon valleys at the minimum of the conduction band.

For acoustic phonons, that are responsible for intra-valley scattering processes, the transition probability is calculated in the elastic approximation and by counting the density of phonons in the samples by energy equipartition. This choice is ustified recalling the limited extension in the BZ of the pockets and the fact that acoustic phonon dispersion at Γ is vanishing. The formula, that takes into account both processes involving emission and absorption of phonons, is the following,

$$P_{\mathbf{k}\mathbf{k}'} = \frac{2\pi k_B T}{\hbar V u_s^2 \rho_c} \mathscr{E}^2 \mathscr{G} \delta[\varepsilon(\mathbf{k}') - \varepsilon(\mathbf{k})]. \tag{B.1}$$

In the expression above, V is the volume of the primitive cell, v is the modulus of the sound speed averaged in along the one lungitudinal and two transversal directions, ρ_c is the density of the material and $\mathscr{E}$ is the coupling constant, that I will be fitting from first principles.

In the case of inter-valley scattering, it is possible to distinguish between f-processes, that take places between orthogonal valleys and g-processes, that happen amidst parallel valleys (see discussion in Sec. 6.2.1 for a detailed definition). The main difference between f- and g- processes is the average distance in the BZ that joins the valleys, resulting in different

Intra valley		
Mode	Coupling c. $\mathscr{E}$ [eV]	Sound speed [$/s$]
TA_1	2.9652	4.8998E+13
TA_2	1.2200	5.4512E+13
LA	5.0979	8.638479E+13

Table B.1 Intra valley phonon modes parameters from first-principles.

Inter valley			
	Mode	Coupling c. $\mathscr{D}$ [eV/]	Energy [eV]
f	TA_1	0.1287	0.01847
	TA_2	0.086	0.002264
	LA	1.6552	0.04612
	LO	1.8941	0.04827
	TO_1	0.08588	0.05663
	TO_2	3.98	0.05755
g	TA_1	0.14378	0.0111
	TA_2	0.40362	0.01155
	LA	0.3667	0.01905
	TO_1	0.2612	0.0604
	TO_2	0.1515	0.0605
	LO	4.57	0.06192

Table B.2 Inter-valley phonon modes parameters from first principles.

averages $\boldsymbol{q}$ phonon wave vectors; this determines the typical values of the constant phonon energy and of the coupling constant that will be used to fit the deformation potentials. The probability formula becomes,

$$P_{\mathbf{k}\mathbf{k}'} = \frac{\pi}{\rho V \omega_{ph}} D^2 \mathscr{G} \left\{ \begin{array}{c} N \\ N+1 \end{array} \right\} \delta\left\{\varepsilon(\mathbf{k}') - [\varepsilon(\mathbf{k}) \pm \hbar\omega_{ph}]\right\}, \tag{B.2}$$

where ω_{ph} is the phonon angular frequency, and D is the coupling constant.

To reproduce Silicon's phenomenology, the parameters that fit these formulas have been calculated from first principles in the past for inter-valley processes [62], thus providing ground to check our first-principles methods. Interestingly, intra-valley parameters are often empirical [117], and are choosen to best fit experimental data in the near-intrinsic transport regime (doping concentration $\leq 10^{15} cm^{-3}$). With my first-principlea approach via Eq. 2.33 EPC constants can be fitted. There results of the calculations are listed below:

Comparing the full ab-initio transport results for $\mu_e(n_i)$ with the values obtained with the ones obtained with the deformation potential fitted with the parameters in Tab.s B.1, B.2, I am able to confirm that deformation potential provides an accurate approximation to the transition probability due to EPC in silicon, a statement that can be also extended to covalent materials.

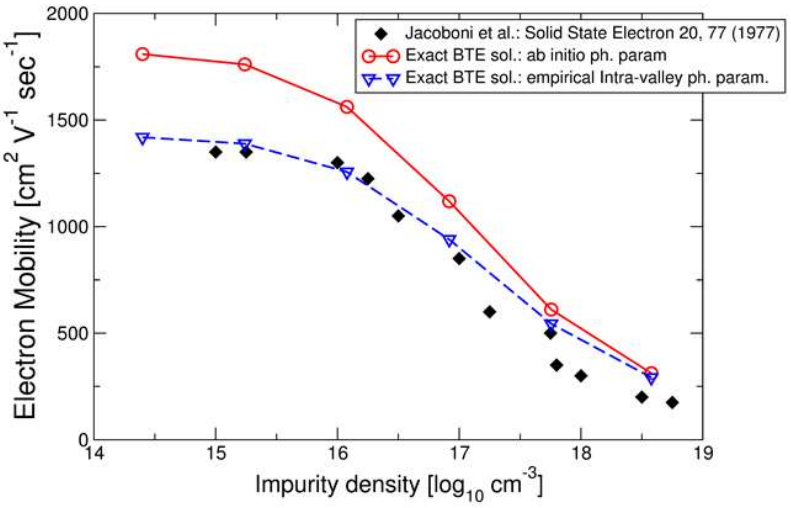

Fig. B.1 Electron mobility against donor concentration at $T = 300K$. Electron-phonon coupling has been modeled using deformation potentials. Red line obtained using the parameters fitted with our calculations as in the Tab.s B.1 and B.2, blue dashed line with paramters in [61]. The main difference in the two curves at low doping is due to an overestimation of the coupling constant of the LA intra-valley modes of the DFT in LDA calculations.

With the aid of these models, we can pinpoint the reason of the overestimation of the mobility in the intrinsic regime. Of the parameter provided in Tab.s B.1 and B.2, the first-principles, averaged phonon energies are in agreement with both previous ab-initio calculations[117] and empirical estimations [61]. Comparing the inter-valley coupling constants with the one available in the literature[117], we verified that their impact on the mobility is small, obtaining very similar results (not shown) with both sets of parameters. I was able to reproduce the experiental intrinsic mobility value by tuning the coupling constant $\mathscr{E}$ of the transition induced by the intra-valley LA mode to empirical values reported in Re. 61. This suggest that the DFT in LDA aproach could underestimate EPC in Si. This observation has been reported also for other sp-bonded systems, such as graphene[123] and diamond[124].

Appendix C

Numerical parameters and convergence

To compute the electronic and vibrational properties including the EPCM elements this work employed DFT and DFPT as implemented in the `Quantum-ESPRESSO` distribution[58] within the LDA[44]. Then $\varepsilon_{m\boldsymbol{k}}$, $\boldsymbol{v}_{m\boldsymbol{k}}$, $\hbar\omega_\lambda$ and $g^{\lambda}_{mm'}(\boldsymbol{k};\boldsymbol{q})$ were calculated on finer grids using the first-principles interpolation scheme[66] based on maximally localized Wannier functions,[63] as implemented in the `Wannier90`[65] and `EPW`[67].

C.1 Metals

C.1.1 Aluminium

The SCF calculation was carried out using a norm-conserving pseudopotential and a plane-wave expansion up to 25 Ry. BZ was sampled using a $8 \times 8 \times 8$ Monkhorst-Pack mesh for both electron and phonons. An 0.03Ry Marzari-Vanderbilt smearing was used to compute charge density. The Wannier interpolation was done on $8 \times 8 \times 8$ k-point mesh using 9 Wannier functions. EPC was stored on a coarse grid of 40^3 k-points . $\varepsilon_m(\boldsymbol{k})$, $\boldsymbol{v}_m(\boldsymbol{k})$, $\hbar\omega_\lambda(\boldsymbol{q})$, and the transition probabilities were calculated on a grid of $(2 \times 40)^3$. The transport-relevant region of the BZ was selected in an energy window of ± 0.07 eV from μ. The gaussian spread was set at 0.01eV.

C.1.2 Copper

The SCF calculation employed a norm-conserving pseudopotential on a PW basis of up to 80Ry. The BZ was sampled on a $16 \times 16 \times 16$ and $5 \times 5 \times 5$ Monkhorst-Pack meshes for electrons and phonons, respectively. Charge density was computed with a 0.02Ry Marzari-

Vanderbilt smearing. Wannier interpolation was carried out on a $10 \times 10 \times 10$ k-point mesh using a basis of 7 Wannier functions. EPC was stored on a coarse grid of 45^3 k-points. $\varepsilon_m(\boldsymbol{k})$, $\boldsymbol{v}_m(\boldsymbol{k})$, $\hbar\omega_\lambda(\boldsymbol{q})$, and the transition probabilities were calculated on a fine grid of $(2 \times 45)^3$. The transport-relevant region of the BZ was selected in an energy window of ± 0.07eV from μ. The gaussian spread was set at 0.01eV.

C.2 Silicon

To calculate V_{SCF}, I used a norm-conserving pseudopotential and a plane-wave expansion up to a 30Ry cutoff. Brillouin-zone sampling was performed on $12 \times 12 \times 12$ Monkhorst-Pack mesh for all charge density and phonon calculations. I used a theoretical lattice parameter of 5.41 Å. To get $\varepsilon_m(\boldsymbol{k})$, $\boldsymbol{v}_m(\boldsymbol{k})$, and $g^\lambda_{mm'}(\boldsymbol{k};\boldsymbol{q})$ in Wannier representation, I started from $10 \times 10 \times 10$ k-points and $5 \times 5 \times 5$ q-points. Then I have used Wannier interpolation to compute transport quantities on very dense meshes up to $110 \times 110 \times 110$.

I have adopted the double grid scheme discussed in Sec. 4.2, in which the EPC matrix elements are stored on a coarse mesh in reciprocal space ($N_{\mathrm{EPC}} \times N_{\mathrm{EPC}} \times N_{\mathrm{EPC}}$) with $N_{\mathrm{EPC}} = 70$, and an ultra fine grid ($N_f \times N_f \times N_f$, with $N_f = p \cdot N_{\mathrm{EPC}}$ and $p = 3$) is used to calculate, $\varepsilon_m(\boldsymbol{k})$, $\boldsymbol{v}_m(\boldsymbol{k})$, and $g^\lambda_{mm'}(\boldsymbol{k};\boldsymbol{q})$, solve the BE, and compute the transport quantities. The delta functions in the transition probabilities are replaced with gaussians having $\sigma = 4$ meV.

The anharmonic phonon lifetimes needed to compute the contribution of the phonon drag to the transport coefficients were computed within the single mode relaxation time approximation and from the third order force constants used in Ref. 91. In this work I have recalculated the lifetimes on a $(70 \times 70 \times 70)$ mesh of q-points using a gaussian width of 2 cm^{-1}.

C.2.1 Convergence of transport quantities

Here I discuss the choice of the numerical parameters used to compute transport coefficients. These parameters are i) the mesh $N_{\mathrm{EPC}} \times N_{\mathrm{EPC}} \times N_{\mathrm{EPC}}$ of k-points on which I compute the electron-phonon coupling matrix elements, ii) the fine grid $N_f \times N_f \times N_f$ (where I use $N_f = p \cdot N_{\mathrm{EPC}}$, with $p = 1$, 2 and 3) used to solve the BE and compute the transport quantities, iii) the energy window from the bottom of the conduction band used to restrict the number of k-points, iv) the standard deviation σ_g of the gaussians used to replace the delta functions in the transition probabilities.

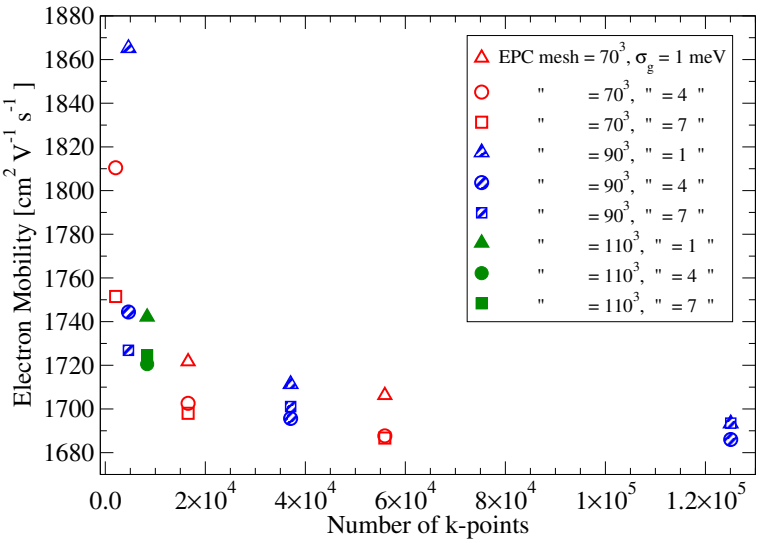

Fig. C.1 Electron mobility at room temperature and for $n = 1.6 \times 10^{15}\text{cm}^{-3}$ as function of number of k-points used to solve the BE. Different electron-phonon coupling grids are used: $N_{\text{EPC}} = 70$ (red empty symbols), $N_{\text{EPC}} = 90$ (blu patterned symbols) and $N_{\text{EPC}} = 110$ (green full symbols). The values of σ_g used are 1 meV (triangles), 4 meV (circles) and 7 meV (squares). The results obtained with less (more) than 10^4 (5×10^4) k-points on the x-axis are for $p = 1$ ($p = 3$); the remainig points are for $p = 2$. The energy window used is 0.15 eV.

In Fig. C.1 I present the electron mobility as a function of the number of k-points used to solve the BE. The different symbols correspond to different values for N_{EPC}, p, and σ_g. My results shows that even with a $N_{\text{EPC}} = 110$ and $p = 1$ (that is very computationally demanding) the convergence is not yet fully achieved. However, increasing the effective mesh with $p = 2$ and $p = 3$ gives stable mobilities, even when starting from different N_{EPC} (i.e. $N_{\text{EPC}} = 70, 90$), which implies that the electron-phonon matrices are accurately sampled already with these mashes.

The choice of the energy window to select the states relevant for transport depends on the thermoelectric transport coefficients under consideration. While a window of 0.15 eV is sufficient to obtain converged results for the electron mobility[1], other coefficients require a larger window. For instance, Fig. 6.11 clearly shows that the accurate evaluation of the Seebeck coefficient requires an energy window considerably smaller than the one needed to compute the Lorenz number. In addition, the energy window might also depend slightly on the relevant scattering mechanisms. It is possible to see this for the Lorenz number [2]: when only impurity scattering is considered there is large contribution from electronic states

[1] This energy window includes also the contribution of the second conduction band that starts around 0.13 eV.

[2] L is much more sensitive than S to the scattering mechanisms included in the BE, as discussed in Sec. 6.2.4

quite far from the bottom of the conduction band and the energy window required for the convergence is slightly larger than in the case in which only phonon scattering is included.

C.2.2 Performance and accuracy of the BE solver

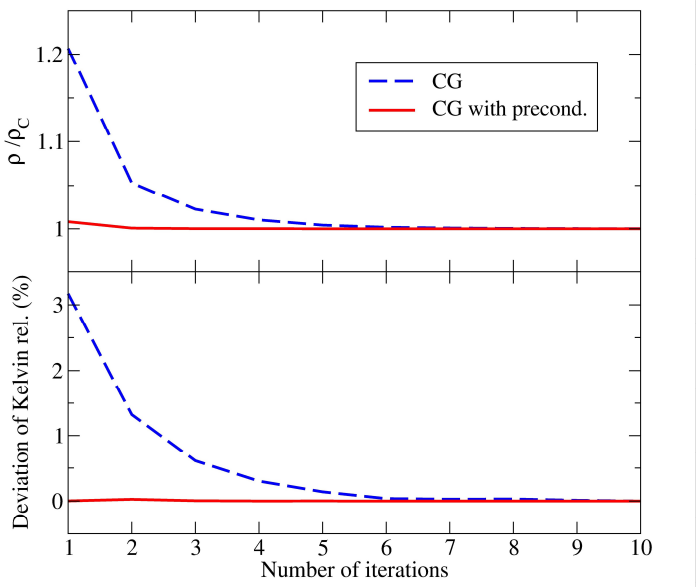

Fig. C.2 Performance of the CG algorithm. Upper panel: resistivity (normalised to the converged result ρ_C) as a function of the number of iterations. Lower panel: Deviation from the Kelvin relation as a function of the number of iterations. The dashed blue (solid red) line is the result of the CG (with reconditioning). The results are for $n = 1.75 \times 10^{14}$ cm^{-3}, T=300 K and with phonons in thermal equilibrium.

The implementation of the LBE solver has been discussed in Sec. 4.4. The performance of the algorithm is shown in Fig. C.2: the plain CG converges in 6 or 7 iterations, while the preconditioned version meets the convergence threshold in 2-3 iterations. In my experience standard iterative approaches[35] converge very slowly, especially in the presence of charged impurity scattering.

In order to assess the accuracy of the solution of the BE, it is interesting to numerically verify the validity of the Kelvin relation Eq. 3.18 without phonon drag. The lower panel of Fig. C.2 shows that, when phonons are in thermal equilibrium, the converged solutions of the BE's with temperature gradient and electric field as driving forces satisfy the Kelvin relation; the CG algorithm with preconditioning reaches the converged result very quickly.

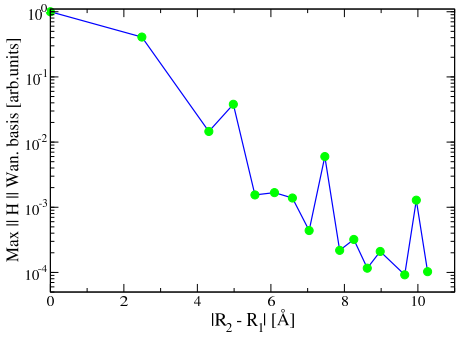

(a) Max $||\mathscr{H}(\boldsymbol{R})||$

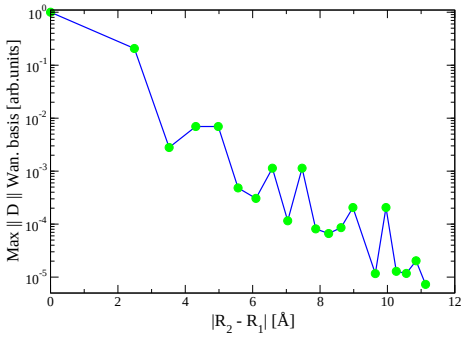

(b) Max $||\mathscr{D}(\boldsymbol{R})||$

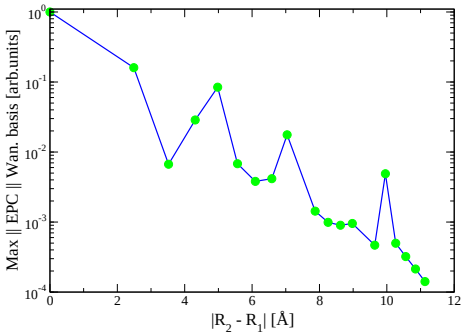

(c) Max $||EPC(\boldsymbol{R})||$

Fig. C.3 Spatial decay of the $\mathscr{H}$ (a), $\mathscr{D}$ (b) and $\left\langle \nu'\mathbf{0} \middle| \partial_{\gamma \boldsymbol{R}''} V_{SCF} \middle| \nu \boldsymbol{R} \right\rangle$ (c) in the MLWF basis. Data have been normalized to the largest value, which occurs when the absolute value of the distance is zero $|\boldsymbol{R}| = 0$. It is possible to appreciate an exponential decay in the distance $\boldsymbol{R}$.

C.3 Diamond

The initial DFT calculation was performed on $8 \times 8 \times 8$ Monkorst-Pack mesh with a PW cutoff of 30 Ry. To obtain the electron and vibrational properties of the system, and the EPC on the 7 WF basis, I started from $10 \times 10 \times 10$ k- and q- point grids. Wannier interpolation was used to store EPC on a 60^3 k-point grid. All the other transport quantities, including transition probabilities were calculated using a fine grid, according to the multi-mesh scheme describe in Sec. 4.2 on a $(3 \times 60)^3$ k-point grid. The relevant relevant transport region was selected within 0.1 eV from the top of the valence band. The gaussian spread use was of 5meV.

In Pic. C.3 it is shown the spatial decay of the relevan operators, $\mathscr{H}$ (a), $\mathscr{D}$ (b) and $\left\langle \nu'\mathbf{0} \middle| \partial_{\gamma \boldsymbol{R}''} V_{SCF} \middle| \nu \boldsymbol{R} \right\rangle$ (c) in the MLWF basis obtained using `wannier90`. It is possible to

see that the upper bound of the matrix element in each spatial direction decays exponentially with the distance.

References

[1] European Commission. Horizon 2020: Societal challenges - secure, clean and efficient energy, Sept 2014. URL http://cordis.europa.eu/programme/rcn/664321_en.html.

[2] Jason Baxter, Zhixi Bian, Gang Chen, David Danielson, Mildred S. Dresselhaus, Andrei G. Fedorov, Timothy S. Fisher, Christopher W. Jones, Edward Maginn, Uwe Kortshagen, Arumugam Manthiram, Arthur Nozik, Debra R. Rolison, Timothy Sands, Li Shi, David Sholl, and Yiying Wu. Nanoscale design to enable the revolution in renewable energy. *Energy Environ. Sci.*, 2:559–588, 2009. URL http://dx.doi.org/10.1039/B821698C.

[3] Eric Pop. Energy dissipation and transport in nanoscale devices. *Nano Research*, 3(3): 147–169, 2010. URL http://dx.doi.org/10.1007/s12274-010-1019-z.

[4] K. Shenai, R. S. Scott, and B. J. Baliga. Optimum semiconductors for high-power electronics. *IEEE Transactions on Electron Devices*, 36(9):1811–1823, Sep 1989.

[5] Chris J.H. Wort and Richard S. Balmer. Diamond as an electronic material. *Materials Today*, 11(1–2):22 – 28, 2008. URL http://www.sciencedirect.com/science/article/pii/S1369702107703498.

[6] A. J. Minnich, M. S. Dresselhaus, Z. F. Ren, and G. Chen. Bulk nanostructured thermoelectric materials: current research and future prospects. *Energy Environ. Sci.*, 2:466–479, 2009. URL http://dx.doi.org/10.1039/B822664B.

[7] Lon E. Bell. Cooling, heating, generating power, and recovering waste heat with thermoelectric systems. *Science*, 321(5895):1457–1461, 2008. URL http://science.sciencemag.org/content/321/5895/1457.

[8] G. Jeffrey Snyder and Eric S. Toberer. Complex thermoelectric materials. *Nature Materials*, 7(2):105–114, 2008/02. URL http://dx.doi.org/10.1038/nmat2090.

[9] S.B Riffat and Xiaoli Ma. Thermoelectrics: a review of present and potential applications. *Applied Thermal Engineering*, 23(8):913 – 935, 2003. URL http://www.sciencedirect.com/science/article/pii/S1359431103000127.

[10] C. Goupil. *Continuum Theory and Modeling of Thermoelectric Elements*. Wiley, 2016. ISBN 9783527413379. URL https://books.google.co.uk/books?id=XQemCgAAQBAJ.

[11] J. Yang. In *24th International Conference on Thermoelectrics*, pages 170–174, 2005.

[12] D.M. Rowe. Thermoelectrics, an environmentally-friendly source of electrical power. *Renewable Energy*, 16(1):1251 – 1256, 1999. URL http://www.sciencedirect.com/science/article/pii/S0960148198005126.

[13] G D Mahan and J O Sofo. The best thermoelectric. *Proceedings of the National Academy of Sciences*, 93(15):7436–7439, 1996. URL http://www.pnas.org/content/93/15/7436.abstract.

[14] Yucheng Lan, Austin Jerome Minnich, Gang Chen, and Zhifeng Ren. Enhancement of thermoelectric figure-of-merit by a bulk nanostructuring approach. *Advanced Functional Materials*, 20(3):357–376, 2010. URL http://dx.doi.org/10.1002/adfm.200901512.

[15] A.F. Ioffe. *Semiconductor thermoelements, and Thermoelectric cooling*. Infosearch, ltd., 1957. URL https://books.google.co.uk/books?id=i_FSAAAAMAAJ.

[16] Werner Haken. Beitrag zur kenntnis der thermoelektrischen eigenschaften der metallegierungen. *Annalen der Physik*, 337(7):291–336, 1910. URL http://dx.doi.org/10.1002/andp.19103370704.

[17] Paothep Pichanusakorn and Prabhakar Bandaru. Nanostructured thermoelectrics. *MATERIALS SCIENCE & ENGINEERING R-REPORTS*, 67(2-4):19–63, JAN 29 2010. doi: 10.1016/j.mser.2009.10.001.

[18] A.F. Ioffe. *Physics of Semiconductors*. Academic Press, 1960.

[19] L. D. Hicks and M. S. Dresselhaus. Effect of quantum-well structures on the thermoelectric figure of merit. *Phys. Rev. B*, 47:12727–12731, May 1993. URL http://link.aps.org/doi/10.1103/PhysRevB.47.12727.

[20] L. D. Hicks and M. S. Dresselhaus. Thermoelectric figure of merit of a one-dimensional conductor. *Phys. Rev. B*, 47:16631–16634, Jun 1993. URL http://link.aps.org/doi/10.1103/PhysRevB.47.16631.

[21] G. A. Slack. *New materials and performance limits for thermoelectric cooling*, pages 407–440. CRC Press, 1995. ISBN 9780849301469.

[22] Yanzhong Pei, Heng Wang, and G. J. Snyder. Band engineering of thermoelectric materials. *Advanced Materials*, 24(46):6125–6135, 2012. URL http://dx.doi.org/10.1002/adma.201202919.

[23] Joseph R. Sootsman, Duck Young Chung, and Mercouri G. Kanatzidis. New and old concepts in thermoelectric materials. *Angewandte Chemie International Edition*, 48 (46):8616–8639, 2009. URL http://dx.doi.org/10.1002/anie.200900598.

[24] M. Zebarjadi, K. Esfarjani, M. S. Dresselhaus, Z. F. Ren, and G. Chen. Perspectives on thermoelectrics: from fundamentals to device applications. *Energy Environ. Sci.*, 5:5147–5162, 2012. doi: 10.1039/C1EE02497C. URL http://dx.doi.org/10.1039/C1EE02497C.

[25] D. A. Broido, M. Malorny, G. Birner, Natalio Mingo, and D. A. Stewart. Intrinsic lattice thermal conductivity of semiconductors from first principles. *Applied Physics Letters*, 91(23):231922, 2007. URL http://scitation.aip.org/content/aip/journal/apl/91/23/10.1063/1.2822891.

[26] Jivtesh Garg, Nicola Bonini, Boris Kozinsky, and Nicola Marzari. Role of disorder and anharmonicity in the thermal conductivity of silicon-germanium alloys: A first-principles study. *Phys. Rev. Lett.*, 106:045901, Jan 2011. URL http://dx.doi.org/10.1103/PhysRevLett.106.045901.

[27] Jiawei Zhou, Bolin Liao, Bo Qiu, Samuel Huberman, Keivan Esfarjani, Mildred S. Dresselhaus, and Gang Chen. Ab initio optimization of phonon drag effect for lower-temperature thermoelectric energy conversion. *Proceedings of the National Academy of Sciences*, 112(48):14777–14782, 2015. URL http://www.pnas.org/content/112/48/14777.abstract.

[28] Wu Li. Electrical transport limited by electron-phonon coupling from boltzmann transport equation: An *ab initio* study of si, al, and mos_2. *Phys. Rev. B*, 92:075405, Aug 2015. URL http://link.aps.org/doi/10.1103/PhysRevB.92.075405.

[29] Georg K.H. Madsen and David J. Singh. Boltztrap. a code for calculating band-structure dependent quantities. *Computer Physics Communications*, 175(1):67 – 71, 2006. URL http://www.sciencedirect.com/science/article/pii/S0010465506001305.

[30] Giovanni Pizzi, Dmitri Volja, Boris Kozinsky, Marco Fornari, and Nicola Marzari. Boltzwann: A code for the evaluation of thermoelectric and electronic transport properties with a maximally-localized wannier functions basis. *Computer Physics Communications*, 185(1):422 – 429, 2014. URL http://www.sciencedirect.com/science/article/pii/S0010465513003160.

[31] L. D. Landau. On the theory of fermi liquid. *JETP*, 8:70–74, January 1959.

[32] Richard E. Prange and Leo P. Kadanoff. Transport theory for electron-phonon interactions in metals. *Phys. Rev.*, 134:A566–A580, May 1964. URL http://link.aps.org/doi/10.1103/PhysRev.134.A566.

[33] Václav Špička and Pavel Lipavský. Quasiparticle boltzmann equation in semiconductors. *Phys. Rev. B*, 52:14615–14635, Nov 1995. URL http://link.aps.org/doi/10.1103/PhysRevB.52.14615.

[34] H. Mitter. Recent applications of boltzmann's theory. In H. Mitter, E. Schachinger, and H. Sormann, editors, *Recent Progress in Many-Body Theories*, number v. 4, chapter 2, pages 9–21. Springer US, 1995. ISBN 9780306451034.

[35] F. X. Bronold. Boltzmann transport in condensed matter. In H. Fehske, R. Schneider, and A. Weiße, editors, *Computational Many-Particle Physics*, Lecture Notes in Physics, chapter 8, pages 223–254. Springer Berlin Heidelberg, 2007. ISBN 9783540746850.

[36] N.W. Ashcroft and N.D. Mermin. *Solid state physics*. Science: Physics. Saunders College, 1976. ISBN 9780030493461.

[37] R.M. Martin. *Electronic Structure: Basic Theory and Practical Methods*. Cambridge University Press, 2004.

[38] P. Hohenberg and W. Kohn. Inhomogeneous electron gas. *Phys. Rev.*, 136:B864–B871, Nov 1964. URL http://link.aps.org/doi/10.1103/PhysRev.136.B864.

[39] Klaus Capelle. A bird's-eye view of density-functional theory. *Brazilian Journal of Physics*, 36:1318 – 1343, 12 2006. URL http://www.scielo.br/scielo.php?script=sci_arttext&pid=S0103-97332006000700035&nrm=iso.

[40] W. Kohn and L. J. Sham. Self-consistent equations including exchange and correlation effects. *Phys. Rev.*, 140:A1133–A1138, Nov 1965. URL http://link.aps.org/doi/10.1103/PhysRev.140.A1133.

[41] L. H. Thomas. The calculation of atomic fields. *Mathematical Proceedings of the Cambridge Philosophical Society*, 23:542–548, 1 1927. URL http://journals.cambridge.org/article_S0305004100011683.

[42] E. Fermi. Un metodo statistico per la determinazione di alcune proprietà del'atomo. *Rend. Accad. Naz. Lincei*, 6:602–607, 1927.

[43] Stefano Baroni, Stefano de Gironcoli, Andrea Dal Corso, and Paolo Giannozzi. Phonons and related crystal properties from density-functional perturbation theory. *Rev. Mod. Phys.*, 73:515–562, Jul 2001. URL http://link.aps.org/doi/10.1103/RevModPhys.73.515.

[44] J. P. Perdew and Alex Zunger. Self-interaction correction to density-functional approximations for many-electron systems. *Phys. Rev. B*, 23:5048–5079, May 1981. URL http://link.aps.org/doi/10.1103/PhysRevB.23.5048.

[45] A.L. Fetter and J.D. Walecka. *Quantum Theory of Many-particle Systems*. Dover Books on Physics. Dover Publications, 2003. ISBN 9780486428277.

[46] Giovanni Onida, Lucia Reining, and Angel Rubio. Electronic excitations: density-functional versus many-body green's-function approaches. *Rev. Mod. Phys.*, 74:601–659, Jun 2002. URL http://link.aps.org/doi/10.1103/RevModPhys.74.601.

[47] E.K.U. Gross, E. Runge, and O. Heinonen. *Many-Particle Theory,*. Taylor & Francis, 1991. ISBN 9780750301558.

[48] Lars Hedin. New method for calculating the one-particle green's function with application to the electron-gas problem. *Phys. Rev.*, 139:A796–A823, Aug 1965. doi: 10.1103/PhysRev.139.A796. URL https://link.aps.org/doi/10.1103/PhysRev.139.A796.

[49] M. van Schilfgaarde, Takao Kotani, and S. Faleev. Quasiparticle self-consistent *gw* theory. *Phys. Rev. Lett.*, 96:226402, Jun 2006. URL http://link.aps.org/doi/10.1103/PhysRevLett.96.226402.

[50] M. Born and R. Oppenheimer. Zur quantentheorie der molekeln. *Annalen der Physik*, 389(20):457–484, 1927. URL http://dx.doi.org/10.1002/andp.19273892002.

[51] G. Grimvall. *The electron-phonon interaction in metals*. Selected topics in solid state physics. North-Holland Pub. Co. : sole distributors for the U.S.A. and Canada, Elsevier North-Holland, 1981. ISBN 9780444861054.

[52] G V Chester and A Houghton. Electron-phonon interaction in metals i: The harmonic approximation. *Proceedings of the Physical Society*, 73(4):609, 1959. URL http://stacks.iop.org/0370-1328/73/i=4/a=310.

[53] H. Hellmann. Einführung in die quantenchemie. von h. hellmann. 350 s.,43 abb., 35 tab. franz deuticke, leipzig u. wien 1937. pr. geh. rm. 20,-. geb. rm. 22,-. *Angewandte Chemie*, 54(11-12):156–156, 1941. URL http://dx.doi.org/10.1002/ange.19410541109.

[54] R. P. Feynman. Forces in molecules. *Phys. Rev.*, 56:340–343, Aug 1939. URL http://link.aps.org/doi/10.1103/PhysRev.56.340.

[55] Pui K. Lam and Marvin L. Cohen. *Ab initio* calculation of phonon frequencies of al. *Phys. Rev. B*, 25:6139–6145, May 1982. URL http://link.aps.org/doi/10.1103/PhysRevB.25.6139.

[56] Stefano Baroni, Paolo Giannozzi, and Andrea Testa. Green's-function approach to linear response in solids. *Phys. Rev. Lett.*, 58:1861–1864, May 1987. URL http://link.aps.org/doi/10.1103/PhysRevLett.58.1861.

[57] Xavier Gonze. Adiabatic density-functional perturbation theory. *Phys. Rev. A*, 52:1096–1114, Aug 1995. URL http://link.aps.org/doi/10.1103/PhysRevA.52.1096.

[58] Paolo Giannozzi, Stefano Baroni, Nicola Bonini, Matteo Calandra, Roberto Car, Carlo Cavazzoni, Davide Ceresoli, fido L Chiarotti, Matteo Cococcioni, Ismaila Dabo, Andrea Dal Corso, Stefano de Gironcoli, Stefano Fabris, Guido Fratesi, Ralph Gebauer, Uwe Gerstmann, Christos Gougoussis, Anton Kokalj, Michele Lazzeri, Layla Martin-Samos, Nicola Marzari, Francesco Mauri, Riccardo Mazzarello, Stefano Paolini, Alfredo Pasquarello, Lorenzo Paulatto, Carlo Sbraccia, Sandro Scandolo, Gabriele Sclauzero, Ari P Seitsonen, Alexander Smogunov, Paolo Umari, and Renata M Wentzcovitch. Quantum espresso: a modular and open-source software project for quantum simulations of materials. *Journal of Physics: Condensed Matter*, 21(39):395502, 2009. URL http://stacks.iop.org/0953-8984/21/i=39/a=395502.

[59] J.J. Sakurai and J. Napolitano. *Modern Quantum Mechanics*. Addison-Wesley, 2011. ISBN 9780805382914.

[60] A. Piróth and J. Sólyom. *Fundamentals of the Physics of Solids: Volume II: Electronic Properties*. Fundamentals of the Physics of Solids. Springer Berlin Heidelberg, 2008. ISBN 9783540853152.

[61] Carlo Jacoboni and Lino Reggiani. The monte carlo method for the solution of charge transport in semiconductors with applications to covalent materials. *Rev. Mod. Phys.*, 55:645–705, Jul 1983. URL http://link.aps.org/doi/10.1103/RevModPhys.55.645.

[62] Valeriy Tyuterev, Jelena Sjakste, and Nathalie Vast. Theoretical intrinsic lifetime limit of shallow donor states in silicon. *Phys. Rev. B*, 81:245212, Jun 2010. URL http://link.aps.org/doi/10.1103/PhysRevB.81.245212.

[63] Nicola Marzari, Arash A. Mostofi, Jonathan R. Yates, Ivo Souza, and David Vanderbilt. Maximally localized wannier functions: Theory and applications. *Rev. Mod. Phys.*, 84:1419–1475, Oct 2012. URL http://link.aps.org/doi/10.1103/RevModPhys.84.1419.

[64] Nicola Marzari and David Vanderbilt. Maximally localized generalized wannier functions for composite energy bands. *Phys. Rev. B*, 56:12847–12865, Nov 1997. URL http://link.aps.org/doi/10.1103/PhysRevB.56.12847.

[65] Arash A. Mostofi, Jonathan R. Yates, Giovanni Pizzi, Young-Su Lee, Ivo Souza, David Vanderbilt, and Nicola Marzari. An updated version of wannier90: A tool for obtaining maximally-localised wannier functions. *Computer Physics Communications*, 185(8):2309 – 2310, 2014. URL http://www.sciencedirect.com/science/article/pii/S001046551400157X.

[66] Feliciano Giustino, Marvin L. Cohen, and Steven G. Louie. Electron-phonon interaction using wannier functions. *Phys. Rev. B*, 76:165108, Oct 2007. URL http://link.aps.org/doi/10.1103/PhysRevB.76.165108.

[67] Jesse Noffsinger, Feliciano Giustino, Brad D. Malone, Cheol-Hwan Park, Steven G. Louie, and Marvin L. Cohen. Epw: A program for calculating the electron–phonon coupling using maximally localized wannier functions. *Computer Physics Communications*, 181(12):2140 – 2148, 2010. URL http://www.sciencedirect.com/science/article/pii/S0010465510003218.

[68] W. Pauli. *Statistical Mechanics*. The MIT Press, 1973.

[69] L. M. Martyushev and V. D. Seleznev. *Phys. Rep.*, 426:1–45, 2006.

[70] J.M. Ziman. *Electrons and Phonons: The Theory of Transport Phenomena in Solids*. International series of monographs on physics. OUP Oxford, 1960. ISBN 9780198507796.

[71] José A. Manzanares, Miikka Jokinen, and Javier Cervera. On the different formalisms for the transport equations of thermoelectricity: A review. *Journal of Non-Equilibrium Thermodynamics*, 40:211–227, Jul 2015.

[72] K. Huang. *Statistical mechanics*. Wiley, 1987. ISBN 9780471815181.

[73] L.P. Kadanoff, G. Baym, and D. Pines. *Quantum Statistical Mechanics*. Advanced Books Classics Series. Perseus Books, 1994. ISBN 9780201410464.

[74] M. V. Fischetti. Effect of the electron-plasmon interaction on the electron mobility in silicon. *Phys. Rev. B*, 44:5527–5534, Sep 1991. URL http://link.aps.org/doi/10.1103/PhysRevB.44.5527.

[75] Conyers Herring. Theory of the thermoelectric power of semiconductors. *Phys. Rev.*, 96:1163–1187, Dec 1954. URL http://link.aps.org/doi/10.1103/PhysRev.96.1163.

[76] Giorgia Fugallo, Michele Lazzeri, Lorenzo Paulatto, and Francesco Mauri. *Ab initio* variational approach for evaluating lattice thermal conductivity. *Phys. Rev. B*, 88: 045430, Jul 2013. URL http://link.aps.org/doi/10.1103/PhysRevB.88.045430.

[77] O. D. Restrepo, K. Varga, and S. T. Pantelides. First-principles calculations of electron mobilities in silicon: Phonon and coulomb scattering. *Applied Physics Letters*, 94(21): 212103, 2009. URL http://scitation.aip.org/content/aip/journal/apl/94/21/10.1063/1.3147189.

[78] Vincenzo Lordi, Paul Erhart, and Daniel Åberg. Charge carrier scattering by defects in semiconductors. *Phys. Rev. B*, 81:235204, Jun 2010. URL http://link.aps.org/doi/10.1103/PhysRevB.81.235204.

[79] D. Chattopadhyay and H. J. Queisser. Electron scattering by ionized impurities in semiconductors. *Rev. Mod. Phys.*, 53:745–768, Oct 1981. URL http://link.aps.org/doi/10.1103/RevModPhys.53.745.

[80] B. A. Sanborn, P. B. Allen, and G. D. Mahan. Theory of screening and electron mobility: Application to *n* -type silicon. *Phys. Rev. B*, 46:15123–15134, Dec 1992. URL http://link.aps.org/doi/10.1103/PhysRevB.46.15123.

[81] B.K. Ridley. *Quantum Processes in Semiconductors*. Oxford science publications. OUP Oxford, 1999. ISBN 9780198505792.

[82] T. C. McGill and R. Baron. Neutral impurity scattering in semiconductors. *Phys. Rev. B*, 11:5208–5210, Jun 1975. URL http://link.aps.org/doi/10.1103/PhysRevB.11.5208.

[83] J. R. Meyer and F. J. Bartoli. Phase-shift calculation of electron mobility in *n*-type silicon at low temperatures. *Phys. Rev. B*, 24:2089–2100, Aug 1981. URL http://link.aps.org/doi/10.1103/PhysRevB.24.2089.

[84] C. Hamaguchi. *Basic Semiconductor Physics*. Physics and astronomy online library. Springer, 2001. ISBN 9783540416395.

[85] K. M. Itoh, W. Walukiewicz, H. D. Fuchs, J. W. Beeman, E. E. Haller, J. W. Farmer, and V. I. Ozhogin. Neutral-impurity scattering in isotopically engineered ge. *Phys. Rev. B*, 50:16995–17000, Dec 1994. URL http://link.aps.org/doi/10.1103/PhysRevB.50.16995.

[86] J. Pernot, P. N. Volpe, F. Omnès, P. Muret, V. Mortet, K. Haenen, and T. Teraji. Hall hole mobility in boron-doped homoepitaxial diamond. *Phys. Rev. B*, 81:205203, May 2010. URL http://link.aps.org/doi/10.1103/PhysRevB.81.205203.

[87] T. H. Geballe and G. W. Hull. Seebeck effect in germanium. *Phys. Rev.*, 94:1134–1140, Jun 1954. URL http://link.aps.org/doi/10.1103/PhysRev.94.1134.

[88] T. H. Geballe and G. W. Hull. Seebeck effect in silicon. *Phys. Rev.*, 98:940–947, May 1955. URL http://link.aps.org/doi/10.1103/PhysRev.98.940.

[89] H J Goldsmid, C C Jenns, and D A Wright. The thermoelectric power of a semiconducting diamond. *Proceedings of the Physical Society*, 73(3):393, 1959. URL http://stacks.iop.org/0370-1328/73/i=3/a=306.

[90] Mattia Fiorentini and Nicola Bonini. Thermoelectric coefficients of *n*-doped silicon from first principles via the solution of the boltzmann transport equation. *Phys. Rev. B*, 94:085204.

[91] Jivtesh Garg, Nicola Bonini, and Nicola Marzari. First-principles determination of phonon lifetimes, mean free paths, and thermal conductivities in crystalline materials: Pure silicon and germanium. In SL Shinde and GP Srivastava, editors, *Length-scale Dependent Phonon Interactions*, volume 128 of *Topics in Applied Physics*, pages 115–136. Springer, 2014.

[92] C. Jacoboni. *Theory of Electron Transport in Semiconductors: A Pathway from Elementary Physics to Nonequilibrium Green Functions*. Springer Series in Solid-State Sciences. Springer Berlin Heidelberg, 2010. ISBN 9783642105869.

[93] Conyers Herring and Erich Vogt. Transport and deformation-potential theory for many-valley semiconductors with anisotropic scattering. *Phys. Rev.*, 101:944–961, Feb 1956. URL http://link.aps.org/doi/10.1103/PhysRev.101.944.

[94] Piotr Kowalczyk, Andrzej Palczewski, Giovanni Russo, and Zbigniew Walenta. Numerical solutions of the boltzmann equation: comparison of different algorithms. *European Journal of Mechanics - B/Fluids*, 27(1):62 – 74, 2008. URL http://www.sciencedirect.com/science/article/pii/S0997754607000428.

[95] Pierre-Alexandre Pantel, Dany Davesne, and Michael Urban. Numerical solution of the boltzmann equation for trapped fermi gases with in-medium effects. *Phys. Rev. A*, 91:013627, Jan 2015. URL http://link.aps.org/doi/10.1103/PhysRevA.91.013627.

[96] M Omini and A Sparavigna. An iterative approach to the phonon boltzmann equation in the theory of thermal conductivity. *Physica B: Condensed Matter*, 212(2):101 – 112, 1995. URL http://www.sciencedirect.com/science/article/pii/0921452695000163.

[97] Edgar Gabriel, Graham E. Fagg, George Bosilca, Thara Angskun, Jack J. Dongarra, Jeffrey M. Squyres, Vishal Sahay, Prabhanjan Kambadur, Brian Barrett, Andrew Lumsdaine, Ralph H. Castain, David J. Daniel, Richard L. Graham, and Timothy S. Woodall. Open MPI: Goals, concept, and design of a next generation MPI implementation. In *Proceedings, 11th European PVM/MPI Users' Group Meeting*, pages 97–104, Budapest, Hungary, September 2004.

[98] Jonathan R. Yates, Xinjie Wang, David Vanderbilt, and Ivo Souza. Spectral and fermi surface properties from wannier interpolation. *Phys. Rev. B*, 75:195121, May 2007. URL http://link.aps.org/doi/10.1103/PhysRevB.75.195121.

[99] M. C. Payne, M. P. Teter, D. C. Allan, T. A. Arias, and J. D. Joannopoulos. Iterative minimization techniques for *ab initio* total-energy calculations: molecular dynamics and conjugate gradients. *Rev. Mod. Phys.*, 64:1045–1097, Oct 1992. URL http://link.aps.org/doi/10.1103/RevModPhys.64.1045.

[100] Jonathan Richard Shewchuk. An introduction to the conjugate gradient method without the agonizing pain. 1994. URL http://www.cs.cmu.edu/~quake-papers/painless-conjugate-gradient.pdf.

[101] A. Greenbaum. *Iterative Methods for Solving Linear Systems*. Frontiers in Applied Mathematics. Society for Industrial and Applied Mathematics, 1997. ISBN 9780898713961.

[102] Nicholas A. Lanzillo, Jay B. Thomas, Bruce Watson, Morris Washington, and Saroj K. Nayak. Pressure-enabled phonon engineering in metals. *Proceedings of the National Academy of Sciences*, 111(24):8712–8716, 2014. URL http://www.pnas.org/content/111/24/8712.full.pdf.

[103] Bin Xu and Matthieu J. Verstraete. First principles explanation of the positive seebeck coefficient of lithium. *Phys. Rev. Lett.*, 112:196603, May 2014. URL http://link.aps.org/doi/10.1103/PhysRevLett.112.196603.

[104] Philip B. Allen and Božidar Mitrović. Theory of superconducting tc. volume 37 of *Solid State Physics*, pages 1 – 92. Academic Press, 1983. URL http://www.sciencedirect.com/science/article/pii/S0081194708606657.

[105] P. B. Allen. Electron-phonon effects in the infrared properties of metals. *Phys. Rev. B*, 3:305–320, Jan 1971. URL http://link.aps.org/doi/10.1103/PhysRevB.3.305.

[106] R. Bauer, A. Schmid, P. Pavone, and D. Strauch. Electron-phonon coupling in the metallic elements al, au, na, and nb: A first-principles study. *Phys. Rev. B*, 57:11276–11282, May 1998. URL http://link.aps.org/doi/10.1103/PhysRevB.57.11276.

[107] S. Y. Savrasov and D. Y. Savrasov. Electron-phonon interactions and related physical properties of metals from linear-response theory. *Phys. Rev. B*, 54:16487–16501, Dec 1996. URL http://link.aps.org/doi/10.1103/PhysRevB.54.16487.

[108] P. D. Desai, H. M. James, and C. Y. Ho. Electrical resistivity of aluminum and manganese. *Journal of Physical and Chemical Reference Data*, 13(4):1131–1172, 1984. URL http://scitation.aip.org/content/aip/journal/jpcrd/13/4/10.1063/1.555725.

[109] R. A. Matula. Electrical resistivity of copper, gold, palladium, and silver. *Journal of Physical and Chemical Reference Data*, 8(4):1147–1298, 1979. URL http://scitation.aip.org/content/aip/journal/jpcrd/8/4/10.1063/1.555614.

[110] P.G. Klemens, K.H. Hellwege, H. Landolt, R. Börnstein, and O. Madelung. *Metals: Electronic Transport Phenomena*, volume 15c of *New Series*. Springer, 1991. ISBN 9780387535128.

[111] Jerome G Hust, DH Weitzel, and RL Powell. Thermal conductivity, electrical resistivity, and thermopower of aerospace alloys from 4 to 300 k. *J Res Natl Bur Stand Sec A*, 75:269, 1971.

[112] George William Clarkson Kaye and Thomas Howell Laby. *Tables of physical and chemical constants and some mathematical functions*. Longmans, Green and Company, 1921.

[113] R. Franz and G. Wiedemann. Ueber die wärme-leitungsfähigkeit der metalle. *Annalen der Physik*, 165(8):497–531, 1853. URL http://dx.doi.org/10.1002/andp.18531650802.

[114] Dario Narducci, Stefano Frabboni, and Xanthippi Zianni. Silicon de novo: energy filtering and enhanced thermoelectric performances of nanocrystalline silicon and silicon alloys. *J. Mater. Chem. C*, 3:12176–12185, 2015. URL http://dx.doi.org/10.1039/C5TC01632K.

[115] Akram I. Boukai, Yuri Bunimovich, Jamil Tahir-Kheli, Jen-Kan Yu, William A. Goddard III, and James R. Heath. Silicon nanowires as efficient thermoelectric materials. *Nautre*, 451:168–171, 10 January 2008. URL http://dx.doi.org/10.1038/nature06458.

[116] Z. Aksamija and I. Knezevic. Thermoelectric properties of silicon nanostructures. In *Nanotechnology (IEEE-NANO), 2010 10th IEEE Conference on*, pages 806–810, Aug 2010.

[117] Zhao Wang, Shidong Wang, Sergey Obukhov, Nathalie Vast, Jelena Sjakste, Valery Tyuterev, and Natalio Mingo. Thermoelectric transport properties of silicon: Toward an *ab initio* approach. *Phys. Rev. B*, 83:205208, May 2011. URL http://link.aps.org/doi/10.1103/PhysRevB.83.205208.

[118] C. Jacoboni, C. Canali, G. Ottaviani, and A. Alberigi Quaranta. A review of some charge transport properties of silicon. *Solid-State Electronics*, 20(2):77 – 89, 1977. URL http://www.sciencedirect.com/science/article/pii/0038110177900545.

[119] C. Canali, C. Jacoboni, F. Nava, G. Ottaviani, and A. Alberigi-Quaranta. Electron drift velocity in silicon. *Phys. Rev. B*, 12:2265–2284, Sep 1975. URL http://link.aps.org/doi/10.1103/PhysRevB.12.2265.

[120] R. A. Logan and A. J. Peters. Impurity effects upon mobility in silicon. *Journal of Applied Physics*, 31(1):122–124, 1960. URL http://scitation.aip.org/content/aip/journal/jap/31/1/10.1063/1.1735385.

[121] P. Norton, T. Braggins, and Levinstein H. *Phys. Rev. B*, 8:5632, 1973.

[122] J. Y. Tang and Karl Hess. Impact ionization of electrons in silicon (steady state). *Journal of Applied Physics*, 54(9):5139–5144, 1983. URL http://scitation.aip.org/content/aip/journal/jap/54/9/10.1063/1.332737.

[123] Cheol-Hwan Park, Nicola Bonini, Thibault Sohier, Georgy Samsonidze, Boris Kozinsky, Matteo Calandra, Francesco Mauri, and Nicola Marzari. Electron-phonon interactions and the intrinsic electrical resistivity of graphene. *Nano Lett.*, 14(3):1113–1119, MAR 2014.

[124] G. Antonius, S. Poncé, P. Boulanger, M. Côté, and X. Gonze. Many-body effects on the zero-point renormalization of the band structure. *Phys. Rev. Lett.*, 112:215501, May 2014. URL http://link.aps.org/doi/10.1103/PhysRevLett.112.215501.

[125] G. D. Mahan, L. Lindsay, and D. A. Broido. The seebeck coefficient and phonon drag in silicon. *Journal of Applied Physics*, 116(24):245102, 2014. URL http://scitation.aip.org/content/aip/journal/jap/116/24/10.1063/1.4904925.

[126] E. Flage-Larsen and Ø. Prytz. The lorenz function: Its properties at optimum thermoelectric figure-of-merit. *Applied Physics Letters*, 99(20):202108, 2011. URL http://scitation.aip.org/content/aip/journal/apl/99/20/10.1063/1.3656017.

[127] Hyun-Sik Kim, Zachary M. Gibbs, Yinglu Tang, Heng Wang, and G. Jeffrey Snyder. Characterization of lorenz number with seebeck coefficient measurement. *APL Mater.*, 3(4):041506, 2015. URL http://scitation.aip.org/content/aip/journal/aplmater/3/4/10.1063/1.4908244.

[128] Yu. G. Gurevich and O. L. Mashkevich. *Sov. Phys. Solid State*, 30:1055, 1988.

[129] E. H. Sondheimer. The kelvin relations in thermo-electricity. *Proc. Roy. Soc., Lond. A*, 234(1198):391–398, 1956. URL http://www.jstor.org/stable/99844.

[130] R. S. Balmer, J. R. Brandon, S. L. Clewes, H. K. Dhillon, J. M. Dodson, I. Friel, P. N. Inglis, T. D. Madgwick, M. L. Markham, T. P. Mollart, N. Perkins, G. A. Scarsbrook, D. J. Twitchen, A. J. Whitehead, J. J. Wilman, and S. M. Woollard. Chemical vapour deposition synthetic diamond: materials, technology and applications. *JOURNAL OF PHYSICS-CONDENSED MATTER*, 21(36), SEP 9 2009. doi: {10.1088/0953-8984/21/36/364221}.

[131] Chris J. H. Wort and Richard S. Balmer. Diamond as an electronic material. *MATERIALS TODAY*, 11(1-2):22–28, JAN-FEB 2008. doi: {10.1016/S1369-7021(07)70349-8}.

[132] W. Gajewski, P. Achatz, O. A. Williams, K. Haenen, E. Bustarret, M. Stutzmann, and J. A. Garrido. Electronic and optical properties of boron-doped nanocrystalline diamond films. *Phys. Rev. B*, 79:045206, Jan 2009. URL http://link.aps.org/doi/10.1103/PhysRevB.79.045206.

[133] M. Werner, R. Locher, W. Kohly, D.S. Holmes, S. Klose, and H.J. Fecht. The diamond irvin curve. *Diamond and Related Materials*, 6(2):308 – 313, 1997. URL http://www.sciencedirect.com/science/article/pii/S0925963596006838.

[134] T. H. Borst and O. Weis. Boron-doped homoepitaxial diamond layers: Fabrication, characterization, and electronic applications. *physica status solidi (a)*, 154(1):423–444, 1996. URL http://dx.doi.org/10.1002/pssa.2211540130.

[135] John Y. W. Seto. The electrical properties of polycrystalline silicon films. *Journal of Applied Physics*, 46(12):5247–5254, 1975. URL http://scitation.aip.org/content/aip/journal/jap/46/12/10.1063/1.321593.

[136] J.-P. Lagrange, A. Deneuville, and E. Gheeraert. A large range of boron doping with low compensation ratio for homoepitaxial diamond films. *Carbon*, 37(5):807 – 810, 1999. URL http://www.sciencedirect.com/science/article/pii/S0008622398002759.

[137] Jan Isberg, Johan Hammersberg, Erik Johansson, Tobias Wikström, Daniel J. Twitchen, Andrew J. Whitehead, Steven E. Coe, and Geoffrey A. Scarsbrook. High carrier mobility in single-crystal plasma-deposited diamond. *Science*, 297(5587):1670–1672, 2002. URL http://science.sciencemag.org/content/297/5587/1670.

[138] Jan Isberg, Adam Lindblom, Antonella Tajani, and Daniel Twitchen. Temperature dependence of hole drift mobility in high-purity single-crystal cvd diamond. *physica status solidi (a)*, 202(11):2194–2198, 2005. URL http://dx.doi.org/10.1002/pssa.200561915.

[139] H. Pernegger, S. Roe, P. Weilhammer, V. Eremin, H. Frais-Kölbl, E. Griesmayer, H. Kagan, S. Schnetzer, R. Stone, W. Trischuk, D. Twitchen, and A. Whitehead. Charge-carrier properties in synthetic single-crystal diamond measured with the transient-current technique. *Journal of Applied Physics*, 97(7):073704, 2005. URL http://scitation.aip.org/content/aip/journal/jap/97/7/10.1063/1.1863417.

[140] Miloš Nesladek, Anna Bogdan, Wim Deferme, Nicolas Tranchant, and Philippe Bergonzo. Charge transport in high mobility single crystal diamond. *Diamond and Related Materials*, 17(7–10):1235 – 1240, 2008. URL http://www.sciencedirect.com/science/article/pii/S0925963508002367.

[141] Hendrik Jansen, Daniel Dobos, Thomas Eisel, Heinz Pernegger, Vladimir Eremin, and Norbert Wermes. Temperature dependence of charge carrier mobility in single-crystal chemical vapour deposition diamond. *Journal of Applied Physics*, 113(17):173706, 2013. URL http://scitation.aip.org/content/aip/journal/jap/113/17/10.1063/1.4802679.

[142] L. Reggiani, S. Bosi, C. Canali, F. Nava, and S. F. Kozlov. Hole-drift velocity in natural diamond. *Phys. Rev. B*, 23:3050–3057, Mar 1981. URL http://link.aps.org/doi/10.1103/PhysRevB.23.3050.

[143] N. Tranchant, M. Nesladek, D. Tromson, Z. Remes, A. Bogdan, and P. Bergonzo. Time of flight study of high performance cvd diamond detector devices. *physica status solidi (a)*, 204(9):3023–3029, 2007. URL http://dx.doi.org/10.1002/pssa.200776342.

[144] K. Somogyi. Interpretation of electrical and galvanomagnetic properties of diamond monocrystals. *Applied Physics Letters*, 75(13):1911–1913, 1999. URL http://scitation.aip.org/content/aip/journal/apl/75/13/10.1063/1.124868.

[145] J. Barjon, N. Habka, C. Mer, F. Jomard, J. Chevallier, and P. Bergonzo. Resistivity of boron doped diamond. *physica status solidi (RRL) – Rapid Research Letters*, 3(6):202–204, 2009. URL http://dx.doi.org/10.1002/pssr.200903097.

[146] Jan Isberg. *Transport Properties of Electrons and Holes in Diamond*, pages 29–48. John Wiley & Sons, Ltd, 2009. ISBN 9780470740392. URL http://dx.doi.org/10.1002/9780470740392.ch2.

[147] G. L. Pearson and J. Bardeen. Electrical properties of pure silicon and silicon alloys containing boron and phosphorus. *Phys. Rev.*, 75:865–883, Mar 1949. URL http://link.aps.org/doi/10.1103/PhysRev.75.865.

[148] S. Yamanaka, D. Takeuchi, H. Watanabe, H. Okushi, and K. Kajimura. Low-compensated boron-doped homoepitaxial diamond films using trimethylboron. *physica status solidi (a)*, 174(1):59–64, 1999. URL http://dx.doi.org/10.1002/(SICI)1521-396X(199907)174:1<59::AID-PSSA59>3.0.CO;2-A.

[149] Atsushi Koizumi, Jun Suda, and Tsunenobu Kimoto. Temperature and doping dependencies of electrical properties in al-doped 4h-sic epitaxial layers. *Journal of Applied Physics*, 106(1), 2009. URL http://scitation.aip.org/content/aip/journal/jap/106/1/10.1063/1.3158565.

[150] Lino Reggiani, David Waechter, and Stefan Zukotynski. Hall-coefficient factor and inverse valence-band parameters of holes in natural diamond. *Phys. Rev. B*, 28: 3550–3555, Sep 1983. URL http://link.aps.org/doi/10.1103/PhysRevB.28.3550.

[151] R.D. Barnard. *Thermoelectricity in Metals and Alloys*. Taylor & Francis, 1972. ISBN 9780850660593.

[152] Jeremiah R. Lowney and Herbert S. Bennett. Majority and minority electron and hole mobilities in heavily doped gaas. *Journal of Applied Physics*, 69(10):7102–7110, 1991. URL http://scitation.aip.org/content/aip/journal/jap/69/10/10.1063/1.347650.